GPS Kinematic Positioning for the Airborne Laser Altimetry at Long Valley, California

by

Gang Chen

B.S., Astronomy (1986)
Nanjing University

M.S., Astronomy (1989)
Shanghai Observatory, Chinese Academy of Science

Submitted to the Department of Earth, Atmospheric, and planetary Sciences in partial fulfillment of the requirements for the degree of

Doctor of Philosophy in Geophysics

at the

MASSACHUSETTS INSTITUTE OF TECHNOLOGY

Nov. 1998

Author .....
Department of Earth, Atmospheric, and Planetary Sciences
June 19, 1998

Certified by .....
Thomas A. Herring
Thesis Supervisor

Accepted by .....
Ronald G. Prinn
Department Head

GPS Kinematic Positioning for the Airborne Laser Altimetry at Long Valley, California

by

Gang Chen

Submitted to the Department of Earth, Atmospheric, and Planetary Sciences on June 19, 1998 in partial fulfillment of the requirements for the degree of Doctor of Philosophy in Geophysics

Abstract

The object of this thesis is to develop a reliable algorithm and software for cm-level kinematic GPS (Global Positioning System) data analysis. To assess the accuracy of the software, we use it to determine the trajectory of the aircraft during the surveys at Long Valley, California, in 1993 and 1995. This thesis covers the algorithm development, the modeling, and the software design. We implement a robust Kalman filter to perform the kinematic data processing for GPS measurements. In the kinematic data processing with the Kalman filter, the estimates of the aircraft's position, the GPS receiver clock, and atmospheric corrections are modeled with appropriate stochastic processes.

To achieve cm-level accuracy for an aircraft trajectory, the GPS phase observables must be used and the integer-cycles of phase ambiguity must be resolved. In this thesis, we investigate the ambiguity problem in different situations and develop different ambiguity strategies depending on the situation. Firstly, we develop a position-independent (position-free) ambiguity search method for the initial ambiguity search for GPS kinematic surveying. Our ambiguity search method focuses on providing the flexibility and uniqueness to determine the correct ambiguities in most experimental conditions including long baselines (up to 100 km), high noise level in low elevation observations, and "bad" observations during the search. Secondly, we develop a method to utilize position-free widelane and extrawidelane observables to detect cycle slips that occur when the signal from a GPS satellite is interrupted during the flight, for example, when the satellite is blocked by the aircraft's wing during a turn. Our ambiguity algorithms use dual frequency GPS observables so that the effects of the ionospheric delay can be accounted for. Several tests performed indicate that our ambiguity strategy works well for a separation between the moving and fixed GPS receivers of up to 100 km.

We developed a kinematic software developed to automatically detect various errors during the data processing, including detecting and correcting of cycle slips, detecting and removal of bad data, and performing ambiguity searches. The user interface to the software is command driven with default values for most processing. This interface provides flexibility and should make the software usable with little training.

To evaluate our software, we processed GPS data taken in the 1993 and 1995 Long Valley airborne laser altimetry surveys. We performed four types of tests: (a) Static tests which

the evaluate the root-mean-square (RMS) scatter of the aircraft position while it is stationary on the runway; (b) runway tests which compare the height estimates of the aircraft at approximately the same position along the runway during taxiing, takeoffs and landings; (c) lake tests in which we compare profiles of Lake Crowley's surface and crossings on the lake surface; and (d) Benton crossing tests in which we compare surface height estimates at location within 2 m of each other at a grassy region of Benton Crossing. The latter two tests use of combination of the laser altimeter and GPS trajectory data. The processing of the laser data with our GPS trajectory was performed by our colleagues at the Scripps Institute of Oceanography.

The static tests show that during the times the aircraft was stationary at the beginning and ends of flights, the RMS scatter of relative height difference between the aircraft and the reference GPS station at Bishop airport, approximately 500 meters from the aircraft, varied between 4 and 2 mm for both campaigns. The runway tests show that the average height differences between trajectories repeat to within 4 cm for six tracks on the taxiway, during the takeoffs and landings. The lake surface tests show height variations within 3 cm for the lake surface after removing the cubic polynomial to approximately fit for the geoid-ellipsoidal height differences and flow within the lake for each of the five flight sections over the lake. The Lake Crowley crossover analysis shows a mean difference of 0.2 cm and RMS scatter of 4.5 cm for relative height from laser footprint pairs within 2 m distance. The Benton Crossing crossover results show a mean value of 0.2 cm and RMS scatters of 15.5 cm in a similar cross analysis after outliers are deleted. Based on our analyses, we conclude that laser altimetry over the flat surface (i.e. Lake Crowley) can determine surface heights with ~3 cm precision. The contribution from the error in GPS trajectory appears to be 1-2 cm.

Thesis supervisor:	Thomas A. Herring
Title:	Professor of Geophysics
Committee:	Professor Thomas A. Herring Dr. Robert W. King Professor Chris J. Marone Professor Jean-Bernard Minster

Acknowledgments

The completion of this thesis would not have been possible without the support of many people.

First, I would like to thank my advisor, Tom Herring, not only for his guiding the preparation in this thesis, but also for his continuing support, and encouragement through five years at MIT. He was always willing to share his insights with me and was patient with every questions. From Tom, I learned a lot, from how GPS works for geodesy to how to make the plots more colorful. Also I am grateful for the freedom he gave me to explore and develop my own ideas.

I owe a special thank to Adrian Borsa. Without his help in the ATLAS data analysis, I could not have finished Chapter 5 of this thesis. He has spent a great deal of his time going through the data analysis with my numerous tests. I would also like to thank Michelle Hofton for her time spent with me discussing the GPS processing at NASA Goddard Space Flight Center (GSFC) and providing data, information and suggestions whenever I wanted. I am indebted to Prof. Bernard Minster and his group for allowing me use the data and for inviting me to the field test in Long Valley. I have enjoyed working with them.

I would like to thank Bob King for his critical comments and discussions on the thesis which not only made my ill-written sentences more readable, but also led me to a better understanding of the GPS system.

My thanks also go to Arthur Niell for providing mapping function code, to Paul Tregoning for his comments and tests on the use of the first version of my GPS kinematic software, to Ming Fang, Brad Hager, Clint Conrad, Katy Quinn, Simon McClusky and other 6th floor colleagues for sharing their geophysical knowledge, computer tricks and fun; To Chris Marone, I am grateful for the chance to take his interesting course and to do friction research with his instruction; To Ben Chao for the invitation to visit NASA GSFC, and for discussions covering a broad scope of problems in the Earth sciences.

I would like to express my gratitude to my parents. For the post five years, their endless

support and understanding from the remote other side of Earth has meant a lot to their son. Also thanks to my sister for her encouraging me cross the Pacific and helping me take care of our parents.

Finally, the person I wish to thank most is, my wife, Wei Zhu, who made my journey to MIT not lonely, and fills my heart with confidence, courage, and love all the time.

This work was supported by NASA grants NAGS-3550 and NASS-33017.

Table of Contents

Chapter 1 Introduction

The object of this thesis is to develop a reliable algorithm and software for cm-level kinematic GPS data analysis and to assess its accuracy in determining the trajectories for airborne laser altimetric surveys at Long Valley, California. The availability of precise laser altimeter data provides us with a unique opportunity to evaluate the accuracy of the aircraft kinematic trajectory during flight.

1.1 Kinematic GPS Surveying

Global Positioning System (GPS) has been widely used in navigation, timing and surveying for over 20 years. In geodetic and geophysical fields, GPS also provides a tool for high precision measurements of plate motions, tectonic deformation and volcanic monitoring. Recent results show few mm-level accuracy for position determinations in some GPS networks [*Alber et. al*, 1997].

In kinematic differential GPS surveying one GPS antenna is normally moving with a vehicle or an aircraft while the other remains stationary at a ground reference station. Both antennas record the GPS signals continuously so than the relative positions of the antennas can be determined by differential data processing. The mobility and rapidity of kinematic GPS surveying provides numerous opportunities for precise quantitative studies such as rapid surveying cross faults shortly after earthquakes [*Hirahara et al.*, 1996; *Genrich et al.*, 1997], position controlling for airborne photogrammetry [*Ackermann*, 1992; *Becker and Barriere*, 1993], and seismic explosive source positioning on the ocean [*Chapman et al.*, 1997; *Tregoning et al.*, 1998]. Besides its direct applications, precise kinematic GPS can be also used to improve the accuracy of other techniques. Without the cm-level accuracy of kinematic GPS positioning for aircraft, for example, it is impossible for the airborne laser altimeter technique to monitor cm-level variations of ground displacement.

The common observables of GPS are pseudorange (time difference between transmission and reception of signal with the transmission time set by the satellite clock and reception time measured with a non-synchronized ground clock) and carrier beat phase (difference between the received phase and the phase generated from local oscillator of receiver). Doppler measurements are also available but not used here. For cm-level measurements, carrier phase is generally used because it is much more precise than pseudorange. Carrier phase is most useful, however, when there are long tracks of uninterrupted tracking of a satellite so that the change in range to the satellite may be used for positioning. Also, dual frequency measurements are needed to remove the frequency-dependent (dispersive) ionospheric effects on GPS signals.

Several data analysis methods have been developed which depend on the use of different observables. Utilizing the code signals directly received from satellites, point positioning is widely used in general surveys but needs knowledge of satellite clock errors as well as orbital position information. By comparing the signals from the same satellite at two GPS receivers, differential positioning (single difference) removes effects of the unknown satellite clock. The comparison of single-difference observables from two satellites (double differencing) can remove the receiver's clock variation. For close stations, many other errors such as orbital errors, ionospheric delays, tropospheric delays, and earth tide effects, also cancel to a large degree in differential method. pseudorange differential positioning is used but limited by measurement accuracy. Carrier phase differential method with static receivers can use changes in phase to make more accurate positioning, but the most accurate results are obtained if the ambiguities in the double differences can be resolved.

As a surveying technique, kinematic GPS has wide applications but also stringent requirements. Compared to static GPS surveys, the occupation time is shorter and the amount of data accumulated is less in the kinematic applications. Also the rapid changes of environment around the moving GPS antenna tend to create more technical problems than occur in a static survey at a fixed site. The impact of these problems can be severe in aircraft applications where the motions are rapid and the aircraft can fly a large distance from the base station. For kinematic positioning, resolving cycle ambiguities is critical. The fast movement of aircraft can make tracking more difficult for receivers, leading to corrupt data than for the static case.

The use of kinematic GPS technique requires a reliable and fast algorithm for the GPS data analysis. One of the primary motivations for this study is to develop GPS analysis software to help scientists, especially for those involved in the Long Valley airborne laser altimetric experiments, to whom GPS is merely a secondary tool, to process smoothly kinematic GPS data. For easy but reliable use, software for aircraft positioning must have the following features: a) the software must resolve the ambiguities properly from the beginning of the survey while the aircraft is stationary; b) for a long-distance and long-time flight, new satellites should be used and their ambiguities must be resolved immediately; c) Corrupted data and loss-of-lock on satellite signal must be detected and then either deleted or its cycle slip re-estimated; d) for large separations, ionospheric delay must be accounted for. Ideally all of these are done autonomously by software. In this thesis, we discuss our development of a kinematic GPS analysis program. We also evaluate the program using data from Long valley laser altimeter campaigns.

1.2 Geodetic Measurements at Long Valley

Long Valley caldera is a large volcano located 20 km south of Mono Lake along the eastern side of the Sierra Nevada in east-central California (Figure 1.1). In this area of eastern California, persistent earthquakes and volcanic eruptions have been occurring for over 3 million years [*Knesel and Davidson*, 1997]. These activities formed the current eastern Sierra landscape in the vicinity of Long Valley caldera. The caldera is an elliptically shaped area approximately 25 by 60 kilometers in size (the elliptical area in Figure 1.1). Ten kilometers below the surface of the caldera is a magma chamber [*Dvorak and Dzurisin*, 1997].

After 50 years of relative quiescence, the volcanic activities resumed during the 1980s and 1990s. The new activities started in 1980 with frequent earthquakes in the Long Valley caldera region [*Julian*, 1983; *Julian and Sipkin*, 1985]. The vertical surface uplift near the center of the resurgent dome was detected at a rate of 4 to 5 cm per year [*Savage et al.*, 1986]. Models consistently showed that the bulk of the uplift was caused by an expanding magma reservoir 6 to 10 km beneath the center of the resurgent dome, with an injection volume of about 0.15 km^3

between 1975 and 1983 [*Rundle and Whitecomb*, 1984]. In 1989 a massive earthquake swarm occurred beneath Mammoth Mountain. Uplift increased to almost 5 cm/year which can be modeled by a re-inflation of the magma body approximately 0.025 km^3 for the 1989-1991 period [*Langbein et al.*, 1993]. These activities brought about a total uplift near 70 cm in the last two decades. This magma body may have a total volume of 500-1,000 km^3. Intensive research has been pursued to map the distribution of magma beneath the whole area as well as its inflation rate.

The increased activities have motivated increased monitoring in this region. Several groups, including the U.S. Geological Survey, began monitoring the area intensively for earthquake activity and ground deformation, in addition to conducting many detailed regional geological and geophysical surveys in the Long Valley area. About 50 permanent seismic stations of the Northern California Seismic Network (NCSN) are operated within 50 km of the caldera to monitor the seismic activities. Seismometers are deployed in the Mammoth Mountain and the southern rim of the caldera to record the seismic activities over the dome and nearby area.

Surface height change, the uplift, in the caldera is an important indicator of volcanic eruptions. The surface rises or falls as magma moves under the surface. The uplift plays a key role in revealing the movement of geothermal and/or volcanic fluids under Long Valley dome. Researchers are trying to model the rate and pattern of surface displacement. Those models generally consist of several pressure sources embedded in an elastic material. The vertical and horizontal displacement pattern reveals such characteristics as depth and rate of magma accumulation under the ground and are needed to build up models. Besides the rapid change before and during volcanic eruptions, long term changes occur near the volcanic area. The shallow magma causes the ground surface to rise or fall slowly, and those irregular changes may be a good sensor for eruption prediction. Along with seismic activity, the slight displacements of the surfaces are the most significant phenomena that can be monitored before and between volcano eruptions.

Geodetic measurements have proven to be useful for providing information as precursors to volcanic eruptions. Surface uplift in the caldera has been measured with Electromagnetic Distance Measurements (EDM) since 1975 [*Denlinger and Riley*, 1984], and with accurate two-color geodimeter measurements since 1983 [*Langbein et al.*, 1995]. Ground GPS measurements have been also used to document changes in the reservoir and strain field over the last several years [*Dixon et al.*, 1993 & 1997; *Marshall et al.*, 1996; *Webb et al.*, 1995]. Ground GPS networks and leveling survey usually measure the relative positions at bench marks scattered across the surface. Repeat measurements of the benchmarks are used to determine the changes in relative positions. Such ground networks produce very precise results but do not provide good coverage around the volcanic areas. For a typical 10-plus kilometer square volcanic area, a large number of points is needed to determine the details of surface displacement associated with the underground magma movements. The expense of maintaining such networks could be prohibitive for long term monitoring. Furthermore, the largest displacement often occurs near the center of volcanic areas where an eruption would endanger both personal and equipment.

In addition to the scattered ground-based measurements, aircraft or satellite observations could provide a valuable data source in obtaining a dense coverage over the uplift area directly without extensive increase of the expense and labor cost. While ground surveying can provide precise measurements of changes in fixed benchmarks, airborne surveying can provide less precise but much denser measurements of profiles directly over the center of uplift areas in a short time. In the future, an aircraft laser system can provide the capability for a rapid topographic profiler, if needed, in response to any area with increased geologic activity, particularly in remote or dangerous volcanic environments.

In order to test this new technology, from 1993 to 1997 researchers from several universities and government agencies led by the Scripps Institution of Oceanography (SIO), NASA's Goddard Space Flight Center (GSFC) and Wallops Flight Facility (WFF), conducted aircraft topographic surveying over the Long Valley caldera, California. Such surveys are performed using an airborne laser system developed by WFF. The objective of this field project was not only to measure the uplift over the resurgent dome and nearby areas of Long Valley caldera, but also to improve and refine the equipment and analysis techniques for the future

application of airborne and spaceborne laser altimetry.

Besides the field tests conducted by SIO, GSFC and WFF, the Long Valley survey work also involved collaborations among many research groups at the Massachusetts Institute of Technology (MIT), Jet Propulsion Laboratory (JPL), Lawrence Livermore National Laboratory, U.S. Geological Survey and the University of Arizona to provide technical help. The role of the MIT team focused on the assessment of GPS data analysis for GPS aircraft tracking and the development of a robust and easy-to-use software package for the precise kinematic GPS surveying.

1.3 Laser Altimetry

The principle of laser profiling (ranging) is shown in Figure 1.2. A short pulse (usually infrared radiation) is emitted towards the surface by the instrument in the aircraft, and its echo is detected some time later. By measuring the time delay between the transmission and reception of a signal and knowing the speed of propagation of the light pulse, the range (distance) from the instrument to the surface can be determined. By sending out a continuous stream of pulses, the system can build up a profile of the range. If the position of the aircraft, the direction of the laser pointing, and the relative position of the laser measurement point and GPS receiver in the aircraft are accurately known as a function of time, the surface profile may then be deduced. The surface heights calculated are referenced to ellipsoid (a purely geometric shape), not to the geoid (irregular shape related to local gravity). Geoid models can be used to compute the difference between the geoid and ellipsoid surface, i.e. the geoidal heights N in Figure 1.2. for changes in surface height, However, the difference between the ellipsoid and geoid is not important unless the geoid height is changing.

Laser altimeters have been successfully used on NASA space shuttle missions [*Zuber et al.*, 1992; *Smith and Sandwell*, 1994, and *Smith et al.*, 1997]. Several laser instruments are under development for Earth topography including the Geoscience Laser Altimetry System (GLAS) and the Vegetation Canopy Lidar (VCL). The GLAS satellite will be placed in orbit around the Earth in mid-2001. In recent years, in support of the spaceborne missions, airborne laser

altimeters have been under study for their utility in profiling topographic features of the Earth. Satellite laser altimeters have been used to profile the surface of the moon and Mars. Laser altimetry utilizes a much more focused beam than equivalent radar instruments, resulting in a smaller footprint, and is more sensitive to the angular attitude of the platform. The airborne laser altimeter technology has been used to characterize the geomorphology of the volcanic island of Surtsey, in the North Atlantic [*Garvin,* 1996], and has shown promise in providing height of land surface for satellites in measurements of the Greenland ice sheet height [*Krabill et al.*, 1995]

1.4 Role of GPS in Airborne Altimetry

One of the main obstacles to the application of airborne laser altimetry is the effect of the trajectory measurement error. The laser instrument on the aircraft measures the surface height relative to the aircraft position directly by emitting and receiving the laser signals reflected from the ground. In order to obtain the surface profile variations, laser measurements have to be tied to a well-defined solid Earth coordinate frame, for example, via differential GPS tracking of the aircraft from ground stations. In traditional navigation systems, including the inertial navigation system, the accuracy of position determination for aircraft is somewhere between 30 cm and 2 meter, worse than the altimeter precision by a factor of ten to fifty. Without cm-level precise aircraft tracking, it is impossible for the aircraft laser technique to approach the accuracy necessary to measure ground motions as small as 4 cm per year, the expected magnitude caused by volcanic activity at Long Valley.

The current instrument precision of GPS is capable of allowing GPS to track a moving object with the required cm-level accuracy. To reach the potential of centimeter-level kinematic GPS surveying, however, several technical problems in the GPS data analysis have to be dealt with carefully. To achieve the accuracy requires the integer cycle ambiguities in the carrier phase measurements to be resolved correctly. In the mountainous areas near Long Valley, the differencing of observations in two GPS antennas may not remove all of the ionospheric effects, multipath effects (reflection from ground or objects) and other non-common model errors. These errors can corrupt the ambiguity resolution of the phase observations. The algorithm developed

should provide unique ambiguity resolution in general conditions. In addition, the most complete model of GPS observations should include all effects larger than one centimeter for ground distance greater than 100 km. These models include precise satellite ephemerides and height dependent atmospheric delay models. The long experiment duration (>4 hrs) and long baselines require that cycle slips during flight, acquiring of new satellites and removal of corrupted data, all be handled by the algorithm with minimum user interaction.

Reliable and fast software is required for the kinematic differential GPS data analysis to achieve its potential to the cm-level in accuracy. Many commercial software packages are capably of the cm-level accuracy for the differential GPS kinematic surveys in small areas (baseline shorter than 10 km), but they often do not work reliably in a large area (100 km horizontal separation and 10 km altitude difference). Analyses of the altimeter flights in Long Valley, had used the commercial Ashtech GPS software PNAV and NASA GITAR software [*Martin*, 1991] to obtain the GPS trajectories [*Ridgway et al.*, 1997; *Hofton et al.*, 1997]. We tested three software packages, PNAV, GITAR and our kinematic GPS software TRACK (TRA jectory Calulation with Kalman filter) for the September 28, 1993 survey in Long Valley. comparing the estimated heights of the aircraft before takeoff and after landing at the airport. TRACK and GITAR generated similar height estimates (within 1 cm) after we carefully corrected all the ambiguities of phase observations for GITAR. The after-landing height estimate of the aircraft from the PNAV has a 5 cm difference from other two programs although they are set with the same height before the takeoff. GITAR is capable to provide cm-level GPS trajectory determination if there are no cycle slips, signal lock loss in the GPS phase observations, and all ambiguities are reliably solved during static portion of flights. Cycle slips and changes in satellite visibility need to be handled interactively in GITAR, however, which makes autonomous data processing difficult. Also GITAR has a requirement of using a common satellite for ambiguity adjustment and double differencing and this limits its use in long-time flights. For these reasons, we felt that it was important to develop a new algorithm that would handle complex situations during flight and would process GPS data largely autonomously.

This thesis documents our approach to the development of algorithms, computer codes, and analysis methods for aircraft GPS navigation for the Long Valley mission. In Chapter 2, we

describe our Kalman filter algorithm as well as the mathematical models and stochastic properties of state variables used in the algorithm. Also we describe the software structure for this algorithm. Chapter 3 addresses our method for the integer ambiguity resolution of carrier phase measurements. We also discuss the application of this method and its validation for short and long baselines. In Chapter 4 we demonstrate the application of our kinematic GPS algorithm in the data analysis in Long Valley Mission. In Chapter 5, we use laser altimeter results to verify the accuracy of GPS trajectory based on our method.

References

Ackermann, F., Kinematic GPS control for photogrammetry, *Photogrammetric Record*, **14**, 261-276, 1992

Alber, C., R. Ware, C. Rocken and F. Solheim, GPS surveying with 1-mm precision using corrections for atmospheric slant path delay, *Geophys. Res. Lett.*, **24**, 1859-1865, 1997.

Becker, R.D. and Barriere, J.P., Airborne GPS for photo navigation and photogrammetry: an integrated approach, *Photogrammetric Engineering and Remote Sensing*, **59**, 1659-1665, 1993

Chapman, N.R.; Jaschke, L.; McDonald, M.A.; Schmidt, H.; Johnson, M., Matched field geoacoustic tomography experiments using light bulb sound sources in the Haro Strait sea trial, *Oceans '97, MTS/IEEE Conference Proceedings*, **1510**, 763-768, 1997.

Denlinger, R. and F. Riley, Deformation of Long Valley Caldera, Mono County, California, from 1975 to 1982, *J. Geophys. Res.*, ***89,*** 8303-8314, 1984.

Dixon, T.H., M. Bursik, S. Kornreich Wolf, M. Heflin, F. Webb, F. Farina, and S. Robaudo, Constraints on deformation of the resurgent dome, Long Valley Caldera, California, from space geodesy. *In Contributions of Space Geodesy to Geodynamics: Crustal Dynamics, Geodynamics Series 23,* 193-214, American Geophysical Union, Washington, 1993.

Dixon, T.H., A. Mao, M. Bursik, M. Heflin, J. Lanbein, R. Stein, and F. Webb, Continuous monitoring of surface deformation at Long Valley caldera, California with GPS. *J. Geophys. Res.*, ***102,*** 12,017-12,034, 1997.

Dvorak, J.J. and Dzurisin, D., Volcano geodesy: the search for magma reservoirs and the formation of eruptive vents. *Reviews of Geophysics, 35,* 343-384,1997

Garvin, J.B., Topographic characterization and monitoring of volcanoes via aircraft laser altimetry, *Geological Society of London Special Publication, **110,*** 137-153, 1996.

Genrich, J.F.; Bock, Y.; Mason, R.G., Crustal deformation across the Imperial Fault: results from kinematic GPS surveys and trilateration of a densely spaced, small-aperture network, *J. Geophys. Res.*, **102**, 4985-5004, 1997.

Hirahara, K; Nakano, T; Kasahara, M; Takahashi, H; Ichikawa, R; Miura, S; Kato, T; Nakao, S;

Hirata, Y; Kotake, Y; Chachin, T; Kimata, F; Yamaoka, K; Okuda, T; Kumagai, H; Nakamura, K; Fujimori, K; Yamamoto, T; Terashima, T; Catane; Tadokoro, K; Kubo, A; Otsuka, S; Tokuyama, A; Tabei, T; Iwabuchi, T; Matsushima, T, GPS Observations of Post-Seismic Crustal Movements in the Focal Region of the 1995 Hyogo-ken Nanbu Earthquake -- Static and Real-Time Kinematic GPS Observations, *Journal of Physics of the Earth*, **44, No. 4**, 301-334, 1996

Hofton, M., J. Blair, B. Minster, J. Ridgway, D. Rabine, J. Bufton, and N. Williams, Using laser altimetry to detect topographic change at long Valley caldera, California, *Earth Surface Remote Sensing, **SPIE 3222,*** 295-306, 1997.

Julian, B.R., Evidence for dyke intrusion Earthquake mechanisms near Long Valley Caldera, California, *Nature,**303,*** 323-325, 1983.

Julian, B. R. and S. A. Sipkin, Earthquake processes in the Long Valley caldera area, California, *J. Geophys. Res., 90,* 11,155-11,169, 1985.

Knesel, K. M., Davidson, J. B., The Origin and Evolution of Large-Volume Silicic Magma Systems: Long Valley Caldera. *International Geology Review. 39, **11,*** 1033-1047, 1997.

Krabill, W. B., Thomas, R. H., Martin, C. F., Swift R. N. and Frederick, E. B., Accuracy of airborne laser altimetry over the Greenland ice sheet, *Int. J. Remote Sensing, **16,*** 1211-1222, 1995.

Langbein, J.O., D.P. Hill, T.N. Parker, and S.K. Wilkinson, An episode of re-inflation of the Long Valley caldera, eastern California: 1989-1991. *J. Geophys. Res., **98,*** 15,851-15870, 1993.

Langbein, J. O., D. Dzurisin, G. Marshall, R. Stein, and J. Rundle, Shallow and peripheral volcanic sources of inflation revealed by modeling two-color geodimeter and leveling data from Long Valley caldera, California, 1988-1992. *J. Geophys. Res., **100,*** 12,487-12,495, 1995.

Marshall, G. A; Langbein, J.; Stein, R. S; Lisowski, M. Svarc, J., Inflation of Long Valley caldera, California, Basin and Range strain, and possible Mono Craters' dike opening from 1990 to 1994 GPS surveys, *Geophys. Res. Lett., **24,*** 1003-1047, 1996.

Martin C., GITAR program documentation, *NASA contract number NAS5-31558, Goddard Space Flight Center, Wallops Flight Facility, Wallops Island, VA*, 1991.

Ridgway, J.R., J.B. Minster, N.P. Williams, J.L. Bufton, and W. Krabill, Airborne laser altimetry

survey of Long Valley, California, *Geophys. J. Int.* ***131***, 267-280, 1997.

Rundle, J. B. and J. H. Whitcomb, A model for deformation in Long Valley, California, 1980-1983, *J.Geophys. Res.*, ***89***, 9371-9380, 1984.

Savage, J. C., Cockerham, R. S. and Estrem, J. E., Deformation near the Long Valley Caldera, Eastern California, 1982-1986, *J. Geophys. Res.*, ***92***, 2721-2746, 1986.

Smith, W.H.F. & Sandwell, D.T., Bathymetric prediction from dense satellite altimetry and sparse shipboard bathymetry, *J. Geophys. Res.*, ***99***, 21803-21824, 1994.

Smith, D. E., M. Zuber, G. Neumann, and F.G. Lemoine, Topography of the Moon from the Commenting Lidar, *J. Geophys. Res.*, ***102***, 1591-1611, 1997.

Tregoning, P.; Lambeck, K.; Stolz, A.; Morgan, P.; McClusky, S.C.; van der Beek, P.; McQueen, H.; Jackson, R.J.; Little, R.P.; Laing, A.; Murphy, B., Estimation of Current Plate Motions in Papua New Guinea from Global Positioning System Observations, *J. Geophys. Res.*, **103**, 12181- 12203, 1998

Webb, F.H., Bursik, M.I. Dixon, T., Farina, F., Marshall, G. & Stein, R.S., Inflation of Long Valley Caldera from one year of continuous GPS observations, *Geophys. Res. Let.*, ***22***, 195-198, 1995.

Webb, F.H., Hensley, S., Rosen, P. and Langbein, J.O., Understanding volcanic inflation of Long Valley Caldera, California, from differential synthetic aperture radar observations, *Eos Trans. AGU Supp., 75,* ***166***, 1994.

Zuber M., D. Smith, S. Solomon, D. Muhleman, J. Head, J. Garvin, J. Abshire, and J. Bufton, The Mars Observer Laser Altimeter investigation, *J. Geophys. Res.*, ***97***, 7781-7797, 1992.

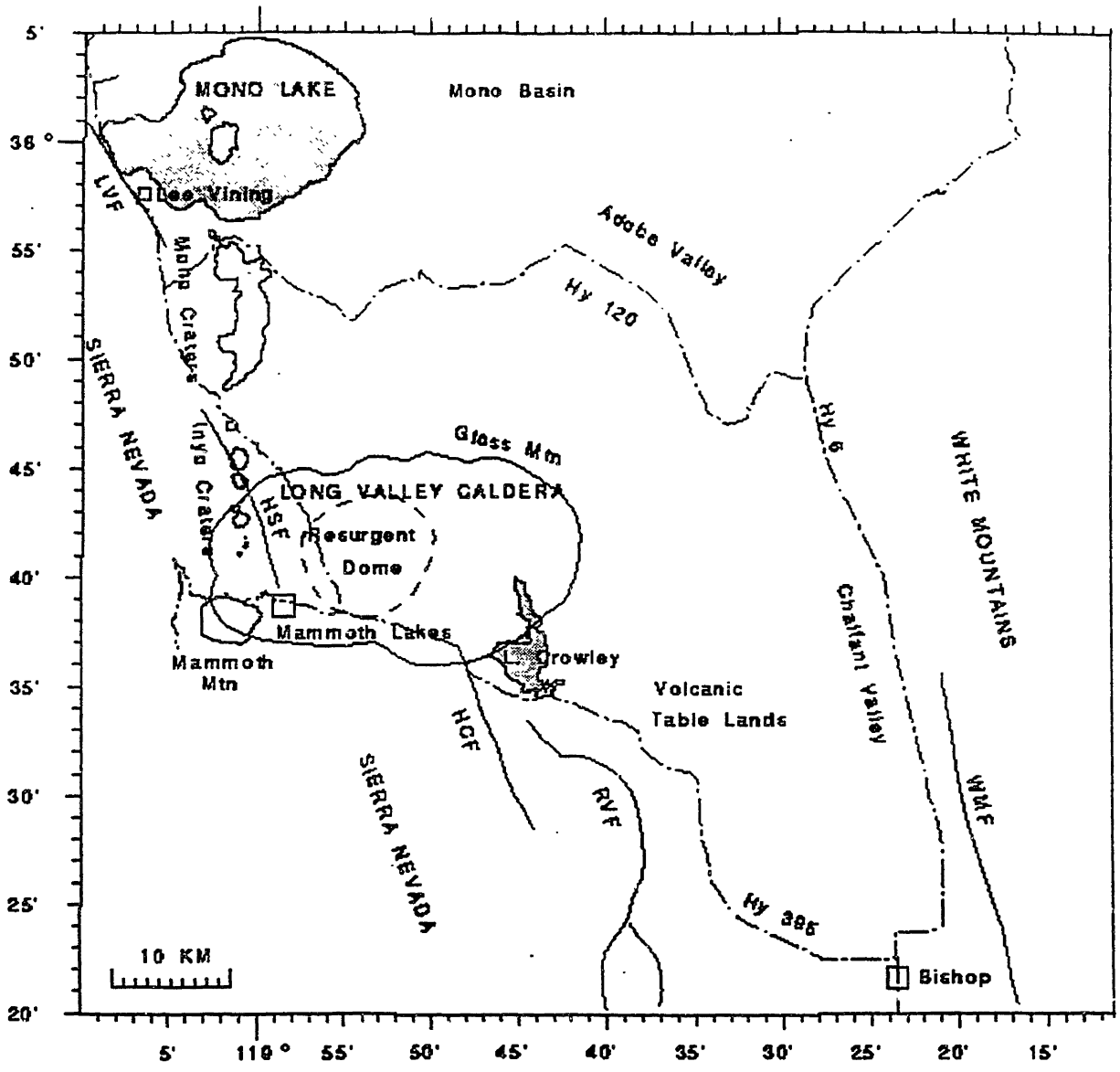

Figure 1.1 The location of Long Valley caldera

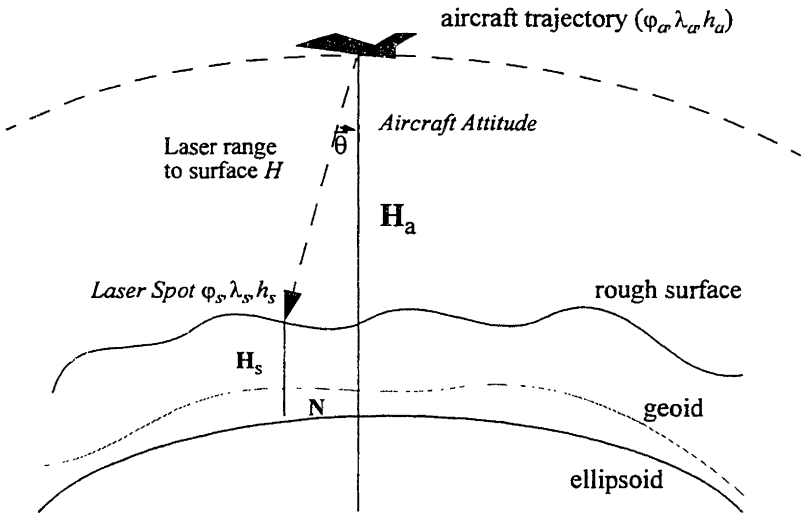

Figure 1.2 Scheme of airborne laser measurement. The bold characters represent the vectors. The aircraft obtains the distance H between the laser spot of the hitted ground to the aircraft via its laser pulse ranging. Then the vector $\mathbf{H}$, the relative position of laser spot to the aircraft is determined by its range value H and the orientation $\bar{\theta}$ of the aircraft determined from the Inertial Navigation System (INS) on board. By subtracting the aircraft altitude ($\mathbf{H}_a$) measured by GPS, the height of surface above the ellipsoid of the laser spot is then calculated as $\mathbf{H}_s=\mathbf{H}_a-\mathbf{H}$. To find surface height above the geoid, we need geoid height $\mathbf{H}_g=\mathbf{H}_s-\mathbf{N}$.

Chapter 2 Kalman Filter Algorithm in GPS Analysis

2.1 Introduction

One important task in geophysical study is to develop a data analysis method for estimation: the process of extracting desired geophysical information from geophysical measurements in the presence of errors. Like all other measurements, GPS observations contain errors. If the errors in the measurements are largely independent of each other, the classic least-squares method is very efficient for parameter estimation. In many geophysical measurements, however, processing system may also be dynamic (e.g. moving aircraft). Besides independent measurement errors, some system model error is time-correlated. In these cases we want to determine the optimum solution, or more generally, the state of the dynamic system in the presence of measurement errors. There are relationships, known and unknown, among the elements that describe the system. During the last four decades, various estimation methods have been developed to utilize the known information to compute the optimal estimates of the parameters of a dynamic system. By applying these optimal algorithms to the GPS data analysis, the estimators can account for the errors in measurements while taking account of the effects of disturbances and control actions on the system.

Theoretically, an optimal estimator is a computational algorithm that processes measurements to deduce a minimum error estimate of the state of a system by utilizing knowledge of system and measurement dynamics, and assumed statistics of system noise and measurement errors. Among the advantages of this type of algorithm are that it minimizes the estimation error in a well defined statistical sense and it utilizes all measurement data plus prior knowledge about the system. Also by using stochastic processes, we can incorporate some dynamic models in measurement solutions in an optimal fashion.

Researchers have been working on optimal estimation in stochastic systems for a long time. Wiener's work first used the filter techniques in stochastic systems but suffered from the

cumbersome calculations required to include all of the past data directly for each estimate [*Shinbert*, 1958]. Later, Kalman and others advanced optimal recursive filter techniques using state- space, time domain formulations [*Kalman*, 1960; *Kalman and Bucy*, 1961]. This new approach, now known as the Kalman filter, includes an estimation procedure that enables parameters to change during the interval over which data are collected.

Kalman filter is a set of mathematical equations that provides an efficient computational (recursive) solution of the least-squares method. The filter is powerful in several aspects: It supports estimations of past, present, and even future states; and it can do so even when the precise nature of the modeled system is unknown. The use of a random process along with deterministic signal descriptions and simple programming for modern high-speed digital computers are the keys. Used without stochastic parameters, the Kalman filter is a recursive solution to Gauss' original least-squares problem. The use of a dynamic system and stochastic model, however, enable the modern mathematics to characterize physical situations more closely.

Engineers and scientists have found that, in a typical navigation system, the errors propagate in essentially a linear manner and therefore linear combinations of these errors can be detected by a linear Kalman filter. The linear Kalman filter has been proven to be ideally suited for several navigation systems, such as that used for the NASA Apollo mission during the 1960s. The wide spread application of Kalman filtering in navigation has proven that this estimation technique is capable of providing robust estimation to states of a dynamic system, for example, positions and velocity of a moving object. Furthermore, Kalman filters can also provide estimates of the values of the realizations of the stochastic processes associated with the system, such as parametric models for the variations of the clocks and the atmospheric delays in GPS observations. A Kalman filter can provide useful estimates of different system error sources with significant correlation times [*Herring et al.* 1990; *Genrich and Minster*, 1991].

In algorithm and software design, the Kalman filter shows its advantage in computational efficiency and flexibility in operational design. As a time-varying filter, it can accommodate nonstationary error sources when their statistical behavior is known. Configuration changes in

the navigation system are relatively easy to deal with by programming changes. The Kalman filter provides for optimal use of any number, combination, and sequence of measurements. Indeed, it is the very foundation for time-dependent data analysis. Depending on the different purposes, the Kalman filter can be used in various geodetic measurements [*Herring et al.* 1990; *Genrich and Minster*, 1991]. Based on the previous experience and the nature of the kinematic GPS surveying for aircraft, we selected the Kalman filter as the core algorithm for data processing.

To apply the Kalman filter, we need to develop a model for the evaluation of the state of the system. We select a kinematic model in which the aircraft state vector is composed of position and velocity. In our model, the velocity of the aircraft is modeled as white noise. There are two possible types of models designs for Kalman filter's state process, dynamic or kinematic, depending on the nature of the system. A dynamic model utilizes the dynamic relationship of system parameters through time. In this system, normally the physical behavior is known or easily-modeled, such as an orbiting body acting under gravitational and other forces (e.g. drag and solar radiation pressure). Generally, in these types of models, the non-gravitational forces are treated as stochastic processes. If we have information about the acceleration of the aircraft, from the on-board accelerometers, for example, we could use a dynamic model in our analysis. In the GPS data analysis here, however, we will develop an algorithm that relies solely on the available GPS observation data. In the absence of acceleration information, it is very difficult to define consistent physical dynamic links between the positions of aircraft from epoch to epoch, considering the rapid changes of the aircraft's velocity and direction during the takeoff or landing. Thus we refer to the state process model designed for aircraft movement in our algorithm as "kinematic" rather than "dynamic".

In this chapter, we first describe the basic Kalman algorithm, and then discuss the physical model implemented in the GPS kinematic surveying and the stochastic model for estimates. The state formula will be established for data analysis.

2.2 Discrete-time Kalman Filter Algorithm

Kalman filtering encompasses an extensive area of estimation theory, but we will restrict our discussions to discrete time Kalman filters for a GPS kinematic surveying case. For more detail review of Kalman Filter algorithm, see *Kalman* 1960; *Kalman and Bucy*, 1961; *Liebelt*, 1967; *Gelb*, 1974; *Cohn* et al., 1981; *Lewis*, 1986; *Brown*, 1992; and *Jacobs*, 1993. The basic recurrence equations used to implement a Kalman filter estimator here are similar to those appearing in *Liebelt* [1967] and *Gelb* [1974].

The Kalman filter we used is for a linear dynamic system; i.e. we estimate the state of a discrete-time controlled process that is governed by linear stochastic difference equations. We collect an n-dimensional vector set of GPS measurements $\mathbf{Z}_t$ which could be pseudo-range (code) measurements (P1 and P2), carrier phase measurements (L1 and L2), or their linear combinations (which we will describe later). Through the linearization, the observation vector $\mathbf{Z}_t$ can be expressed in a linearized form of the equations which relate the GPS measurements to the parameters to be estimated, an m-dimensional state vector, $\mathbf{X}_t$. The state vector includes parameters representing the positions of aircraft, receiver clock errors, and atmospheric delays. Noise in the measurements is incorporated through an additive measurement noise $\mathbf{V}_t$. The general GPS measurement process is modeled as a measurement equation at time, t,

$$\boldsymbol{Z}_t = \boldsymbol{H}_t\boldsymbol{X}_t + \boldsymbol{V}_t \qquad (2.2.1)$$

$\mathbf{Z}_t$ is the vector of differences between the observed signals from each GPS satellite and their theoretical values calculated from aprior values of the parameters; $\mathbf{X}_t$ is the vector of adjustments to the *a priori* values of the parameters; $\mathbf{H}_t$ is the matrix of partial derivatives which relates the changes in parameter values to changes in the values of the measurement through the linear relationship; and $\mathbf{V}_t$ is a vector of residuals which represent the measurement noise in the GPS observations.

Typically a GPS measurement set like (2.2.1) contains redundant information when n is larger than m. Traditionally, a least-squares estimation is used to solve the above problem without statistical knowledge for its system process. In the kinematic mode of GPS surveys, the position of the aircraft is not static, so only the observations obtained at the same instant of time can be used with least-squares estimation. For a typical five to eight common satellites available for two GPS receivers, the amount of redundant observations is relatively small. Differing from the Least Square method, the Kalman filter takes other direction to approach this problem with "recursive estimation". For a time dependent measurement, the Kalman filter uses a prediction $\mathbf{X}_{t/t-1}$ vector calculated from a dynamic or kinematic model of its parameters $\mathbf{X}_{t-1}$ and $\mathbf{X}_t$ with a statistical model from the last epoch to the current epoch. Taking into account the statistical properties of $\mathbf{V}_t$ at the current time, Kalman filter calculates $\mathbf{X}_t$ values by maximizing the probability of measurements $\mathbf{Z}_t$. In this algorithm, the number of estimated parameters (state variables) is not limited by the measurements made at an individual epoch.

From the standpoint of classical physics, the future change of state variables in a dynamic system can be determined by its known physical state equation exclusively if there are no outside perturbations. Unfortunately, in the real world, external perturbations always exist and we can't get the exact description of the evolution of the dynamic system in the time domain. Thus the behavior of any real physical system could consist of two parts: one can be predicted by known equations; the other is a stochastic process with zero mean value. The dynamics of this physical system can be viewed as a Markov process and represented by the following state transition equation:

$$X_t = \Phi_{t,t-1} X_{t-1} + \Gamma_{t-1} W_{t-1} \qquad (2.2.2)$$

where $\Phi_{t,t-1}$ is the state transition matrix, which, operating on the state $\mathbf{X}_{t-1}$ at epoch $t-1$, gives the expected state $\mathbf{X}_t$ at epoch t. In a linear system, $\Phi_{t,t-1}$ represents the linear time derivative of state vectors $\mathbf{X}_{t-1}$ and $\mathbf{X}_t$ between the observation times; Γ_{t-1} is the constant matrix that defines the fixed relationship between $\mathbf{X}_t$ and $\mathbf{W}_{t-1}$. $\mathbf{W}_{t-1}$ is the vector of random perturbations affecting the state during the interval between epochs $t-1$ and t. The definition of the perturbation $\mathbf{W}_{t-1}$ can be flexible in Kalman filtering. For the nonstochastic parameters, $\mathbf{W}_{t-1}$ is defined to be zero, that is,

there are no random perturbations of the state with time. We restrict our discussion to the Markov class of stochastic processes whose state $\mathbf{W}_t$ at time t depends only on its state at time t-1 and on the change which occurs between t-1 and t. In this paper, the stochastic parameters typically include the components of the white noise, random walks, and integrated random walks. They are used to represent the variation of positions and velocities of the aircraft as well as fluctuations of the clocks and the atmospheric delays.

To form the Kalman filter estimator, statistical characterizations have to be made for the relationships among the process noise W_t and measurement noise V_t. To simply the problem, we make the following assumptions. These noises are assumed have a zero mean values and a standard deviation as shown in the equations

$$
\begin{aligned}
&E\{V\} = 0 \\
&E\{W\} = 0 \\
&E\{W_i W_j^T\} = Q_t \delta_{ij} \\
&E\{V_i V_j^T\} = R_t \delta_{ij} \\
&E\{W_i V_j^T\} = 0
\end{aligned}
\tag{2.2.3}
$$

where $\mathbf{Q}_t$ and $\mathbf{R}_t$ are values independent from the duration between time epochs t_i and t_j, δ_{ij} is the Dirac function, and $E\{\}$ denotes expectation. These assumptions require that the measurement process and the random motion of the system each be uncorrelated. Based on these assumptions, the random perturbations at any epochs are uncorrelated with those at any other epoch and have zero mean values. The current state of the system does not affect the random perturbations in the system at later epochs.

The Kalman filter estimation runs a process by using a form of feedback control: the filter estimates the process states forward at some time, then obtains feedback in the form of measurements to finish the estimates and keeps looping over time epochs. The main equations for the Kalman filter fall into two groups: time update equations (prediction) and measurement update equations (update). The prediction equations are responsible for projecting forward the current state and error covariance estimates in time to obtain the *a priori* estimates for the next time step. The measurement update equations are responsible for incorporating the new measurements into

the *a priori* estimates to obtain the improved *a posteriori* estimates. The whole procedure of Kalman filtering could consist of three parts: initialization, prediction, and update as in Figure 2.1

A. Initialization Step

We consider the dynamic system to commence at the initial epoch t_0. We assume its state vector is $\mathbf{X_0}$ and its covariance matrix $\mathbf{P_0}$. $\mathbf{X_0}$, $\mathbf{P_0}$ is known at t_0 as

$$E\{\mathbf{X}_0\} = \mathbf{u}_0; \quad E\{\mathbf{X_0}\mathbf{X_0}^T\} = \mathbf{P}_0; \tag{2.2.4}$$

$\mathbf{u_0}$ is the m-dimensional known vector. and $\mathbf{P_0}$ is an m by m symmetric matrix.

B. Prediction Step

The prediction step could be thought of as a time update equation. A dynamic propagation relationship like equation (2.2.2) allows us to make a forward prediction from any epoch *t-1* to *t*. The time dependent state vector $\mathbf{X_{t/t-1}}$ is projected with its dynamic state transition matrix $\Phi_{t,t-1}$ for epoch *t* from its values $\mathbf{X_{t-1}}$ at epoch *t-1*

$$X_{t/t-1} = \Phi_{t,t-1}X_{t-1} \tag{2.2.5}$$

Using the law of covariance propagation appeared to Equation (2.2.2) with the assumptions in equation (2.2.3), the predicted covariance $\mathbf{P_{t/t-1}}$ for $\mathbf{X_{t/t-1}}$ is

$$P_{t/t-1} = \Phi_{t,t-1}P_{t-1}\Phi^{T}_{t,t-1} + \Gamma_{t-1}Q^{T}_{t-1}\Gamma^{T}_{t-1} \tag{2.2.6}$$

The prediction step provides the best "guess" for the next time and its associated as variance based on the available information in current time *t*. The covariance is composed of two parts, the state uncertainty and the stochastic noise contribution during time between epochs *t-1* and *t*.

C. Update Step

The update step takes the incoming observations containing information on some components of the state vectors and estimates the best adjustments from predicted values. The state vector $\mathbf{X_t}$ is updated to epoch t with the Kalman gain matrix $\mathbf{K_t}$ distributing the differences between the current observations and the values predicted from the current state between the elements of the state vector. The difference in (2.2.7) is called the measurement innovation, or the residual. The residual reflects the discrepancy between the predicted measurement and the actual measurement.

$$X_t = X_{t/t-1} + K_t(Z_t - H_t X_{t/t-1}) \tag{2.2.7}$$

The key task during the measurement update is to compute the "Kalman gain," $\mathbf{K_t}$, specifying the weight to be given to the new observations. The Kalman gain $\mathbf{K_t}$ is calculated to be the gain or blending factor that minimizes the a posteriori error covariance.

$$K_t = P_{t/t-1} H_t^T \left[H_t P_{t/t-1} H_t^T + R_t \right]^{-1} \tag{2.2.8}$$

Then the covariance, $\mathbf{P_t}$, of the new estimates $\mathbf{X_t}$ is also updated from $\mathbf{P_{t/t-1}}$

$$P_t = [I - K_t H_t] P_{t/t-1} \tag{2.2.9}$$

The above Kalman filter estimation steps B and C are carried out sequentially and recursively (Figure 2.1). Equations (2.2.4) to (2.2.9) form a complete sequence for processing observations with the filter. When the computations at epoch t are completed, the sequence is repeated with quantities at epoch $t+2$ substituted for those at epoch $t+1$, and those at epochs t for those at epoch $t-1$. The sequence is repeated until all observations have been included. That is the basic forward Kalman filter process. This recursive nature is one of the very appealing features of the Kalman filter: it makes practical implementations much more feasible than an implementation of a Weiner filter which is designed to operate on all of the data directly for each estimate.

There are three types of applications of the Kalman filter for data analysis: smoothing, filtering, and predicting representing the process of providing solutions for past, current, and future epochs, respectively. Most of the applications in this thesis are filtering; i.e. providing solutions for the current epoch. For smoothing, the forward process is not complete because the estimates do not yet incorporated data from epoch $t+1$ forward. A backward process helps the smoothing but is not necessary in the filtering. For details of the application of a backward Kalman filter for geodetic measurement, readers can refer to *Herring et al*, [1990]. Strictly, the trajectory determination would be better if it comes from a smoothing processing. We use a single forward processing, however, which is much simpler for design. The use of a forward-only process is also based on other two considerations: one is that the potential future application of this software for real time use demands a design as a forward process; the other is that, with current precise phase measurements and robust Kalman filter process design, the results of forward processing is smooth and accurate enough without further backward smoothing.

2.3 GPS Observations

The fundamental measurements recorded by a GPS receiver are the differences in time or phase between the signals from GPS satellites and similar signals generated by the receiver. GPS signals are transmitted at two frequencies: L1 (1575.42 MHz) and L2 (1227.60 MHz). Several different combinations of GPS observations are used in this thesis for different purposes. We discuss the code pseudorange, carrier phase, and their useful linear combinations in this section.

2.3.1 Pseudorange Observations

The pseudoranges between the satellite and the receiver are derived from the difference in reception time and transmission time of an encoded satellite signal. Up to two pseudorandom noise (PRN) codes are modulated onto the two base carriers (L1 and L2). The L1 signal is modulated with a C/A (Course Acquisition) code and a higher rate P (Precision) code. The L2

signal does not have C/A code modulated on its carrier. When anti-spoofing is active (as it is for data analyzed here), the P code is further modulated with a code called the W code. The product of the P and W code is the Y code. The range provided by code tracking is called "pseudorange" because the value includes not only the true range from the satellite to the receiver but also the clock biases of satellite and receiver. Here, we denote by t_s the time given by the satellite clock at the transmission time and by t_r the time given by the receiver clock at signal reception. The pseudorange, $P(t_r)$, can be written in terms of the true range, ρ, the errors in the satellite clock, $\varepsilon(t_s)$, and receiver clock $\varepsilon(t_r)$, with the difference as $\Delta\delta=\varepsilon(t_r)-\varepsilon(t_s)$, and propagation effects, ρ_{atm}, and ionosphere, ρ_{ion}:

$$P(t_r) = \rho + c\Delta\delta + \rho_{atm} - \rho_{ion} + v \qquad (2.3.1)$$

where v represents the measurement noise.

The precision of a pseudorange derived from the code measurement is about 1% of the chip length (modulated code signal length; 300 m for the C/A code and 30 m for P code) which is roughly 0.3 meter for a P code pseudorange measurement. The pseudorange (code) measurement in this thesis is mainly used to obtain an approximate or initial position and to construct the ionosphere-free, geometry-free measurements such as the widelane, used in the ambiguity search and the detection of cycle slip as discussed in the next chapter.

2.3.2 Carrier Phase Observations

Carrier phase observations are obtained by comparing the phases between a signal transmitted by a satellite and a similar signal generated by a receiver. For a signal received at epoch t_r at site from GPS satellite emitted at t_s

$$\Phi(t_r) = \phi(t_r) - \theta(t_s) \qquad (2.3.2)$$

where $\Phi(t_r)$ is the observed carrier beat phase for the signal from one satellite; $\phi(t_r)$ is the

carrier phase received from the satellite; and $\theta(t_s)$ is the phase of the local oscillator of the GPS receiver.

Like the code measurement equation, equation (2.3.2) can be further written as

$$\Phi(t_r) = \frac{\rho}{\lambda} + \frac{c\Delta\delta}{\lambda} + \frac{\rho_{atm}}{\lambda} + \frac{\rho_{ion}}{\lambda} + \Phi_0 + v \qquad (2.3.3)$$

where the wavelength λ is for L1 or L2; the Φ_0 represents the initial bias in each phase measurement.

The precision of GPS phase observations is normally about 1% of the wavelength. One cycle of carrier phase is about 19 cm for L1 frequency and 24 cm for L2 frequency. The phase observation at L1, L2 or its linear combination L3 (see Section 2.3.4) are used for cm-level precision positioning. The software and algorithm developed here, however, are capable of dealing with either pseudo-range data, or the carrier phase data.

2.3.3 Single and Double Differencing

In local kinematic surveys, normally two GPS receivers are used: one is on the moving vehicle, the other is on the fixed station with known position. In analyzing data, we first form the difference of observations from the same GPS satellite in the two receivers. The difference between receivers is conventionally referred to as "receiver single difference"; it may be written for at the L1 and L2 frequencies as

$$\begin{aligned} \Delta\Phi_1 &= \frac{\Delta\rho}{\lambda_1} + \frac{\Delta\rho_{clk}}{\lambda_1} + \frac{\Delta\rho_{atm}}{\lambda_1} + \frac{\Delta\rho_{ion}}{\lambda_1} + \Delta\Phi_{01} + noise; \\ \Delta\Phi_2 &= \frac{\Delta\rho}{\lambda_2} + \frac{\Delta\rho_{clk}}{\lambda_2} + \frac{\Delta\rho_{atm}}{\lambda_2} + \frac{\lambda_2\Delta\rho_{ion}}{\lambda_1^2} + \Delta\Phi_{02} + noise \end{aligned} \qquad (2.3.4)$$

where λ_1 and $\lambda_1$are the wavelengths of L1 and L2. The only difference between equations 2.3.3

and 2.3.4 is that the signal ($\Delta\Phi$) and each term represent the single difference of values between two GPS receivers obtained from the same GPS satellite, for example, $\Delta\rho = \rho_{site1} - \rho_{site2}$. $\Delta\rho_{ion}$ is the differential dispersive ionospheric delay at the L1 frequency, and $\Delta\rho_{clk}$ is the difference in receiver clock offsets. $\Delta\Phi_{0i}$ is the initial phase difference in the satellites (fraction plus an integer number of cycles).

The satellite single difference between two satellites can be formed in the same way as the receiver single difference. By combining receiver and satellite single differences, a double difference can eliminate the receiver clock offset, $\Delta\rho_{clk}$ in the equation (2.3.4), and can be written as

$$\begin{aligned} \nabla\Delta\Phi_1 &= \frac{\nabla\Delta\rho}{\lambda_1} + \frac{\nabla\Delta\rho_{atm}}{\lambda_1} + \frac{\nabla\Delta\rho_{ion}}{\lambda_1} + \nabla\Delta N_1 + noise; \\ \nabla\Delta\Phi_2 &= \frac{\nabla\Delta\rho}{\lambda_2} + \frac{\nabla\Delta\rho_{atm}}{\lambda_2} + \frac{\lambda_2\nabla\Delta\rho_{ion}}{\lambda_1^2} + \nabla\Delta N_2 + noise \end{aligned} \qquad (2.3.5)$$

where ∇ represents the differences between two satellites. $\nabla\Delta N$ is called the "integer ambiguity" which represents the integer bias in the double difference of the phase measurements related to the same satellite in each frequency.

The propagation paths of signals to two GPS receivers separated by tens of kilometers are very close, reducing the sensitivity of the measurements to ionospheric and geometric effects. Differential GPS makes modeling of the measurements much simpler than for a global solution or a large scale network. In this thesis, we use either single or double difference for our calculations. The double difference method is similar to the single difference method except that the double difference remove receiver clock errors. When we use the stochastic process to trace the evolution of receiver clock offsets and average out the common constant non-integer parts of bias in single difference of phase data, single differencing generates almost the same results as double differencing. The double differencing method requires a reference satellite for differencing between satellites which makes the programming and data analysis more complex.

The residual information of single difference can also help us to identify the problematic observations with specific satellite. The double difference of carrier phase measurements is used in the ambiguity search which will be introduced in Chapter 3. In the analysis of Long Valley measurements in Chapter 4, we will use single difference of carrier phase most of time.

2.3.4 Linear Combinations of Observations

We use several linear combinations of the original carrier phase and/or code measurements during the data analyses. Those combinations are the ionosphere-free linear combination of carrier phase (L3), the extrawidelane geometry-free linear observation (L4), the widelane observation (L5) and the ionosphere-free and geometry-free combination of carrier phase and code observations (L6). (We adopt the nominative of [Beutler et. al, 1996]; other investigators [king and Bock, 1998] have used LC for L3 and LG for L4). We discuss them in this section. In the following discussion, L_1 and L_2 represents the phase observations in cycles (appropriate to the frequencies), and P_1 and P_2 represent the code measurements in meters at the L1 and L2 frequencies, respectively. For simplicity, we use the following symbols for the phase measurement at L1 and L2.

$$\begin{aligned} L1 &= \Phi_1 \\ L2 &= \Phi_2 \end{aligned} \qquad (2.3.6)$$

Ionosphere-free Linear Combination (L3)

The ionosphere is a dispersive medium, with the delay of a radio signal nearly proportional to the inverse square of the frequency *f*. The delay caused by propagation through the ionospheric layer in the atmosphere ranges from 6 to 50 m. The ionospheric delay in GPS signals has been studied for many years, [see for example, Wide et al. 1989]. The normal approach is to eliminate the ionospheric delay by forming a linear combination of the L1 and L2 phase measurements. In GPS data analysis, the combination is called as the "ionosphere-free

measurement", L3,

$$L3 = \frac{1}{1-\left(\frac{f_2}{f_1}\right)^2}L_1 - \frac{\frac{f_2}{f_1}}{1-\left(\frac{f_2}{f_1}\right)^2}L_2 \qquad (2.3.7)$$

This quantity is called ionosphere-free because the dominant frequency square dependence is eliminated. Higher order effects can be up to 30 mm in the single frequency L1 when the total electron content is extremely high [*Kleusberg*, 1986], but these are rare.

The same combination can also be applied to a linear combination of code observations in the distance units as

$$P3 = \frac{f_1^2}{f_1^2-f_2^2}P_1 - \frac{f_2^2}{f_1^2-f_2^2}P_2 \qquad (2.3.8)$$

Extrawidelane Linear Combination (L4)

Since l1 and L2 carry the same geometric information, we can construct a position-independent quantity by subtracting the L2 carrier phase observation multiplied by the frequency ratio from the L1 carrier phase observation

$$L4 = \Phi_{L1} - \frac{\lambda_2}{\lambda_1}\Phi_{L2} \qquad (2.3.9)$$

This quantity L4 is independent of the receiver clock as well as of geometry (orbits, station coordinates) and thus is often called geometry-free linear combination or extra-widelane. In the next chapter, we use this observable in our ambiguity search algorithm.

Widelane Observations (L5)

The widelane (L5) observation is another popular linear combination mainly used for

ambiguity and cycle slip fixing.The widelane observation is constructed by differencing L1 and L2 phase measurements directly. The L5 is a useful value for ambiguity resolution due to its wide wavelength.

$$L5 = \Phi_1 - \Phi_2 \tag{2.3.10}$$

MW Widelane Observations (L6)

The widelane observation in Equation (2.3.10) still contains the position information. Since the ionosphere affects code and phase measurements equally but with opposite sign (The ionosphere retards the group delay but advances the phase delay) in E.q. 2.2.1 and 2.2.3, we can eliminate the ionospheric effects and position information from the widelane observation. When both code and phase information are all available on two frequencies, we obtain the position-free and ionosphere-free value as

$$L6 = \Phi_1 - \Phi_2 - \frac{f_1 - f_2}{f_1 + f_2}\left(\frac{P_1}{\lambda_1} + \frac{P_2}{\lambda_2}\right) \tag{2.3.11}$$

This quantity is called the Melbourne-Wubbena combination (M-W widelane) by Beutler et al. [1996]. It combines the phase and code observations to eliminate the ionospheric, geometric and clock effects and will be used for the ambiguity initialization in our algorithm (Chapter 3).

2.4 Model

The application of the Kalman filter in the analysis of kinematic GPS data requires appropriate modeling not only of the measurements but also of the system process. Measurement modeling can provide appropriate values for some constant effects in the GPS measurements, such as the phase center offsets, and the approximate estimates close to their true values for linearization. For system process modeling, first, we must build up a linear dynamic system for the Kalman filter. secondly, to implement a Kalman filter successfully, appropriate stochastic

processes must be chosen to represent the behavior of parametric models. In this section, we discuss the use of both measurement and kinematic process modeling clock offset, atmospheric delay, and position changes.

The parameters used in a Kalman filter can be considered as stochastic ones. In a dynamic system, the statistical models adopted to represent a stochastic parameter should depend on the physics of the noise-generating process. Most of the underlying physics, however, is not well understood. The implementation of the ideal stochastic process sometimes yields a cumbersome solution so that an exact representation is often not practicable, if not prohibitive. Based on the experience of using the Kalman filter in other geodetic measurements such as VLBI [*Herring et al.*, 1990], we adopt three types of stochastic processes to represent the variations of parameters: white noise, random walk, and integrated random walk.

Depending on the type of data used, pseudorange or carrier phase, the GPS measurement equation is either equation (2.3.1) or (2.3.3). If the ambiguity N is taken out of the carrier phase measurement equation (2.3.3), there is little difference in the treatment of the phase and range measurements. In the following discussion, we develop the state expression for both phase and range data, and leave the ambiguity solution until the next chapter.

The improvement of GPS techniques has helped the use of the kinematic model in the Kalman filter algorithm. In contrast to a pure dynamic system, the solution of a kinematic system puts weight more heavily on the current measurements than on the past-time information. To obtain a reliable solution from differential GPS measurements at one epoch, at least four common satellites should be measurement from both GPS receivers. In our experiment, normally, there are five to eight satellites available for both the receivers on the ground and on the aircraft, although at times, the satellite availability does drop to four. The number of available satellites depends on the distance of the aircraft from the base station as well as on other factors. To keep a robust solution even in a satellite constellation with fewer satellites, we limit the number of parameters in our equations. With the differential measurements, the parameters in the observation models are the unknown position of the target, the receiver clock offset, and the atmospheric model.

In the state equations, the state vector X_t contains the position information P_t (both position and velocity, or position only), the clock difference effect $c\Delta\delta_t$, and the zenith delay adjustment D_t representing the difference in atmospheric delay between the fixed and moving receivers.

$$X_t = \begin{bmatrix} P_t \\ c\Delta\delta_t \\ D_t \end{bmatrix} \tag{2.4.1}$$

The stochastic process matrix is

$$W_t = \begin{bmatrix} W_p \\ W_{clk} \\ W_{atm} \end{bmatrix} \tag{2.4.2}$$

with coefficient matrix $\Gamma_t = \begin{bmatrix} I_p & 0 & 0 \\ 0 & I & 0 \\ 0 & 0 & I \end{bmatrix}$ (2.4.3)

The associated covariance matrix of the process noise is

$$Q_t = \begin{bmatrix} Q_p & 0 & 0 \\ 0 & Q_{clk} & 0 \\ 0 & 0 & Q_{atm} \end{bmatrix} \tag{2.4.4}$$

The measurement matrix is

$$H_t = \begin{bmatrix} H_\rho & H_{clk} & H_{atm} \end{bmatrix} \tag{2.4.5}$$

the state transition matrix is

$$\Phi_t = \begin{bmatrix} \Phi_p & 0 & 0 \\ 0 & I & 0 \\ 0 & 0 & I \end{bmatrix} \qquad (2.4.6)$$

We discuss each part of the model for position, atmospheric and clock separately.

2.4.1 Position and Velocity Model

The position and velocity model can be written as

$$\boldsymbol{P} = \begin{bmatrix} X \\ Y \\ Z \end{bmatrix} \qquad (2.4.7)$$

with a unit state transition matrix in three spatial directions as

$$\Phi_p = \begin{bmatrix} 1 & 0 & 0 \\ 0 & 1 & 0 \\ 0 & 0 & 1 \end{bmatrix} \qquad (2.4.8)$$

The geometric range ρ in equations (2.3.1) and (2.3.3) is the distance from the satellite to the receiver in a vacuum, the value of primary interest, because it contains the receiver position information. The range also contains information about the orbital position of the satellite, the receiver clock and satellite clock offsets. To approach the true range in the absent of accurate knowledge of satellite and receiver clock information, the *a priori* range value is therefore calculated iteratively. The measurement matrix H is

$$H_P = \begin{bmatrix} \frac{\partial \rho}{\partial x} & \frac{\partial \rho}{\partial y} & \frac{\partial \rho}{\partial z} \end{bmatrix} \qquad (2.4.9)$$

where ρ represents the range.

The post processing of GPS surveying with a kinematic model for the aircraft has few

constraints on its variation of acceleration and velocity. Thus the use of a stochastic process to model position depends on the behavior of the velocity of the aircraft during the entire flight. Normally a combination of white noise, random walk (integrated white noise) and integrated random walk can simulate most of process noises. Based on the navigation application of a Kalman filter by other instigators and several tests we had run with different combination of components from three standard processing noises, we use a white noise for the velocity stochastic model for Long Valley analysis. The position therefore behaves as a random walk.

To simply the simulation of the random behavior of positions, we assume the process noise components of the position are independent to each other in three dimensions of spatial coordinate system with the covariance matrix:

$$\boldsymbol{Q_p} = \begin{bmatrix} S_x\Delta t & 0 & 0 \\ 0 & S_y\Delta t & 0 \\ 0 & 0 & S_z\Delta t \end{bmatrix} \qquad (2.4.10)$$

where S_x, S_y and S_z are constant values; Δt is the time duration between the last time and current epochs.

2.4.2 Clock Model

In Equation 2.3.3, $c\Delta\delta$ is defined as the difference between the receiver and satellite clocks. The single difference between two receivers cancels the satellite clock offset, but the difference of receiver clock offsets still remains. In the Kalman filter, we implement a stochastic model for the variation of the clock. By choosing different stochastic processes, we have more flexibility in the choices to represent the behavior of clocks.

The clock model is very loose compared to the data noise and does not impose a large constraint on the solution. We use a random walk to simulate the clock's behaviors with

$$\boldsymbol{Q_{clk}} = [S_{clk}\Delta t] \qquad (2.4.11)$$

$$H_{clk} = 1 \qquad (2.4.12)$$

In our data processing, we calculate the common constant offset in all differential GPS signals which mainly due to the clock offset contribution before employing the processing of Kalman filter. This process removes any potential large jumps in the receiver clock without affecting parameter estimations. Therefore the clock stochastic model we implement here doesn't have to account for large and discontinuous changes. It just needs to be weakly constrained relative to the data noise.

2.4.3 Atmospheric Model

The nondispersive atmospheric delay is caused by refraction of the Earth's neutral atmosphere (troposphere and stratosphere). Unlike the dispersive effects of ionosphere, the atmospheric delay can't be eliminated by dual-band measurements. For measurements made in the zenith direction, the constituents of the atmosphere other than water vapor induce delays of approximately 2.3 m for a site at sea level. The water vapor contribution at the zenith direction is less, about 0.3 m, but is more volatile. The atmospheric delays are larger away from the zenith value and can reach more than 8 m for a GPS signal received at an elevation angle of 15 degrees.

Typically, the atmospheric effects on radio signals are treated by predicting an approximate value at the zenith, mapping this value to the elevation angle of the satellite, and then estimating the departure from the value as a zenith atmospheric delay. The model we implemented is a function of time and elevation angle, in the form

$$\rho_{atm}(t) = Z_d(t)m_d(t) + Z_w(t)m_w(t) \qquad (2.4.13)$$

where $Z_d(t)$ is the zenith delay due to the constituents in the atmosphere that are in hydrostatic equilibrium ("dry" delay), $Z_w(t)$ represents the wet part in zenith delay due to the dipole component of the refractivity of water vapor in the atmosphere (wet delay); $m_d(t)$ and $m_w(t)$ are

the mapping functions for hydrostatic and wet delay respectively [*Davis et al.*, 1985, Herring 1992]. The mapping function can be Marini's [*Marini*, 1974], CfA-2.2 [*Davis et al.*, 1985], MTT function [*Herring*, 1992], or NMF function [*Niell*, 1996]. We provide the different mapping functions in Appendix A.

The model values of tropospheric zenith delays $Z_d(t)$ and $Z_w(t)$ are calculated with a model from *Saastamoinen* [1972] model with typical and constant meteorological conditions at sea level with pressure 1013.25 mb, temperature 20°C and relative humidity 50%. The pressure at the height of the receiver is extrapolated by assuming hydrostatic equilibrium [*Davis*, 1986] and a lapse rate of -6.5° C/km [*Holton*, 1979]. In the flight test, the altitude of the aircraft could vary from zero to a few kilometers. The extrapolated zenith delay value is still approximate, so an atmospheric delay correction is needed when the atmospheric delay has large variations or the records of the meteorologic measurements are not correct.

The uncorrected atmospheric delay in (2.4.12) is modeled as a random walk in the zenith direction and the dry mapping function is used to map the zenith value to the elevation angle of viewing. The selection of the stochastic variance for zenith delay is a little difficult for kinematic GPS surveying because most of models developed for static ground sites but the aircraft moves in a zone covered 10 km vertically and 100 km horizontally. A thorough study of the statistical fluctuations of water vapor under the assumptions of Kolmogorov turbulence theory by *Treuhaft and Lanyi* [1987] shows that the structure function for the propagation delay in the zenith direction could be similar to that of random walk process in a limited frequency domain. This conclusion leads to the successful use of a random walk in VLBI measurements [*Herring et al.*, 1990]. The stochastic model is applied just to the moving receiver in the analysis here although our software can handle the atmospheric estimations on both fixed and moving receivers. Our test shows that the variation of atmospheric delay in zenith is limited to under 1 to 2 centimeter in most experiments.

The process noise for the atmospheric correction is

$$\boldsymbol{Q}_{atm} = [S_{atm}\Delta t] \qquad (2.4.13)$$

$$\boldsymbol{H}_{atm} = [M_d] \qquad (2.4.14)$$

where S_{atm} in unit of m^2/s and M_d is the dry mapping function. The mapping function we used in our algorithm is the MTT dry mapping function [*Herring, et al.*, 1992].

The precise modeling is important to keep the Kalman filter processing smoothly. To obtain high precise position estimates from the phase data, however, we still have to solve the ambiguity problem at first, which is addressed at the next chapter.

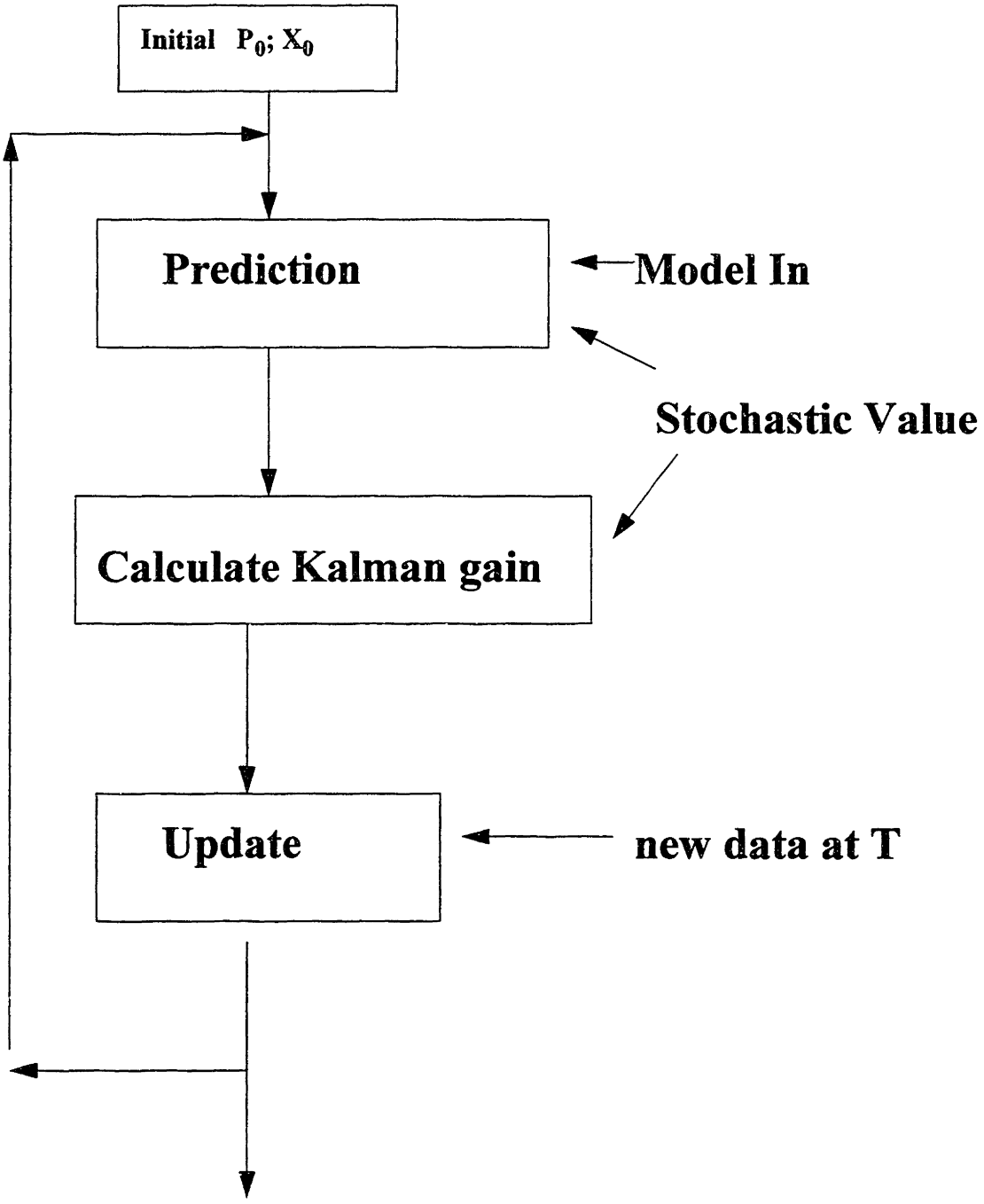

Figure 2.1 Diagram of the Kalman Filter processing

Reference

Beutler G., E. Brockmann, S. Frankhauser, W. Gurtner, J. Johnson, L. Mervart, M. Rothacher, S. Schaer, T. Springer, R. Weber, Bernese GPS Software, Version 4.0, Eds. by *L. Mervart and M. Rothacher, Astronomic Institute, Univ. of Berne,* 1996

Brown, R.G. and Y.C. Hwang, Introduction to Random Signals and Applied Kalman Filtering, *Second edition, John Wiley & Sons Gelb, A. (ed), 1974, Applied Optimal Estimation, MIT press, Cambridge Mass,* pp. 374, 1992.

Cohn, S., M. Ghil, and E. Isaacson, Optimal Interpolation and the Kalman Filter, *Proceedings of the Fifth Conference on Numerical Weather Prediction, Monterey California, American Meteorological Society, Boston Mass.,* 36 - 42, 1981

Davis, J,L., Atmospheric propagation effects on radio Interferometry, *Ph. D. Thesis, MIT, Cambridge, MA,* 1986

Davis, J. l., T. A. Herring, and I. I. Shapiro, Effects of atmospheric modeling error on determinations of baseline vectors from VLBI, *J. Geophys. Res.,* ***96,*** 643-650, 1991.

Gelb, A., Applied Optimal Estimation, 274 pp., *MIT Press, Cambridge, Mass.,* 1974.

Genrich, J. F. and J. B. Minster, Ship navigation for geophysical applications using kalman-filtered GPS fixes, *Geophysics*, **56**, 1961-1970, 1991.

Herring, T. A., The precision and accuracy of intercontinental distance determinations using radio Interferometry, *Ph. D. Thesis, M.I.T., Cambridge, MA,* 1983.

Herring, T. A., J. L. Davis and I. I. Shapiro, Geodesy by radio interferometry: The application of Kalman filtering to the analysis of VLBI data, *J. Geophys. Res.,* ***95,*** 12561-12581,1990.

Herring, T. A., modeling atmospheric delays in the analysis of space geodetic data, in *Refraction of trans-atmospheric Signals in Geodesy, eds. J. C. Munck and T. A. Spoelstra, Netherlands Geodetic Commission Publications in Geodesy,* ***36***, 157- 36,164, 1992.

Holton, I, R., An introduction to dynamic meteorology, *International Geophysics series, Vol. 16, Academic Press, London,* 1972.

Ifadis, I. I., The atmospheric delay of radio waves: Modeling the elevation dependence on a global scale, *Technical Report #38L, Chalmers University of Technology, Göteborg,*

Sweden, 1986

Jacobs, O.L.R, Introduction to Control Theory, *second edition, Oxford University Press,* 1993.

Julier, S. J., J. K. Uhlmann, and H. F. Durrant-Whyte, A New Approach for Filtering Nonlinear Systems. *Proceedings of the 1995 American Control Conference, Seattle, Washington,* 1628-1632, 1995.

Lewis, R.,Optimal Estimation with an Introduction to Stochastic Control Theory, *John Wiley & Sons, Inc.,* 1986.

Liebert, P.B., An introduction to optimal estimation, *Addison-Wesley, Reading, Mass.,* 273 pp., 1967.

Kalman, R.E., and Bucy, R.S., New results in Linear Filtering and Prediction Theory, *J. Basic Eng.,* 95-108, 1961.

Kalman, R.E., A new Approach to Linear Filtering and Prediction Problems, *J. Basic Eng.,* March, 35-46, 1960.

Kleusberg, A., ionospheric propagation effects in geodetic relative GPS positioning, *Man. Geo., **11,*** 256-261, 1986.

King, R. W., Documentation for the MIT GPS Analysis Software: GAMIT, *Mass. Institute of Technology,* 1997

Marini, J. W. and Murray, C. W., Correction of laser range tracking data for atmospheric refraction at elevations above 10 degrees, *NASA report X-591-73-351, Goddard Space Flight Center,* 1973.

Marini, J. W, Correction of satellite tracking data for an arbitrary atmospheric profile, *Radio Science,* 7, 223-231, 1972.

Niell, A. E., Vertical change and atmosphere correction in VLBI, in Proceedings of the AGU Chapman Conference on Geodetic VLBI: Monitoring Global Change, *NOAA Tech. Rep. NOS 137 NGS 49,* 428-436, U.S. Dept. of Commer., Rockville, Md., 1991.

Niell, A. E., Global mapping functions for the atmosphere delay at radio wavelengths, *J. Geophys. Res., **101, B2,*** 3227-3246, 1996.

Saastamoinen, Contribution to the theory of atmospheric refraction. *Bulletin Geodesique, Vol **107,*** 13-34, 1972

Shinbert, M., Optimization of Time-varying linear Systems with Nonstationary Inputs, *Trans. ASME, **80,*** 457-462, 1958

Truehaft, R. N., & G. E. Lanyi, The effect of the dynamic wet tropospheric radio interferometric measurements, *Radio Sci., 22,* 251-265, 1987.

Wild U., Beutler G., Gurtner W. and Rothacher M, Estimating the ionosphere using one or more dual frequency GPS receivers. In: *Proceedings of the Fifth International Geodetic Symposium on Satellite Positioning, Las Cruces, New Mexico, March 13-17, Vol. 2*, 724-736, 1989.

Chapter 3 Phase Ambiguity Resolution Strategy

3.1 Introduction

To meet the precision requirement of centimeter for the aircraft positioning in this experiment, we must use GPS carrier phase observations for accurate aircraft kinematic positioning. As indicated in the Chapter 2, the observed quantity of phase is the beat phase (i.e. the difference between the satellite-transmitted carrier and a receiver generated replica signal). When a receiver is turned on, the fractional beat phase is observed and an integer counter is initialized. During GPS signal tracking, the counter increments by one cycle whenever the fractional phase changes from 2π to 0. Therefore the accumulated phase recorded at a given epoch is the sum of the fractional phase observable signal and a phase bias. The bias contains a non-integer value plus the number of the unobserved full cycles of the phase observation, an inherent cycle ambiguity N of carrier phase measurement.

For geodetic measurements, time-varying phase observable contains two parts of information: interesting (i.e. position, time) and uninteresting (i.e. receiver clock drift and phase bias) components. For the correct use of GPS carry phase, the key is to eliminate the uninteresting parts from the observables. In a local GPS measurement, the differential technique generally cancels out most of model errors from the atmospheric, ionospheric and tide errors. Double differencing removes both satellite and receiver clock offsets. Single differencing removes satellite clock offsets and the remain receiver clock offset can also easily be estimated as a common value for all satellites. Unlike other factors which have common sources, the phase bias is receiver channel dependent. In GPS receiver, each channel initializes its own counter for one satellite so the phase biases can't be canceled by differencing and modeling. Resolving unknown phase bias becomes a fundamental requirement for accurate cm-level GPS aircraft kinematic positioning.

Theoretically, the phase bias of one channel in a receiver (one-way observation) is defined as a combination of cycle ambiguity N and a non-integer part. When double differences are formed, however, the non-integer part of the bias due t the unknown initial phase of the transmit-

ting and receiver clocks are eliminated. Hence we used double difference for the ambiguity resolution. The remaining integer part of bias is generally called ambiguity. For single differenced phase observables, the non-integer part of their biases can be calculated as a constant non-integer bias at the beginning of data processing; the remaining ambiguities are the same as the integer ambiguities in their double differences.

Without the exact determination of the integer ambiguity, precise positioning at the centimeter level using GPS phase observations cannot be achieved. It is easy to see that a mis-determination of one cycle of ambiguity could result in a few to tens of centimeter shift in the estimates of GPS position. Moreover, ambiguity resolution is more crucial in the kinematic surveying than in the static one. In static GPS analysis, we can separate the ambiguities from the receiver's fixed position by the geometric changes of satellites in a long time observation. In kinematic GPS surveying, the occupation of receiver in one location is short, even varies from epoch by epoch. The ambiguities are high-correlated with positions. Hence, the phase ambiguities must be correctly resolved beforehand in order to convert the phase observations into the precise ranges to the GPS satellites for accurate positioning.

Ambiguity resolution is necessary at three occasions: the beginning of the session (initial ambiguity), cycle slip occurrences, and the rising of a new satellite to be included in GPS analysis. The initial integer number N of cycles between the satellite and the receiver is typically unknown at the beginning of the receiver signal counting. The receiver may reset its initial ambiguities each time that it is turned on or sets initial numbers for a new satellite in one channel. This phase ambiguity N remains constant as long as no loss of signal lock occurs. Discontinuance may occur during an experiment when, for example, the receiver loses lock of signal when the satellite signal is blocked by some buildings or a wing of the aircraft during banking. In this event, the integer counter is re-initialized, causing a jump in the instantaneous accumulated phase by an integer number of cycles. This jump is called a cycle slip and is restricted to phase measurements.

The greatest difficulty for the ambiguity resolution is how to extract the integer cycle numbers from phase observations without the knowledge of precise position. The simplest ambiguity resolution process is the direct use of the ambiguity-free pseudorange measurements for L1

and L2 to obtain estimates of position and ionospheric delay, then to determine the ambiguity value [Blewitt, 1987]. The problem with the pseudorange measurement method is that the measurement error from receiver noise and signal multipathing are high. The use of single-epoch data can cause position errors around 1 meter, resulting in several or more cycle errors in ambiguities.

The widelane combination of phase observations, L5, is occasionally formed to help the ambiguity determination because its long wavelength (86 cm) reduces the impact of position errors on the ambiguity determination. The position-free difference between the associated code and the carrier measurements (L6) formed. Their averages over a time period are rounded to the nearest integer to obtain the ambiguities. However, the widelane (L6) still suffers the effects of the multipath errors and pseudorange measurement errors and can have variation of 1-2 cycles.

In these geometric approaches to ambiguity determination, the unmodeled errors will affect all estimated parameters. Many error sources affect the closeness of the estimated ambiguities to their integer values. Some of these sources could be, but are not limited to, the unmodeled errors in phase, varying atmospheric conditions, and satellite orbital errors. The ionosphere may also prevent a correct resolution of all ambiguities for a long baseline. In static surveying, data are collected over a long time span and used to smooth out the variation of unmodeled errors such as the multipath, ionospheric, and tropospheric effects on the ambiguity selection. When multiple stations are used, redundant baseline combinations between any two stations can also help for the search of ambiguities. Such a strategy is very efficient in static GPS measurements. In the kinematic GPS mod, however, these methods suffer some limitations, especially when the static initialization stage is short or does not exist. The major disadvantage of these techniques is the length of time needed to achieve the required accuracy. In kinematic surveying, the initial static stage before one starts moving usually does not last very long, sometime maybe just a few minutes. In our experiment, the code range data do not have enough time to allow the position solutions to approach the right position before the airplane takes off. Although such methods have been used in kinematic surveying [*Hatch*, 1986, *Bender and Larden*, 1985; *Melbourne*, 1985, *Wubbena*, 1989], they still require improvement in the accuracy of code measurements and the error models of the atmosphere and ionosphere to be effective over a long baseline.

In static differential GPS positioning, ambiguity resolution benefits from a significant change in satellite geometry and averaging of errors over the long observation time span. In kinematic positioning, such advantages vanish and make the ambiguity resolution much more difficult. Research has indicated that there is no reliable analytic way to obtain the ambiguity solution based in single epoch data in general condition. Also the integer characteristics of ambiguities make it hard to resolve ambiguities with other unknown parameters directly from measurements by optimum estimation. Generally, search techniques are needed.

During the last 10 years, numerical studies have been conducted for the "on-the-fly" ambiguity resolution which does not depend on the geodetic positions. A number of fast ambiguity-search techniques have been published. Among the techniques, we have, ambiguity mapping function method [*Remondi,* 1992; *Madar*, 1992]; least squares ambiguity search techniques [*Hatch*, 1990 and 1991; *Lachapelle*, 1992]; fast ambiguity resolution approach [*Frei and Beutler*, 1990]; optimal Cholesky decomposition algorithm [*Landau and Euler,* 1992]; ambiguity transform method [*Teunissen*, 1994 and 1995]; dual frequency method [*Abidin et al.*, 1992 and *Abidin*, 1993]; integer nonlinear programming method [*Wei and Schwarz*, 1995] and others. These ambiguity resolution techniques have common aspects. They are all applied to the initial ambiguity resolution and have some search strategy for the best ambiguity combination. The differences among them are mainly on how to execute such a search strategy. The detailed introduction and discussion for these methods could be very long and exhausting and we are not going to discuss these techniques in detail in this thesis. The major differences between these techniques fall into three categories: the data type or information utilized for the ambiguity search, the search domain and strategy, and the verification criterion. Without some means for classifying the algorithm employed, it is virtually impossible to evaluate their relative merit.

Many ambiguity-search methods have been developed to improve the computational speed of the ambiguity-search process. When high memory costs were high and CPU speed was low, minimizing the computations was important for real time solutions, especially for single frequency solutions which require a large number of ambiguity combinations for testing. However, an algorithm which results in fewer computations does not reduce the time span needed for the verification of the chosen ambiguities. In our case, the kinematic surveying for Long Valley

project is the post-time process, not the real time process. Thus the speed of computation for the ambiguity solution which many authors have addressed, is not our greatest concern.

Most above methods are also developed under the fine test environment which implies the ionospheric, atmospheric, multipathing effects are negligible. The applications of these method normally limit the kinematic moving within 10 km for local GPS differential surveying. In a 100 km horizontal and 10 km vertical scale region the aircraft was flying, some of these assumptions are impracticable. It is not surprise that some of methods failed to generate promising results in our initial trials. We feel the strong need to develop an ambiguity search algorithm for aircraft positioning to be not only fast but also reliable -- having the capability to deal with complex environmental conditions.

In this thesis, we will develop our own ambiguity strategy. One of our aims is to develop an ambiguity resolution strategy that is reliable and unique regardless of all test conditions. We want to develop robust methods for dealing with "bad" data so that the maximum amount of observables can be used for positioning. The other goal is to reduce time span needed for ambiguity determination. From our purpose, reducing the computation time is less important than minimizing the time span of data that must be accumulated before the ambiguities can be resolved reliably. Although our method is based on previous studies, we will not restrict ourselves to any specific techniques that have been developed. In this chapter, we design two different and efficient ways to deal with different ambiguity situations. We firstly developed a position-free ambiguity search technique used for ambiguity initialization and re-initialization. Then we develop a fast method to check and fix the cycle slips during a flight and to estimate the ambiguities for new satellites that rise during a flight.

3.2 Initial Ambiguity Search Strategy

3.2.1 Utilization of Dual Frequency Information

For convenience, we rewrite the double difference equation (2.3.5) as (3.2.1) for two frequency observations as

$$\begin{aligned} \nabla\Delta\Phi_1 &= \frac{\nabla\Delta\rho}{\lambda_1} + \frac{\nabla\Delta\rho_{atm}}{\lambda_1} + \frac{\nabla\Delta\rho_{ion}}{\lambda_1} + \nabla\Delta N_1 + noise; \\ \nabla\Delta\Phi_2 &= \frac{\nabla\Delta\rho}{\lambda_2} + \frac{\nabla\Delta\rho_{atm}}{\lambda_2} + \frac{\lambda_2\nabla\Delta\rho_{ion}}{\lambda_1^2} + \nabla\Delta N_2 + noise \end{aligned} \qquad (3.2.1)$$

Ambiguity resolution on kinematic GPS measurements can be carried out in different search dimensions. Generally there are two possible search spaces: the physical three-dimensional position space ($\Delta\rho$s in equation 3.2.1) and the multi-dimensional mathematical integer ambiguity space (ΔNs in equation 3.2.1). The position-space search is simple to implement. It tests numerical positions in a 3D space centered on an initial position. The best ambiguity candidates are chosen based on the position that has minimum sum of residuals for all observations. The shortcoming of the position space search is that it is very time consuming and the search result is highly dependent on the initial position precision and search step size. Either a too large step size can miss the right position point or a too small step size can increase the computing time cubically. Thus its application in kinematic positioning is limited. Most approaches are performed on the ambiguity space (ΔN).

More recent ambiguity searches use the ambiguity space, which does not have the step size selection problem. Generally the best way to estimate ambiguities is to estimate them simultaneously with other parameters from the phase measurements directly. Assuming a bias-free noise distribution, the integer ambiguities are determined by minimizing the *a posteriori* error variance when all ambiguity integers, position parameters, and other model parameters have been estimated. The greatest complication comes from the integer constraint, which violates the general rules of minimum residual sum if the least square method is applied directly with

equation (2.3.1). Due to this constraint, there is no unique analytical solution for the integer ambiguity [*Wei & Schwarz*, 1995]. Therefore the influence of individual integer combinations on the total error residual has to be computed separately and a search technique is necessary.

The use of double differences of the phase observations poses another problem. The double differencing eliminates most common error sources such as receiver clock offset, which is favorable for ambiguity determination, but suffers a disadvantage in the statistically high correlation between estimated ambiguities. Some strategies have been developed such as the ambiguity transform method to decorrelate the ambiguities [*Teunissen*, 1994 and 1995]. However, there is no reliable transform matrix developed for all circumstances right now.

Although the definition and construction of the ambiguity search are different for different search methods, the core of the search techniques is the same: how to utilize available information to find the "optimal" solution related to minimum observation and model errors. The pseudorange or carrier phases can be corrupted by system noise and model errors such as orbital errors, atmospheric effects, multipath effects. Range and phase observations are sensitive to different error sources. Useful information includes dual frequency observations in L1 and L2, the space geometry constraints from various satellites, the time change of satellite geometry structure, and the noise level of system and model errors. The linear combination L3 in equation 2.3.7 should improve the determination of frequency dependent ionospheric effects for long baselines. The geometric structure of available satellites with respect to the receiver and its time change will provide the error information related to observation in the different directions. Therefore, if we could utilize all of the available information contained in the GPS measurements, we would be able to resolve the carrier phase integer ambiguity more reliably and faster.

3.2.2 Strategy of Initial Ambiguity Search

There is not a simple way to develop a comprehensive approach for ambiguity search considering the complex field conditions in which GPS surveys performed. We have to design a

procedure that is able to cover the whole process with detection and validation of the ambiguity selections. There are two aspects in a determination process for initial ambiguity search: selection and validation. For ambiguity set selection, the work can be further divided into two steps: selection of search space and the improvement of search techniques. The development of search technique focuses on not only the fast and accurate convergence of ambiguity search space, but also the reduction of search time duration. In this thesis, we blend several techniques developed in the last few years into a reliable and fast search process.

To achieve the goals for comprehensive search and validation procedure, we make an ambiguity search in the ambiguity space and break the procedure into the following five steps:

1. Selection of an initial search center
2. Selection of a search space
3. Reduction of search candidates by integer constraint in two frequencies
4. Geometric search for the best candidates
5. Significance check and verification

Step 1. Selection of an Initial Search Center

The accuracy of a search center selection will determine the scale size of the search space in the multi-dimensional ambiguity space. In order to construct a small ambiguity search space that includes the correct ambiguities, we should select the initial ambiguities to approach the correct ones as closely as possible. In the static GPS surveying, a prior position is typically accurate to about 1 meter, sometimes even to 10 centimeters. Such a highly accurate position provides an ideal center for the initial ambiguities in search space. The initial ambiguities are calculated, and rounded to the nearest integer after the adjustment of prior position, clock and other parameters. In the case of kinematic positioning, however, the moving receiver is usually set up temporarily, not near a known benchmark. Most of the time, a high quality initial position is out of the question.

Several methods have been developed to determine the initial ambiguities. One approach

is to take advantage of the ambiguity-free pseudorange measurement for initial positioning. We re-write equation of 2.3.1 as

$$P_1 = \rho + \rho_{atm} + c\Delta\delta + \frac{\kappa}{f_1^2}$$
$$P_2 = \rho + \rho_{atm} + c\Delta\delta + \frac{\kappa}{f_2^2} \qquad (3.2.2)$$

where κ is a direction-related ionospheric value and varies with time.

Under Anti-Spoofing (AS), as we have already been discussed, the code measurements on both frequencies are noisy and don't provide enough accuracy of the initial position to resolve the carrier phase ambiguities directly [*Yang and Goad*, 1994]. Figure 3.1 shows some behavior of code measurements compared to phase measurements during the static portion of the Sept. 13, 1993, Long Valley mission. During this time span, the aircraft is still sitting on the ground. The position estimates vary by 1 to 2 meters. Considering the 19 cm wavelength of L1, a two-meter position bias translates into more than 10 cycles in the initial ambiguity guess. This variation is caused by the noise level of the code measurements and the ionosphere. Moreover, the smoothness of the curve in Figure 3.1 suggests more multipath effects rather than the receiver noise. The noise level of code measurements is larger than that for phase measurements because resolution and multipath are proportional to the wavelength. Thus, even if the AS is turned off in the future, the code measurement is a poor choice for the initial ambiguity guess. The search size in one dimension of ambiguity space would be 15 cycles if the position errors are 3 meters from an instantaneous code measurement.

Another approach is to utilize position-free observation combinations. In the position related methods, errors of position determination directly affect the search of initial ambiguities, especially when the solution is reset on the fly.

The forms of carrier phase observations in equation (2.3.3) could be written explicitly in each frequency L1 and L2 as

$$\lambda_{L1}\Phi_{L1} = \rho + \rho_{atm} + c\Delta\delta_1 - \frac{\kappa}{f_{L1}^2} + \lambda_{L1}\Phi_{01};$$
$$\lambda_{L2}\Phi_{L2} = \rho + \rho_{atm} + c\Delta\delta_2 - \frac{\kappa}{f_{L2}^2} + \lambda_{L2}\Phi_{02} \qquad (3.2.3)$$

For simplicity, we write the dual frequency phase combinations for a single receiver and a single satellite, but in practice we use single and double differences as we described in section 2.3.3. The fourth terms in equation (3.2.3) are the ionospheric effects on dual frequency data.

We modify extrawidelane L4 observation in equation (2.3.9) by using (3.2.3) to get

$$L4 = N_1 - \frac{\lambda_2}{\lambda_1}N_2 - \frac{\kappa}{c\lambda_1}\left(\frac{1}{f_1^2} - \frac{1}{f_2^2}\right) \qquad (3.2.4)$$

This is a special form of the dual frequency combination often referred to as the ionosphere residual by some authors [e.q., *Goad*, 1986]. The right-hand side of equation (3.2.4) shows that the residual contains only the L1 and L2 ambiguities and the ionospheric delay. Moreover, the contribution of the ionosphere is reduced by 65%. by the factor $\left(\frac{1}{f_1^2} - \frac{1}{f_2^2}\right)$.

We re-write equation (3.2.4) as

$$N_1 - \frac{\lambda_2}{\lambda_1}N_2 = L4 + \frac{\kappa}{c\lambda_1}\left(\frac{1}{f_1^2} - \frac{1}{f_2^2}\right) \qquad (3.2.5)$$

Equation (3.2.5) displays the frequency relationship directly and exclusively between the L1 and L2 ambiguity for each satellite from the phase observations. If there were no cycle slips, the temporal variations of the ionospheric residual in equation (3.2.5) would be small for short baselines and normal ionospheric conditions. Thus this combination of ambiguities will be close to constant. In our experiment, the average variation size of the extrawidelane ambiguities is around 0.3 to 0.7 cycles for most of satellites (Table 3.1 and Figure 3.2). A reliable estimate of

$_1 - \frac{\lambda_2}{\lambda_1} N_2$ can be obtained from a time average.

The other position-free ambiguity quantity is the W-M widelane observable (Eq. 2.3.11) which introduces noise from pseudorange measurements but eliminates ionospheric effects. The widelane ambiguity is

$$N_w = L6 = N_1 - N_2 \tag{3.2.6}$$

The residual left in equation (3.2.6) reflects mainly multipath effects and noise in the range data. Barring strong multipath effects, the RMS of the widelane ambiguity in equation (3.2.6) is usually one cycle or less.

We used both equations (3.2.5) and (3.2.6) to estimate the ambiguities N_1 and N_2 by matrix transformation. The advantage of this method is that all quantities used are insensitive to position, resulting in an initial ambiguity that is independent of errors in the starting position. Also the position-free method allows the average of all the data acquired in the session to be used to estimate the L1 and L2 ambiguities provided there are no cycle slips. The averages give us a reasonable estimates of ambiguities but not pin-point accurate values we need. Table 3.1 shows the average of widelane N6 (from L6) and extrawidelane ambiguity N4 (from geometry-free L4) over the 3 plus hour flight experiment on Sept. 13, 1993. Most of their predicted ambiguities of L_1 and L_2 are close to the correct ones within 1 cycle, showing that the multipath and ionospheric effects can be smoothed out with long time averaging. However, there are initial ambiguity guesses that are incorrect by as much as 4 cycles. The abnormal values are all related to the shorter observation time and low elevation angle of satellites. The departure from their true values of ambiguities results from The high correlation of these two equations (3.2.5) and (3.2.6) in which the coefficients of equations are close to each other. Therefore this method generates a good initial ambiguity guess but a search technique is still needed. Propagation of the uncertainties calculated into the N_1 and N_2 estimates leads us to set the search cycles for each satellite to between 7 and 12 cycles around their search centers. The range depends on the RMS of the L4 and L6 values over the entire flight experiment. In order to mitigate the multipath

problems, we don't use low elevation angle satellites in the initial search. The ambiguities for low elevation angle satellites are resolved using the L4 and L6 observations after all other satellite's ambiguities are settled down. This approach affects our selection of primary satellites to be used in the initial search.

The cycle slip can corrupt the averaging of L4 and L6. The high correlation of these two equations (3.2.5) and (3.2.6) also makes it somewhat difficult to determine whether the cycle slip was on L1, L2, or both. Therefore, we select the time period not covering any cycle slips to do the averaging.

Step 2 Choice of the Primary Satellites

We initially choose some GPS satellites, which are above a specific elevation angle limit (normally 15^{o}), as primary satellites. Through this choice, we avoid the observations possibly corrupted by the low elevation angle multipath and possibly atmospheric and ionospheric delay modeling errors (see, for example, Remondi, [1990a and 1990b]). When the ambiguity search is computed with this group of satellites, the lowest elevation angle satellite is removed from primary group and the search repeats to ensure the ambiguities are not affected by removing one satellite. If they do disagree, another low elevation angle satellite is removed and the same consistently check is applied. If the number of primary satellites is reduced to 4, the process is stopped and we move the initial ambiguity search forward to a new epoch which provides enough satellites.

Step 3. Reduction of Search by L1/L2 integer constraint

The integer character of the ambiguities can be used to reduce the search space if dual frequency observations are used (*Lu et. al.*, 1995]. From equations (3.2.1), the double differenced observation equations for L1 and L2 carrier phase observations can be simply written (assuming the ionospheric delay is small) as

$$\nabla\Delta\Phi_1 = \frac{\nabla\Delta\rho}{\lambda_{L1}} + \nabla\Delta N_1 + noise;$$
$$\nabla\Delta\Phi_2 = \frac{\nabla\Delta\rho}{\lambda_{L2}} + \nabla\Delta N_2 + noise \qquad (3.2.7)$$

By eliminating the range term, we can obtain the pure relationship between the phase observations and their integer ambiguities.

$$\nabla\Delta N_2 = \nabla\Delta\Phi_2 - \frac{\lambda_{L1}}{\lambda_{L2}}(\nabla\Delta\Phi_1 - \nabla\Delta N_1) + noise \qquad (3.2.8)$$

For each potential integer of the double difference ambiguity in L1, we can use equation (3.2.8) to find a corresponding one in L2. If this value is not close to an integer, it is excluded from the candidates immediately. When phase noise is around 0.1 cycle on both phase observations, the resultant uncertainty in $\nabla\Delta N_1$ is 0.13 cycle. *Lu et al.* [1995] used this criteria to reduce the number of candidate L2 ambiguities from 30 to 10 for each satellite. For a multi-dimensional ambiguity space search, this method can save significant time.

In our work, we used the same constraint on the L2 integer ambiguity pair but modified the noise assumption to allow for noisier observations. The weakness of this method is that it neglects ionospheric effects which can easily exceed the 0.1 cycle threshold for receivers separated of a few tens of kilometers. The ionospheric effects on the signals are fairly complicated quantities because they depend not only on the elevation and azimuth angles of the observed satellites but also on the sunspot activity's seasonal and diurnal variations [*Finn and Mattewman*, 1989]. In our analyses, we allow the L2 threshold to vary depending on the magnitude of the ionospheric and other errors. The magnitude of these errors varies in various environments, so the determination of the threshold values should depend on the test conditions. A large threshold results in many false candidates, resulting in a volatile ranking during the geometric search as we'll discuss in the next section; On the other hand, a tight threshold should reject the correct ambiguity set. Because of the ionosphere effects, this threshold may be larger with longer baselines. In our test, with a 1-km baseline, a 0.1-0.15 cycle constraint reduced the ambiguity candidates from 20-30 to 5-10 for each satellite. For a 6-dimensional ambiguity search

space when six satellites are used, the total search number is reduced from 10^8 to 10^4. For a 70-km baseline and a calm ionosphere, we used a 0.25 cycle threshold for a calm ionosphere. For a long baseline, an approximate estimate of ionospheric model should be used to estimate the large parts of ionospheric effects, and low elevation angle observables should be excluded. In the worst situation when the ionospheric effects exceed one cycle, the threshold is set to larger than 0.5 effectively removing the lane constraint. In this case, we have to enlarge the search range but will not exclude out the correct ambiguities due to too tight a constraint.

Step 4. Geometric Search for the Best Candidates

After filtering of the ambiguity constraints (Step 2 and 3), the candidates are combined for a geometric search. All possible combinations of the candidate ambiguities are considered as known values and substituted into subsequent adjustments. Double differenced phase measurements (Equation 3.2.1) are formed to estimate the position and other parameters by using a Kalman filter. With the estimated positions, the root mean square (RMS) scatter of the residuals and the Mader function for each ambiguity set are computed. The RMS is computed with only the primary satellites while the Mader sum is computed for all satellites regardless of their participation in the geometric search at each epoch. The potential ambiguities are ranked by the RMS scatter of primary satellites phase residuals and the Mader sum.

Step 5. Significance Check and Verification

The validation of the phase ambiguity search is as important as the selection of the search method. We have to confirm that the ambiguities selected are the reliable and correct ones. The validation is generally made by comparison of the post-fit phase residual values between the solutions from ambiguity candidates which result in the least residuals and the second least residuals. We use various combinations of two metrics to assess the reliability and to rank the ambiguity choices: (a) the RMS scatter of the phase residuals; and b) the Mader function, defined as

$$M = \frac{\sum_{i}^{N} \cos\left(\Phi_i - \frac{2\pi}{\lambda}\Delta\rho\right)}{N} \qquad (3.2.9)$$

where N is the total number of GPS satellites used in the measurements. a cosine mapping function [*Mader*, 1990 and 1992] is used to remove the unknown integer in the non-primary satellites (see below for definition of primary satellite). Equation (3.2.9) is a modification of the original Mader function [Mader, 1990]. In the absence of model errors and noise, M in equation (3.2.9) equals its maximum value of 1. In the use of Mader function, the ambiguity candidate sets are sorted and ranked with their Mader value from maximum to minimum. The Mader function is used to check the quality of geometric solution and has the advantage over the RMS fit in that all phase data at a given epoch can be used even if the ambiguities are not yet resolved. In our thesis, we use both metrics to form a new validation function to speed up the validation procedure.

Validation procedure is used to find out the best combination of ambiguities when enough data are accumulated. This procedure continues until the optimal integer ambiguities are identified. Accumulation of too few epochs (i.e. less than 10) may fail to obtain a reliable statistical judgement for its time averaged values. In the case of double differences, the receiver clock is eliminated and only 3 parameters of position remain in the equations. If there is one (fifth) or more redundant satellites available, the correct integer ambiguity from any satellites should give a unique position. Least square technique is generally applied to estimate the positions with each trial ambiguity set. Kalman filter technique was also used [*Loomis*,1989]. Regardless of the estimation method, the RMS scatter of the phase residuals is examined. For the set of solutions, the integer combination giving the smallest root mean square error for the position is taken as the best estimate. In order to include the residual information of non-primary satellites in the validation, we use Mader function values of non-primary satellites (Equation 3.2.9) because the non-primary satellites do not take part into the search space and are without a trial ambiguity value. The ambiguity candidate sets are sorted and ranked with their Mader value from maximum to minimum. Generally, only the top 50 are kept for further validation tests.

Geometric constraints from redundant satellites play an important role in ambiguity resolution for most methods. If the number of primary satellites used for the search is identical to the total number of the available satellites, the ambiguity with maximum of the Mader function (M in equation 3.2.9) should be identical to that with the minimum RMS. Theoretically, the minimum RMS method will provide the best solution if there are no systematic errors. The latter requirement is rarely met in GPS observations. However, as has been pointed out (see *Borge & Forssell* [1994]), the correct integer ambiguity set may not minimize the instantaneous carrier phase residuals, but does minimize the time average of residuals. We adopt both the time average of the rank of the Mader value and the RMS scatter as selection criteria. In addition, we introduce the scatter of the RMS into the final rank which reveals the variations of the residuals as more epochs of data are included in the search. When the correct ambiguity sets are used in the solution, the Kalman filtering of equation (3.2.1) should not only have a minimum mean RMS, but also generate the smallest scatter of RMS values over time in all ambiguity candidates, provided that the assumption of Gaussian distribution of noise holds true. We'll discuss the detail Behavior of averaged RMS of the primary satellites, the Mader function and their scatters in the next section.

3.3 Tests for Initial Ambiguity Search

3.3.1 Application in Short Baselines

We have used our flight GPS data collected in the Long Valley experiments to test the ambiguity search algorithm implemented in our software. There are several important parameters needed to perform the ambiguity search. First, we choose the number of primary satellites to construct the multi-dimensional ambiguity space (Step 2). A 15° elevation cutoff angle is used for the observations but sometimes we don't allow all observations into the ambiguity space search. The primary satellites can be selected with a higher elevation angle cutoff to avoid the effects of multipath in some cases. Fewer primary satellites also results in a smaller search number. Second we choose the ambiguity search size for the search space. The number of cycle

searched on L1 is set to 9-15 around the search centers depending on the accuracy of initial guesses that we can obtain from the averages of the widelane (L6) and the geometry-free L4 over a long time span. This search creates a spatial window covering a cube of 2-3 meters around the search center. For an ambiguity space search with six primary satellites, the total number of the initial ambiguity combinations may be up to 10^8.

We use the integer ambiguity relationship between the L1 and L2 ambiguities to further reduce the search combination. The allowable errors in integer lane constraint for L1 and L2 pairs is normally set to 0.1- 0.15 cycle (in equation 3.2.7 of Step 3). The major part of these errors come from the difference of the ionospheric and tropospheric delays between the fixed base station and the moving GPS receiver. For most experiments here, the flight began with the aircraft sitting at the airport, which is just a few hundred meters away from the base station receiver. At such a short distance, the ionospheric and tropospheric delays on the differential GPS signals are not very significant, so a small number is used for the integer lane constraint for L1 and L2. Through the integer lane constraint, the search number reduces to 10^3-10^4 for the ambiguity space search. Each 0.05 cycle change in the lane constraint results in reduction of total search numbers by a factor of ten.

L1 is used for the geometric search considering the negligible ionospheric effects on such a short baseline. The number of validation epochs (Step 5) is flexible and varied from 10 up to 50 depends on the quality of data and the duration of each searching epoch is 5 - 10 seconds.

Figures 3.3-3.6 show an example of ambiguity search processing with our algorithm in the experiment of Sept. 13, 1993. The time interval used is 10 seconds, which is longer than the record interval (0.5 second). The longer interval can utilize more changes of the geometric structure of satellites. First, we examine the role of low elevation observations in the ambiguity search. In Figure 3.3, we compare the rank order of the top ambiguity candidates both in the sorting of the RMS of the primary satellites taking part in search (primary RMS rank) and in the sorting of the average Mader function (Mader rank). The Mader function is the value of M in equation (3.2.9) which contains residual information but eliminates the effect of uncorrected

ambiguities in the non-primary satellites. The primary RMS ranks from minimum to maximum but the Mader function ranks from maximum to minimum. If all the observations are included in primary satellites and there are no cycle slips, both ranks provide the same results. In Figure 3.3, we select the number of primary satellites as 5 while the total number of the observable satellites is 6 in order to check the impact of low elevation observations in the ambiguity search. It is very clear, for a short baseline, that the ionospheric and tropospheric effects on double difference observations are canceled almost completely. Thus the Mader function rank of the best ambiguity set is most reliable all the time (Figure 3.3). In contrast to the Mader function, the RMS sum of primary satellites does not rank in the top in every individual epoch during the search because of the higher correlation in the estimated parameters due to the use of only higher elevation data. Therefore, in the absence of multipath, the low elevation observations could improve the reliability of the ambiguity search.

Next we examine the behavior of the various statistics that comprise the criteria of Equation (3.2.10). In Figure 3.4 we plot for the top three candidate ambiguity sets three phase statistics: a) the RMS of the residuals at each epoch; b) the mean of the RMS values accumulated from all previous epochs; and c) the accumulated RMS of the epoch-to-epoch variation of the RMS. In this example, the top candidate set produces the lowest (best) value in all cases except for the individual-epoch statistic (a), for which it drops to second-lowest at three epochs (6, 9, and 10). In Figure 3.5 we plot for the top three candidate sets three statistics of the Mader function: a) the value at each epoch; b) the mean value from the last to the current epoch. In this example, the top candidate produces for every epoch the highest (best) value of the function and its accumulated mean and also the lowest variation from epoch-to-epoch.

As a specific criterion for selecting the correct ambiguities from a set of candidates, we follow the usual practice of forming the ratio of a statistical measure for the best set to that of the second best set. For both the phase residuals (primary satellites) and Mader Function (all satellites), a "true" ambiguity set usually results in a favorable ratio for both the accumulated means and the accumulated epoch-to -epoch variations. There are times, however, when the ratios for one or more of these quantities gives only a marginal preference for the best set; for example, the mean RMS values in Figure 3.4b. In order to provide the most robust selection of

ambiguities under varying conditions, we have defined a validation function which incorporates both the means and variations of the RMS and Mader function:

$$F=[R(\text{mean RMS}) + R(\text{var RMS}) + R(\text{acos}(M)) + R(\text{var (acos}(M))]/4 \qquad (3.2.10)$$

where R denotes the ratio of a particular measure for the second-best ambiguity set to that of the best, and measures to be used are the accumulated (mean) RMS of the phase residuals (Figure 3.4b), the accumulated RMS of the epoch-to-epoch variations of the phase residuals (Fig. 3.4c), the arc cosine of the accumulated mean Mader function (arc cosine of values in Fig 3.5b) and their epoch-to-epoch scatters (Fig 3.5c).

We plot in Figure 3.6 the value of our validation function, along with the values of the mean RMS of the phase residuals and mean Mader function, for the example shown in Figure 3.4 and 3.5. The results show that the combined function maintains a ratio greater than 4 throughout the first 18 epochs, whereas the ratio of phase-residual means drops below 2 and the ratio of Mader-function means drops to 3.

Choosing a cutoff ratio for deciding whether the best set of ambiguities is significantly better than the second best is problematic. ALthough several authors have used a formal F-test to determine the significance of the preference for a particular set, there is no statistical basis for assuming that the measure used (e.g., the mean RMS of the phase residuals) is independent for the two sets of ambiguities. Based on what, we have chosen a value of 2.

Figure 3.7 displays our estimated height of the aircraft on the ground calculated with the best ambiguity sets and the second best sets we obtained from our ambiguity search method. During this time period, the aircraft did not move but the position constraint of aircraft is set to be very loose (300 m $s^{-1/2}$ for process noise). The result with the best ambiguity sets is a very flat line with variation under 1 centimeter. However, it is not easy to distinguish the true position from the false position based on the information in short time. The "false" ambiguity set also generates a flat trace until a satellite dropped out of sight. The total residual geometric structure of observations has been changed, and the new geometric structure predicted a new "optimal"

solution 25 cm away from the former position. When the true ambiguities are found, the residual geometric structure contains the measurement noise only. A loss of a single satellite observation will not change the nature of Gaussian distribution of noise measurements if there are no significant errors in the low elevation observations being lost. The results of the solution should be independent of the number of satellites used in the solution.

3.3.2 Application for a Middle Range Baseline

Most current ambiguity search techniques provide reliable solutions with short baselines (< 10 km). With increasing ionospheric and tropospheric effects for a longer baseline, most of the strategies do not work well due to their "bias-free" (no ionospheric tropospheric, multipath errors) assumption. We have not relied on this assumption that many search techniques are based on. The method developed here tends to be more flexible in complex situations, such as multipath effects and ionospheric effects on long baselines. Although the constraint setting in our method is very flexible and we can adjust the setting to respond to different situations, how well it works still remains in question. Here, we do some tests with a middle range baseline (50~100km). In the Long Valley mission, the aircraft started and landed at the same airports all the time. The application of ambiguity search strategy with long baseline is useful although most kinematic surveying begin from the place near the base station. When the aircraft lands at other airports during flight tests, and sometimes the GPS receiver at the base station does not work well, we need to look for an alternate base station for which the benchmark is not so close to the airport. Considering all possible conditions, an ambiguity search strategy suitable for long baselines is still a need.

We tested our algorithm for longer baselines by using observations between benchmarks in Casa Biablo and Bishop separated by nearly 75 km. A GPS receiver is put on a permanent benchmark and data are sampled at 30 s interval. For a short baseline, the quantity κ in equation (3.2.3) is nearly the same for each site involved into the two-site differencing, and the ionospheric term cancels out. Over a long baseline, things are a little different; the κ values are not the same. However, the ionospheric effects can be removed from the formulation using the

linear combination L3 (LC) of the L1 and L2 observations. Here we replaced the L1 single frequency observation with the L3 observation to perform the geometric search in the ambiguity resolution. The RMS of phase residuals over 20 epochs is reduced from 27.8 mm to 22.5 mm for the true ambiguity sets, a dramatic improvement due to the use of L3. The scatter of the RMS also reduced from 11.3 mm/s to 10.1 mm/s.

It appears that the ionospheric and atmospheric effects do make the case more complicated than that for a short baseline. Figure 3.8, similar to Figure 3.4, shows the primary RMS rank of the top candidates for Casa Biablo-Bishop baseline. For some epochs, the true ambiguity does not even rank in the top 3 in the search, a result which is much worse than for the short baseline. Figures 3.9 and 3.10 show for the top three candidates in the ambiguity search the three phase residual, RMS and Mader function discussed in Section 3.3.1 and shown in Figure 3.4 and 3.5. It appears that if the phase data are significantly degraded by ionospheric errors, it will take a longer time to resolve the ambiguity. This is the typical problem when the distance between the reference receiver and aircraft is increased and the differential ionospheric effect increases. However, the ambiguity is fixed within 20 epochs. Our method of combining RMS and change rate of RMS shows its ability to deal with a middle range base line better than the use of RMS only (Figure 3.11).

In Figure 3.12-3.14 we show a more difficult situation for the same 75-km baseline. All settings for ambiguity search in Figures 3.12-3.14 are the same as those in Figures 3.9 -3.11 except the search time period of latter is half hour earlier. For this period, the best candidate and the second best candidate are only one cycle away in one low elevation satellite. With ionospheric effects absent in the ionosphere-free combination L3, this difference may mostly result from the different atmospheric or multipath effects on the two receivers during this time span. The double differencing does not eliminate all atmospheric effects at a longer baseline as it does at a short baseline. It takes an extremely long time to fix the ambiguity when only the average residuals are used for validation. The ratio of average RMS between the best ambiguity set and second best ambiguity set is below 1.3 even after a 20 epoch search. Again our validation function, which takes the average of RMS and Mader function as well as their scatter, demonstrates a better performance than the RMS-only criterion. Although the search time

generally lasts longer than in the short baseline cases, the ratio value of F in equation 3.2.10 keeps above the significant confidential level of 2 while the RMS-only method (dashed line in Figure 3. 14) never reaches the confidential level.

We compared the position of Bishop relative to Casa Biablo calculated by our kinematic algorithm with the positions estimated using static positioning given by the GAMIT software [*King and Bock*, 1997]. The results are shown in Figure 3.15. The horizontal positions are almost identical and their averaged differences are less than 1 cm. The vertical difference may result from the possible different models used in the two software such as a simplified phase center correction model in kinematic codes.

3.4 Ambiguity Resolution for New Satellites

When a rising satellite is acquired, its phase ambiguity bias is reset and estimated again. In this case, it is most efficient not to use the position-free search algorithm which is time consuming because we just need to resolve ambiguity for one satellite. With ambiguities of other satellites fixed, we can use the estimated position of the moving antenna from other satellites to determine the ambiguity value of the new satellite directly.

In the procedure used in our algorithm and software, we take the following approach: When a new satellite rises, we don't use its observations until the next epoch. At the epoch the new satellite rises above the elevation cutoff angle, we calculate position by using the phase observations from other satellites. Also ionospheric effect on the zenith direction is calculated based on a symmetric model and translate into the direction of the new satellite's signal.

$$\rho_{ion} = \frac{40.3R_E}{(R_E + h_{ion})f^2 \sin\varepsilon} TVEC \qquad (3.4.1)$$

where f is the frequency and ε is the elevation angle of ray over the surface; $TVEC$ is the total vertical electron content of the ionosphere; ρ_{ion} is the ionospheric delay at this ray; R_E is the radius of the earth and h_{ion} is the averaged height of ionospheric layer [*Hofmann-Wellenhof et.*

al., 1995]. A value of 300 - 400 km is typically set to the h_{ion} with 350 km value used in this thesis [Wild et al., 1991]. The ambiguities at two frequencies are obtained after removing the influence of ionospheric effects and position changes. Also the widelane and extrawidelane ambiguity are used to validate these new ambiguities for possible asymmetric ionospheric effects. Theoretically a single observation should not change the residual distribution dramatically if the error in the phase represents only measurement noise only. So this method depends heavily on the position precision, more clearly, on the accuracy of ambiguity solution of other satellites involved.

The rising or setting of a satellite during processing also provides a good opportunity to judge the accuracy of the initial ambiguity search techniques. If our search technique does not obtain the best correct set of ambiguities, even if the results are just one cycle away for only one satellite, the residuals contain the systematic errors from uncorrected positions and thus do not have the Gaussian distribution expected for unbiased measurement noise. The positions of the aircraft are also affected by the incorrect ambiguities. When a new satellite is added or one drops out, it changes the entire residual space structure dramatically. The result is a discontinuity in position as we showed (Figure 3.7). In our solution, when the correct ambiguity set is obtained, the residual does not show large phase jumps or jumps in positions when the aircraft does not move. When the aircraft is flying, this change could be mixed up with the true movement of the aircraft and degrade the precision of position determination.

Using the residuals to generate the ambiguities for a new satellite is potentially sensitive to errors in the models for the atmosphere, ionosphere, orbits and multipath. When the simple method fails to generate a correct answer, a discontinuity will appear in the time variation of residuals from other satellites. In such a situation, we can turn on our ambiguity search algorithm to fix the ambiguity. We also use the search algorithm if the on-board GPS receiver loses power and resets the signal reception during flight.

3.5 Cycle Slip Detection and Fixing

An ambiguity break, a so-called cycle slip, occurs when the phase observation jumps by a few or more cycles in L1 frequency, L2 frequency, or in both. The detection of small cycle slips is potentially difficult because sometimes it is hard to distinguish the cycle slips from a single outlier phase value. A single outlier is defined as an isolated shift of observation which lasts only one or a few epochs whereas a cycle slip causes a permanent constant shift in the observation. The variation of position with time in a kinematic survey makes it hard to use the a single observation for the detection of the cycle slips. In a static GPS analysis, it is possible to scan the pre-processed residuals with an *a priori* model for data quality control and to detect potential cycle slips at any epochs. In a kinematic survey, the pre-fit residuals are of little use because of the movement of one receiver. We can use the two geometry-free linear combinations of phase data: the W-M widelane (L6) and the extra-widelane (L4).

The resolution of the cycle slips is done in two steps: detection and fixing. In our algorithm, the cycle slip detection uses the following strategy: We examine the ambiguity N6 of widelane L6 and ambiguity N4 of extra-widelane L4. The widelane ambiguity N6 is ionosphere free and suffers only from system measurement noise and multipath variations (E.q. 3.3.6). Also the ionospheric effects are largely reduced in L4. Such errors should be smooth over several epochs compared to a cycle break. When a discontinuity occurs in the widelane, there is a possible cycle break there. Then a cycle slip is detected.

Unfortunately, when a cycle slip is detected by the widelane, it is impossible to clarify if this break is in L1 or L2 due to the nature of the widelane (L1-L2). Also the widelane method can not solve the 1/1 slip situation (i. e., one slip in each L1 and L2 will not show discontinuous jump in L6 and is reduced largely in L4). In these situations, we check the postfit-residuals of phase solutions for each satellite to detect any possible missing cycle slip. In the data processing, when a cycle slip is detected, our software will reset the satellite as a new satellite and the strategy described in the last section to regain its ambiguities in two frequencies. If more than two satellites have the cycle slip within the same period, it is possible that a receiver lost signal lock and reset itself. In this situation, an ambiguity search starts for re-initialization.

We evaluated our ambiguity algorithm with some tests. Two Leica receivers were used in a kinematic survey around MIT campus on May 28, 1998. One receiver moved within 10 meters from another in an area among buildings which may cause signal loss. Also one of the antennas was intentionally turned over during the test. These actions caused a lot of cycle slips and signal loss in observations in a short time (Figure 3.16). Our software dealt with the data well, detected and fixed all of the cycle slips and successfully detected the signal reset and re-gained the new ambiguities automatically. The residuals of one satellite, PRN10 (which has the largest number of cycle slips), have an averaged RMS scatter of 0.9 cm and are very flat before and after the signal break (Figure 3.16).

We developed a method targeted to correct phase ambiguity problems in almost all situations for a GPS receiver moving in a large local area, such as the aircraft flying within 100 km horizontal region. The large ionospheric effects can potentially corrupt the ambiguity solution on the longer baseline. The dual frequency processing methods developed for the cycle slips and the rising of a new satellite are able to correct the ionospheric effects as long as the previous ambiguities are correctly resolved. Therefore, for most applications, when the aircraft starts within 10 km of the reference base station, we are able to maintain ambiguity resolution while the aircraft flies as far as 100 km distance away. This feature is very important for a consistent and reliable solution of trajectory determination. The initial ambiguity resolution has been tested and was successful in ambiguity solution for a baseline of 75 km. It demonstrates the potential of our method of ambiguity resolution for long baselines, but more tests are needed in a strong ionospheric situation, although long initial baseline is rare for most flight applications such as the Long Valley experiments.

3.6 Software Design

In the software design complementing the ambiguity search with Kalman filter processing, we use an event diagram shown in Figure 3.17 to demonstrate the time processing flow. The

event diagram in Figure 3.17 shows the main event flows in the software. Each event frame may contain more sub-events which are not shown here. The data involved into the processing can be divided into time-dependent and time-independent ones. In the GPS kinematic survey, the observation data is dense and recorded in time order. To save computer memory and space, we read in and process these time-dependent observation data and model values such as atmospheric delays epoch by epoch within a loop. Thus the event flow of the processing is designed into 3 parts: a pre-processor and a post-processor for the time-independent data such as the antenna offset, position of the reference stations, and the main part, a loop to deal with the observations and model values in each epoch. The details of process are shown in the following diagram.

References

Abidin H. Z., On the construction of the ambiguity searching space for on-the-fly ambiguity resolution. *Navigation, 40*, 3, 321-338, 1993.

Abidin H. Z., Wells D.E. and Kleusberg A., Some aspects of "on the fly" ambiguity resolution. In: *Proceeding of the Sixth International Geodetic Symposium on Satellite Positioning, Columbus, Ohio, March 17-20. Vol. 2*, 660-669, 1992.

Bender P. L. and Larden D. R., GPS carrier phase ambiguity resolution over long baselines. In *Proceedings of the First International Symp. on Precise Positioning with GPS, Rockville, MD, Vol. 1*, 357-361, 1985

Blewitt G., Carrier phase ambiguity resolution for the Global positioning System applied to geodetic baselines up to 2000 km, *J. Geophy. Res., 94*, 10,187,-10,203, 1987.

Borge, T., and B. Forssell, A new real-time ambiguity resolution strategy based on polynomial identification. *Proceedings of the International Symp. on Kinematic Systems in Geodesy, Geomatics and navigation, Banff, Canada,* August 1994.

Finn A, Matthenwman J., A single frequency ionospheric refraction correction algorithm for TRANSIT and GPS, *Proceeding of the Fifth international geodetic Symposium on satellite position, Las Cruces, New Mexico*, **2**, 737-756, 1989.

Frei, E., and G. Beulter, Rapid static positioning based on the fast ambiguity resolution application FARA. Theory and first results. *Manuscripta Geodaetica, 15,* 325-356, 1990.

Hofmann-Wellenhof, B., H. Lichtenegger, and J. Collins, Global Positioning System: Theory and Practice, *3rd Ed., Springer-Verlag Wien New York,* 1995.

Goad C. C., Goodman L., A modified Hopfield tropospheric refraction correction model. Paper *presented at the American Geophysical Union Annual Fall Meeting at San Francisco, California,* December 12-17,1974.

Hatch R., Dynamic differential GPS at the centimeter level, *Proceeding of the Fourth International Geodetic Symposium on Satellite positioning, Austin, Texas,* **2**, 1289-1298, 1986.

Hatch R., Instantaneous ambiguity resolution. In: Schwarz KP, Lachapelle G, *Eds, Kinematic systems in geodesy, surveying, and remote sensing. Springer, New York, Berlin, Heidelberg, London, Paris, Tokyo, Hong Kong,* 299-308,1990.

Hatch R., Ambiguity resolution while moving- experimental results. In: *Proceedings of ION GPS-91, Fourth International Technical Meeting of the Satellite Division of the Institute of Navigation, Albuquerque, New Mexico, September 11-13*, 707-713, 1991.

Hwang P.Y. C., Kinematic GPS: resolving integer ambiguities on the fly. In: *Proceedings of the IEEE Position Location and Navigation Symposium, Las Vegas, March 20-23,* 579-586, 1990.

Lachapelle G., Hagglund J., Falkenberg W., Bellemare P., Casey M., Eaton M., GPS land kinematic positioning experiments. In: *Proceedings of the Fourth International Geodetic Symposium on Satellite Positioning, Austin, Texas, April 28- May 2, vol. 2,* 1327-1344,1986.

Lachapelle G., Cannon M. E. and G. Lu, ambiguity resolutions on-the-fly - a comparison of P-code and high performance C/A code receiver technologies. *Proceedings of ION GPS-92, The Institute of Navigation, Alexandria, VA,* 10235-1032, 1992.

Landau H. and Euler H.-J., On-the-fly ambiguity resolution for precise differential positioning. In: *Proceedings of ION GPS-92, Fifth International Technical Meeting of the Satellite Division of the Institute of Navigation, Albuquerque, New Mexico, September 16-18,* 607-613, 1992.

Loomis P., a kinematic GPS double-differencing algorithm. In: *Proceedings of ION GPS-92, Fifth International Geodetic Symp. on Satellite Positioning, Las Cruces, New Mexico, March 13-17, Vol.2,* 611-620, 1989.

Lu, G., M.E. Cannon and G. Lachapelle, Improving the reliability of OTF ambiguity resolution with dual frequency GPS Observations., *ION-GPS 95*, 1111-1116, 1995.

Mader G. L., Ambiguity function techniques for GPS phase initialization and kinematic solutions. In: *Proceedings of the Second International Symposium on Precise Positioning with the Global Positioning System. Ottawa, Canada, September 3-7,* 1233-1247, 1990.

Mader G. L., Rapid static and kinematic Global Positioning System solution using the ambiguity function technique, *J. Geophys. Res., 97*, 3271-3283, 1992.

Melbourne W. G., The case for ranging in GPS-based geodetic system. In *Proceedings of the First International Symp. on Precise Positioning with the GPS, Rockville, MA, April 15-19, Vol. 1,* 373-386, 1985.

Remondi B. W., Pseudo- kinematic GPS results using the ambiguity function method. *National*

Information Center, Rockville, Maryland, NOAA Technical Memorandum NOS NGS-52, 1990a.

Remondi B. W., Recent advances in pseudo-kinematic GPS. In: *Proceedings of the Second International Symposium on Precise Positioning with the Global Positioning System, Ottawa, Canada, September 3-7,* 1114-1137, 1990b.

Remondi B. W., Real-time centimeter-accuracy GPS without static initialization. In: *Proceedings of Sixth International geodetic Symp. on satellite Positioning, Columbus, Ohio, March 17-20,*1992.

Teunissen, P. J. G., The invertible GPS ambiguity transformation. *Mauscript geodaetica, Vol. 19, No. 6,* 1994.

Teunissen, P. J. G., The invertible GPS ambiguity, *Manuscripta Geodaetica,* **20, No. 6,** 489-97, 1995

Wei, M. and K. P. Schwarz, Fast ambiguity resolution using an integer nonlinear programming method, *ION-GPS 95,* 1101-1110,1995.

Wild U., Beutler G., Gurtner W. and Rothacher M, Estimating the ionosphere using one or more dual frequency GPS receivers. In: *Proceedings of the Fifth International Geodetic Symposium on Satellite Positioning, Las Cruces, New Mexico, March 13-17, Vol. 2,* 724-736, 1989.

Wubbena, G., The GPS adjustment software package GEONAP, concepts and models. In: *Proceedings of the Fifth International Geodetic Symposium on Satellite Positioning, Las Cruces, New Mexico, March 13-17, Vol. 1,* 452-461, 1989.

Yong, M., C. Goad and B. Schaffrin, Real-time on-the-fly ambiguity resolution over short baselines in the presence of Anti-Spoofing. *Proceedings of ION GPS-94 Seventh International meetings, Salt lake City, Sept.,* 1994.

Figure Captions

Figure 3.1 Behavior of the height estimates determined from P1 code measurements compared to determinations from phase measurements during the static stage in the beginning of the aircraft survey on Sept. 13, 1993 in Long Valley. The lighter line (straight) represents the phase solution after a correct ambiguity adjustment. The darker line represents the results from P1 code measurements. Position process noise is set to 10 m $s^{-1/2}$.

Figure 3.2 Behavior of the geometry-free W-M widelane (L6) observations and the extra-widelane (L4) observations. The experiment was conducted in Long Valley with the airborne kinematic measurements on Sept. 13, 1993. Here we show L4 and L6 of two satellites, PRN13 and PRN07. Their mean values can be found in Table 3.1. The widelane observations tend to be noisier when the elevation goes lower because they use code observations, which are more sensitive to atmospheric and multipath effects.

Figure 3.3 The rank of the top ambiguity candidate (best) in each individual epoch. The epochs are separated by 10 seconds. The left and darker bins are the ranks with residual sum of all primary satellites taking part in the search. The right and lighter bins are the ranks with Mader's cosine function sum of all satellites which includes the low elevation angle observations which are the non-primary satellites.

Figure 3.4 Behavior of three top ambiguity candidates in the search with the residual sum of all primary satellites. For the pair aircraft-Bishop Base receivers, the baseline is short (less than 1000 m). The experiment date was Sept. 13, 1993. The star marks are values of the top candidate, the pluses for the second top candidate, and the circles for the third candidate. The upper plot shows the RMS of the phase residuals at each epoch during the ambiguity search. The bottom left plot shows the mean RMS scatter accumulated from the past epochs and the bottom right plot show the averaged point-to-point variation of RMS accumulated from past epochs for three ambiguity candidates. All candidates went through the L1/L2 lane constraint and the rank processing, so not every candidate ranks in the top 50

for every epoch because it may fail to pass some criterion of constraints (see details in the chapter). A "true" ambiguity set usually results into a lowest mean RMS sum and a lowest variation rate of RMS of observations.

Figure 3.5 Behavior of three top ambiguity candidates in the search with the Mader function using all satellites. The marks represent the ambiguity candidates in the same order as Figure 3.4. we show the Mader function at each epoch at the upper plot, the mean value and epoch-to-epoch variation accumulated from previous epochs at the bottom left plot and at bottom right plot, respectively.

Figure 3.6 Validation values calculated from different criteria with total accumulated past search epochs. The interval between epochs is 10 seconds. The values are calculated with the ratio of validation functions between the top candidate and the second top candidates. The solid line is the result from our new validation function. The dashed line uses the average residual sum only and the dot-dashed line uses the Mader function only for the ratio computation. The significance level is set to 2 for all functions.

Figure 3.7 The estimated elevation heights of the aircraft on the runway. During this 18-minute period, the aircraft was sitting on the ground (no movement). The phase observations are used for the calculation associated with the best ambiguity set and the second best ambiguity sets which we have computed from the search. Velocity processing noise is loose (in kinematic mode) with 100 m $s^{-1/2}$. The lighter line represents the results from the best ambiguity set and the darker line represents the results from the second best ambiguity set respectively. The darker line has a jump when a satellite is lost from the measurements due to its low elevation. The sigma of the darker line changes from 4 cm to 12 cm while that of lighter line just increases from 3.8 cm to 4.7 cm.

Figure 3.8 Same as Figure 3.3 except the baseline is Bishop Base to Casa Diablo (75 km) for this plot. Experiment date is Sept. 15, 1993. Because we used all available satellites in the search, the residual sum shares the same rank order as the Mader function. Due to the increasing model errors with baseline length, the overall best candidate does not rank in

the top three all the time as it does in the short baseline test.

Figure 3.9 Same as Figure 3.4 except the baseline is Bishop Base to Casa Diablo (75 km).

Figure 3.10 Same as Figure 3.5 except the baseline is Bishop Base to Casa Diablo (75 km).

Figure 3.11 Same as Figure 3.6 except the baseline is Bishop Base to Casa Diablo (75 km).

Figure 3.12 Same as Figure 3.9 except the ambiguity search at a different search time.

Figure 3.13 Same as Figure 3.10 except the ambiguity search at a different search time.

Figure 3.14 Same as Figure 3.11 except the ambiguity search is for a different search time. In this more difficult situation, the residual sum only (dashed line) does not make it over the significant threshold line of 2 even after a 20-epoch search. Our method generates more significant value and keeps the ratio over 2 all time.

Figure 3.15 Relative position components (North, East and Up) of the Bishop Base related to Casa Diablo. The initial values are calculated with the GAMIT software.

Figure 3.16 Ambiguity resolution test at MIT on May 28, 1998. Leica receivers are used. The plots represent the results from the satellite PRN10. The top two plots display the changes of widelane (L6) and extra-widelane (L4) behavior which contain many cycle slips and bad observations because of the intentionally abrupt move of the receivers. The values of L4 and L6 sometimes jump high while we only show part of jumps around or under 50 cycles. The third plot shows the corrections of ambiguity automatically after the cycle jumps are detected or a re-initialization is made. The bottom plot shows the residuals from the valid data (solid dots), and deleted bad data (open circles) after the ambiguity adjustments. The mean of residuals of PRN10 are 0.2 mm with RMS of 0.9 cm

Figure 3.17 Event diagram of software which show the process and data input/output flows.

PRN	Total epoch	"True Ambiguity" ΔN1	ΔN2	"Initial Guess " Diff. ΔN1	ΔN2	N4 Diff. Mean	RMS	N6 Diff. Mean	RMS
2	13370	28841692	-9795538	-3	-2.6	0.3	0.2	-0.5	0.5
7	18455	1802039	1710236	-1.1	-1	0.2	0.3	-0.1	0.5
12	27144	3697686	-10427588	1.9	1.9	-0.6	0.4	0.0	1.0
13	27599	8407845	829572	1.5	1.1	0.1	0.4	0.4	0.8
16	5943	12547388	15820236	2	2.1	-0.7	0.2	-0.1	1.2
20	9902	16878285	30436029	2	2.2	-0.8	0.3	-0.2	0.9
24	23290	4596485	-680794	2.3	2.2	-0.6	0.6	0.0	0.5
26	6236	-10233762	-8090884	-1.2	-1.2	0.3	0.1	0.0	1.0
27	1680	4671577	2356118	-2.4	-4.1	0.4	0.0	-1.4	0.7

Table 3.1 The comparison of ambiguities in L1 and L2 estimated from the search technique (the "true" ambiguity) and the ambiguities (initial guess) computed from the averaged ambiguities of N4, the ambiguity of the geometry-free linear phase combination observation (L4) and of N6, the widelane ambiguity of L6. All the ambiguity qauntities represent the double difference againest those of PRN09 in cycles. First column is the PRN number of the GPS satellite. The initial guess of ambiguities are differences away from the "true" values. The columns N4 and N6 are the differences of mean values averaged over their total epochs against the calculated values from "true ambiguities", respectively.

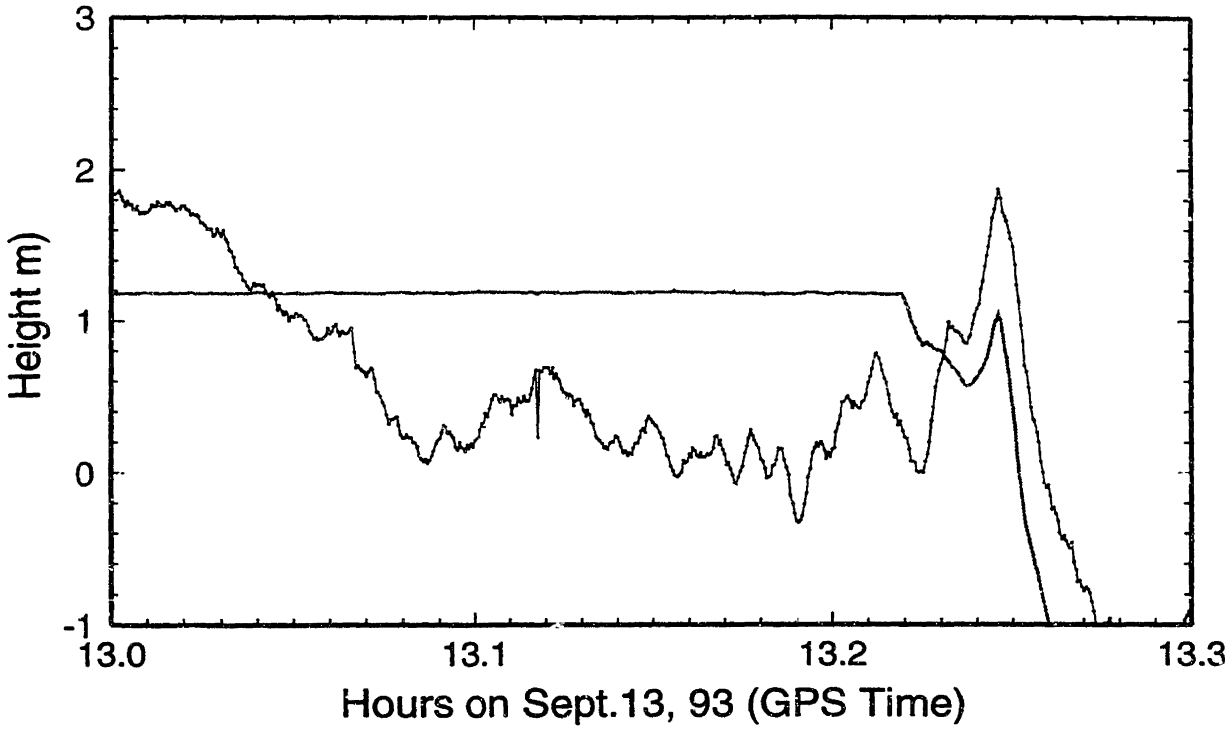

Figure 3.1

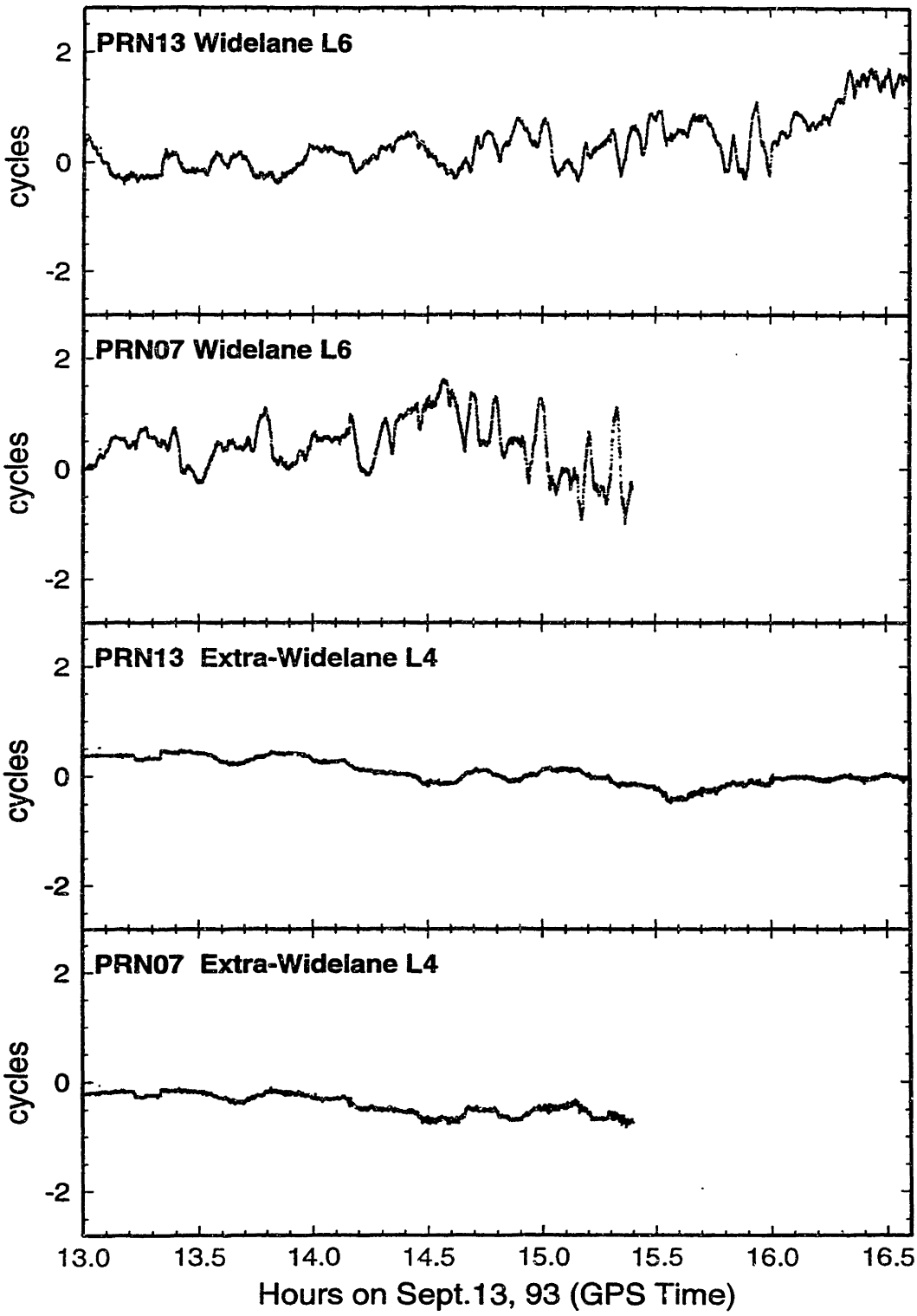
PRN13 Widelane L6
PRN07 Widelane L6
PRN13 Extra-Widelane L4
PRN07 Extra-Widelane L4
cycles
2
0
-2
13.0
13.5
14.0
14.5
15.0
15.5
16.0
16.5
Hours on Sept.13, 93 (GPS Time)

Figure 3.2

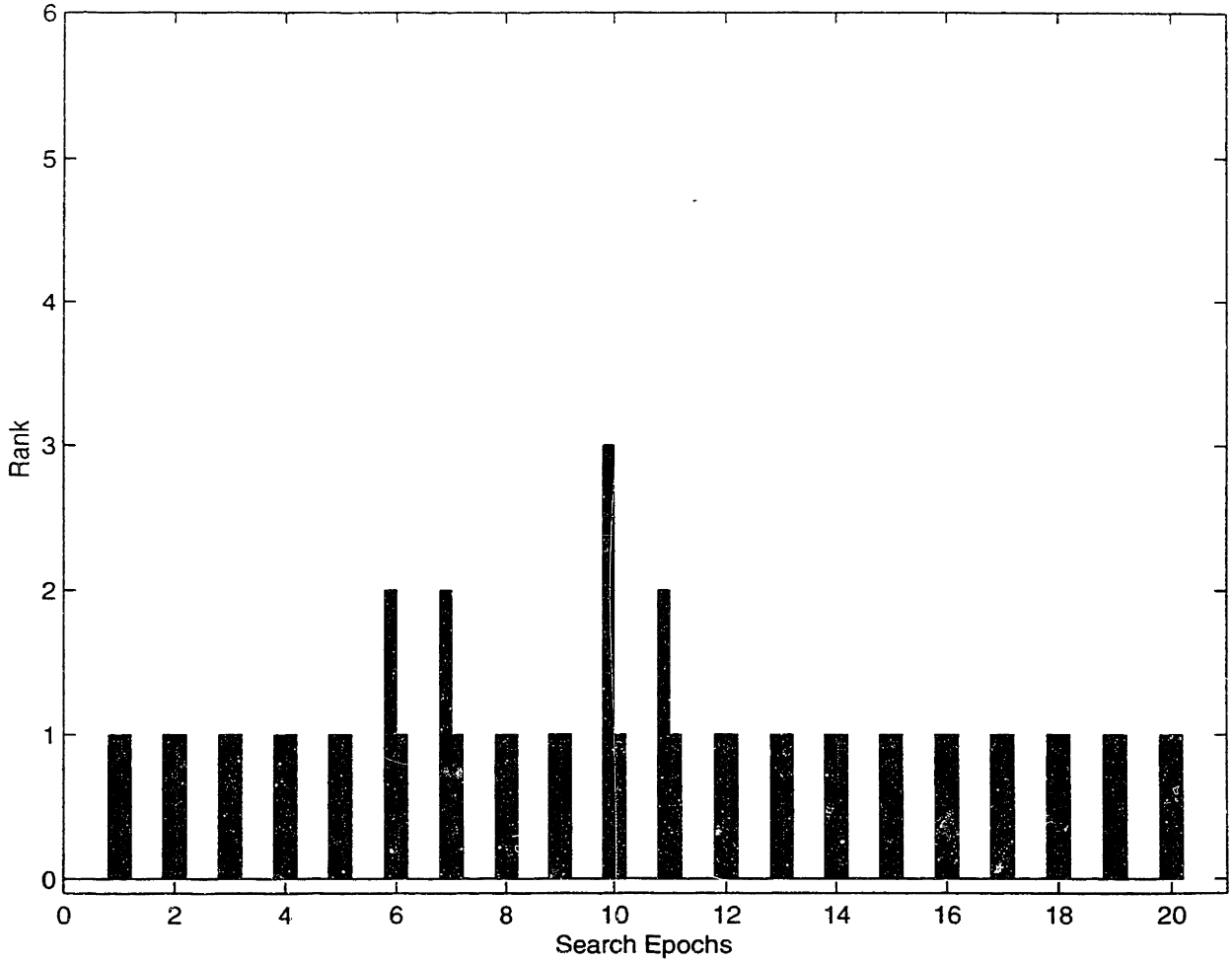

Figure 3.3

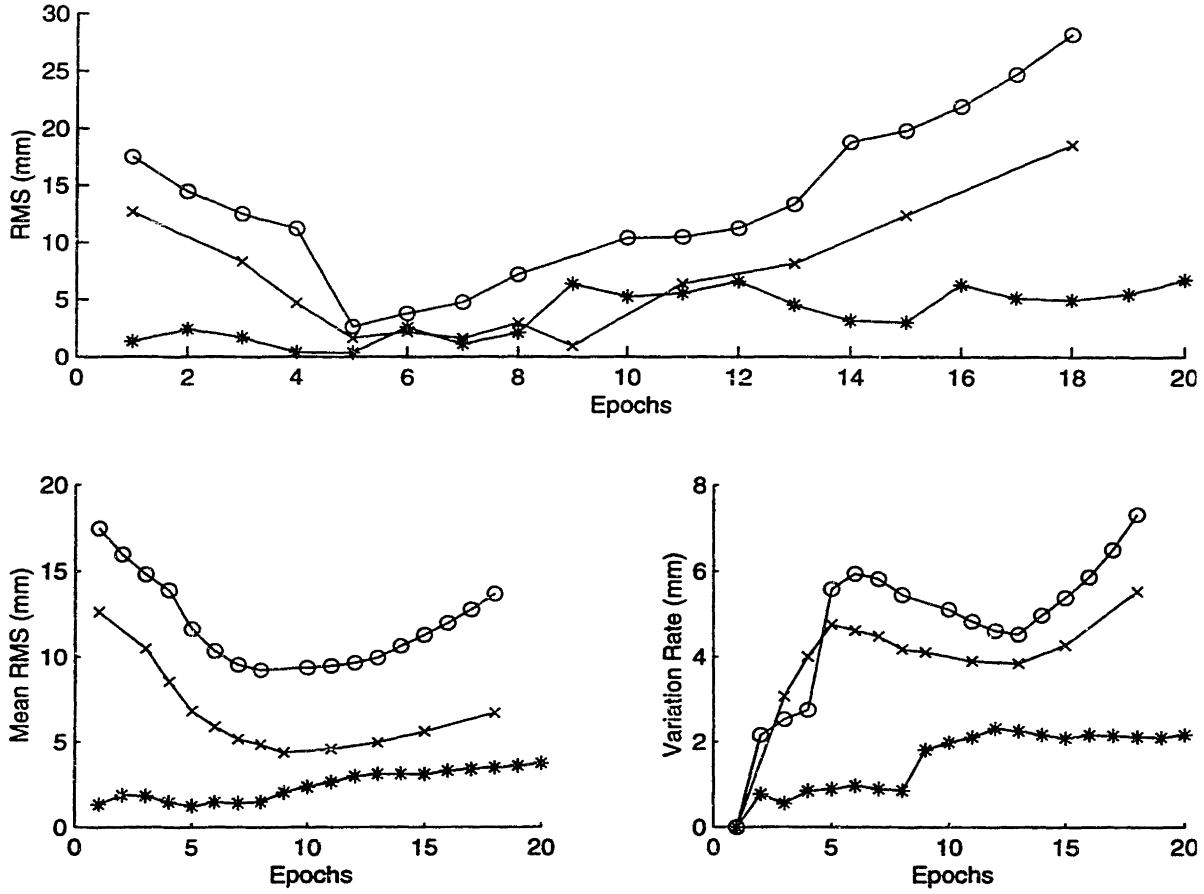

Figure 3.4

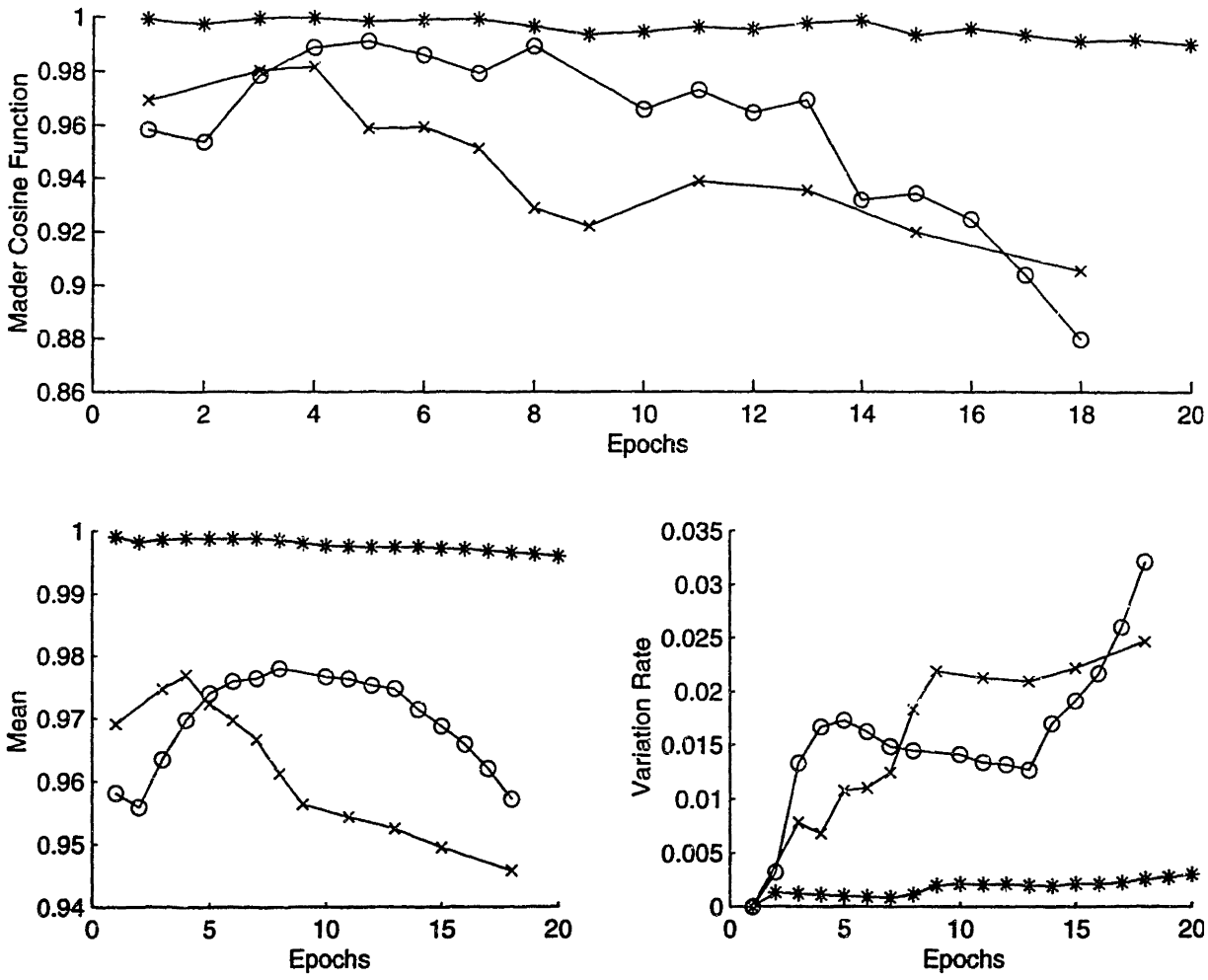
Mader Cosine Function
Epochs
Mean
Epochs
Variation Rate
Epochs

Figure 3.5

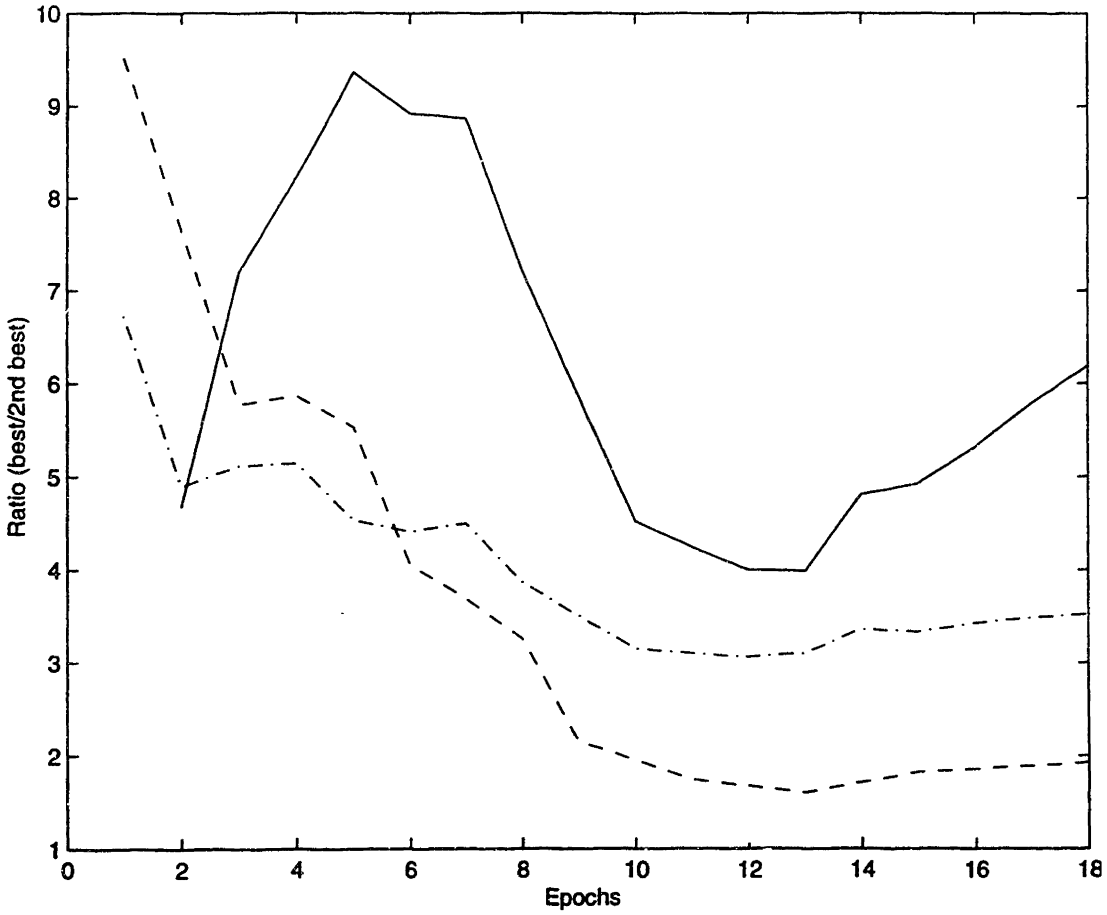

Figure 3.6

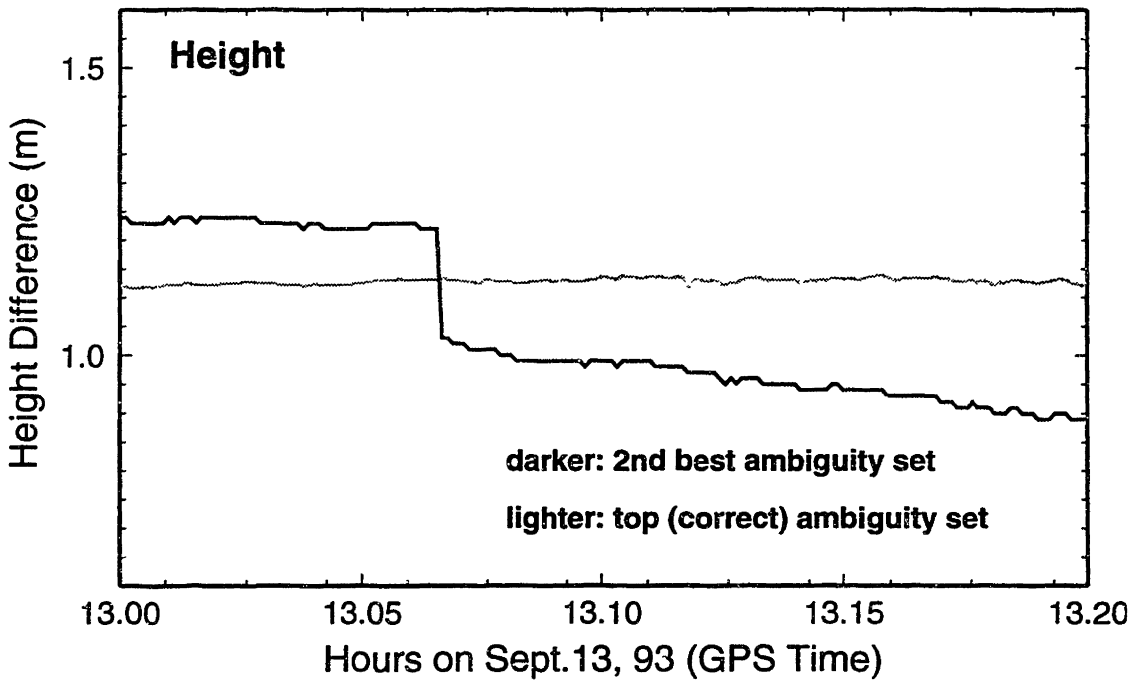
Height
1.5
1.0
Height Difference (m)
darker: 2nd best ambiguity set
lighter: top (correct) ambiguity set
13.00
13.05
13.10
13.15
13.20
Hours on Sept.13, 93 (GPS Time)

Figure 3.7

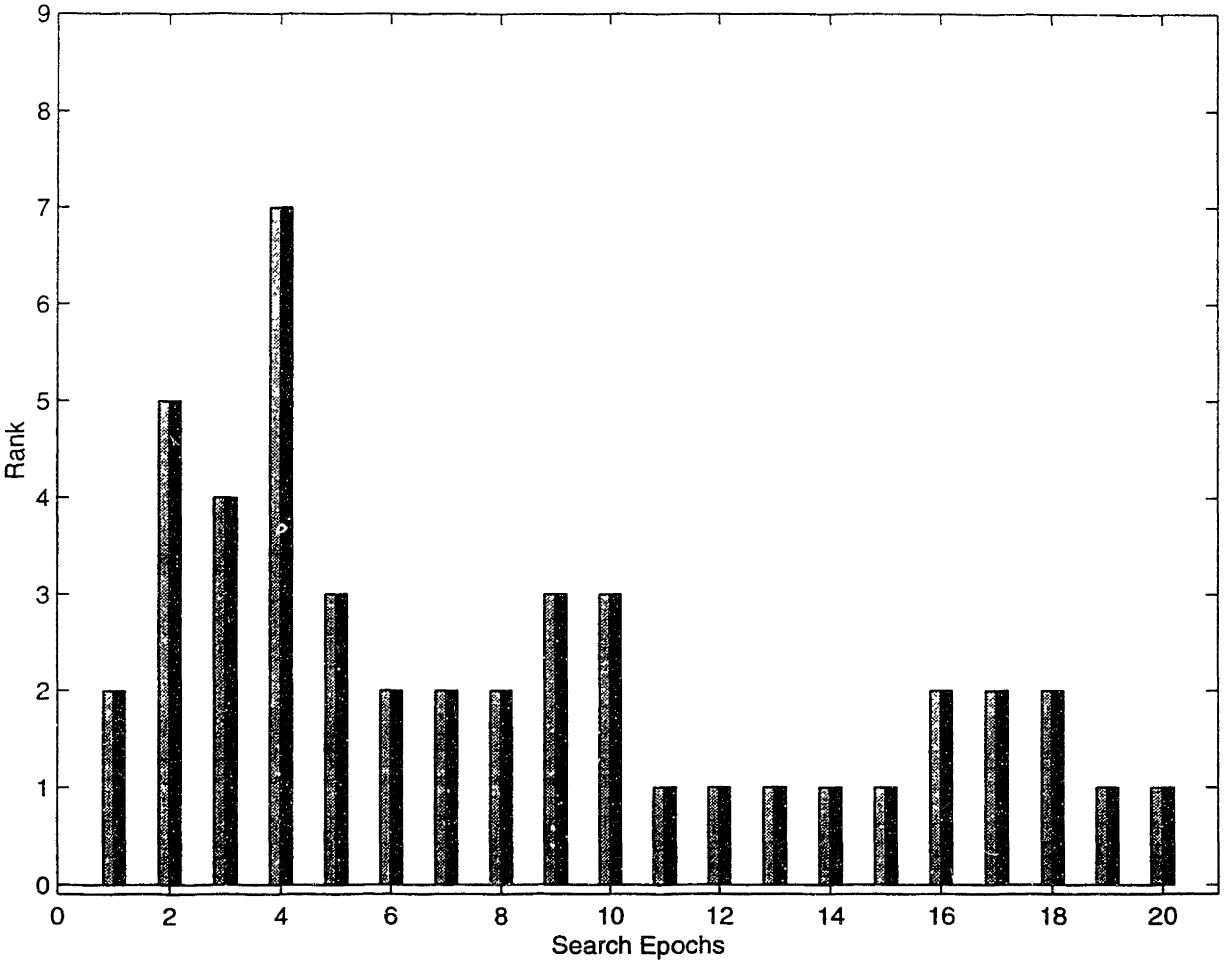

Figure 3.8

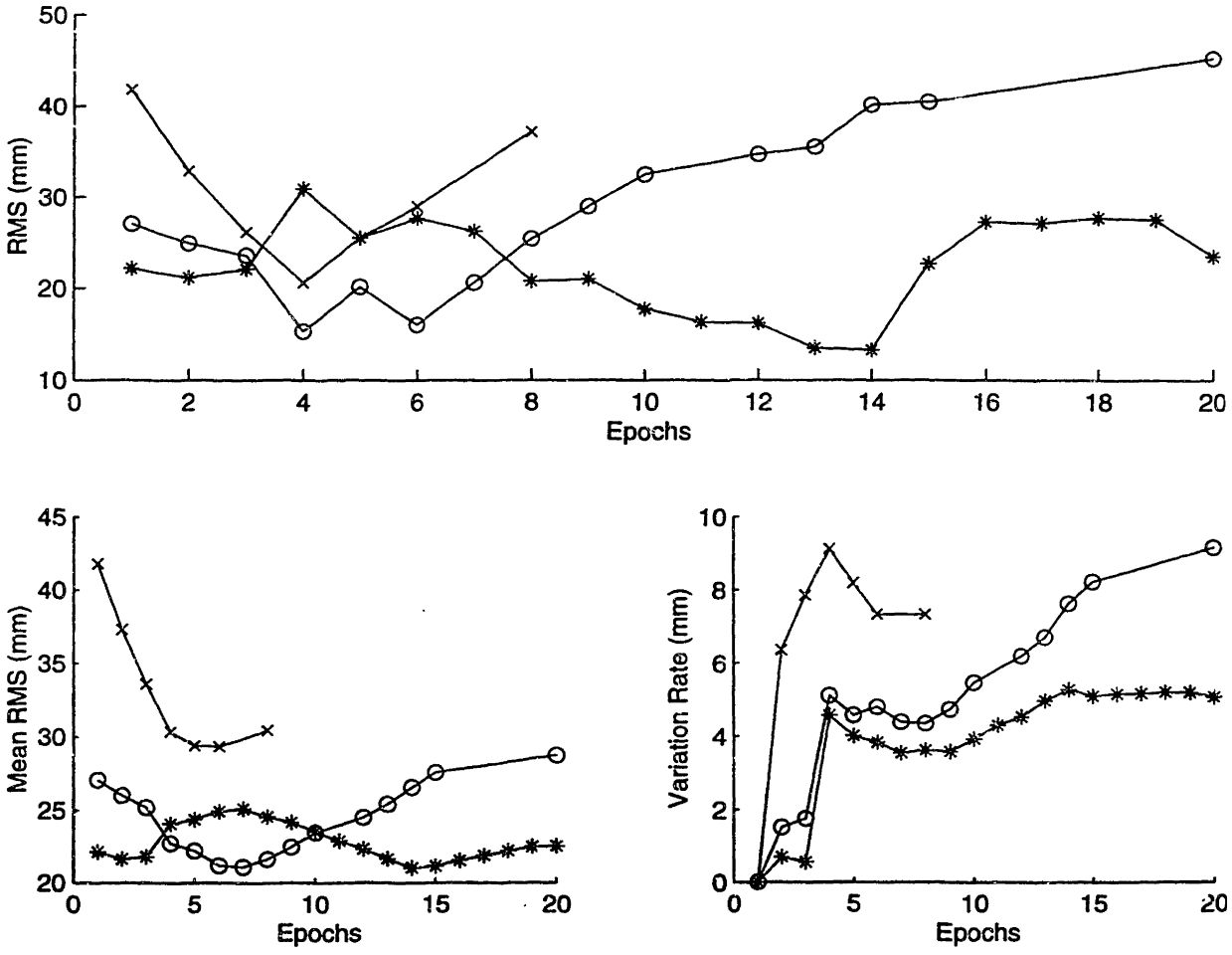

Figure 3.9

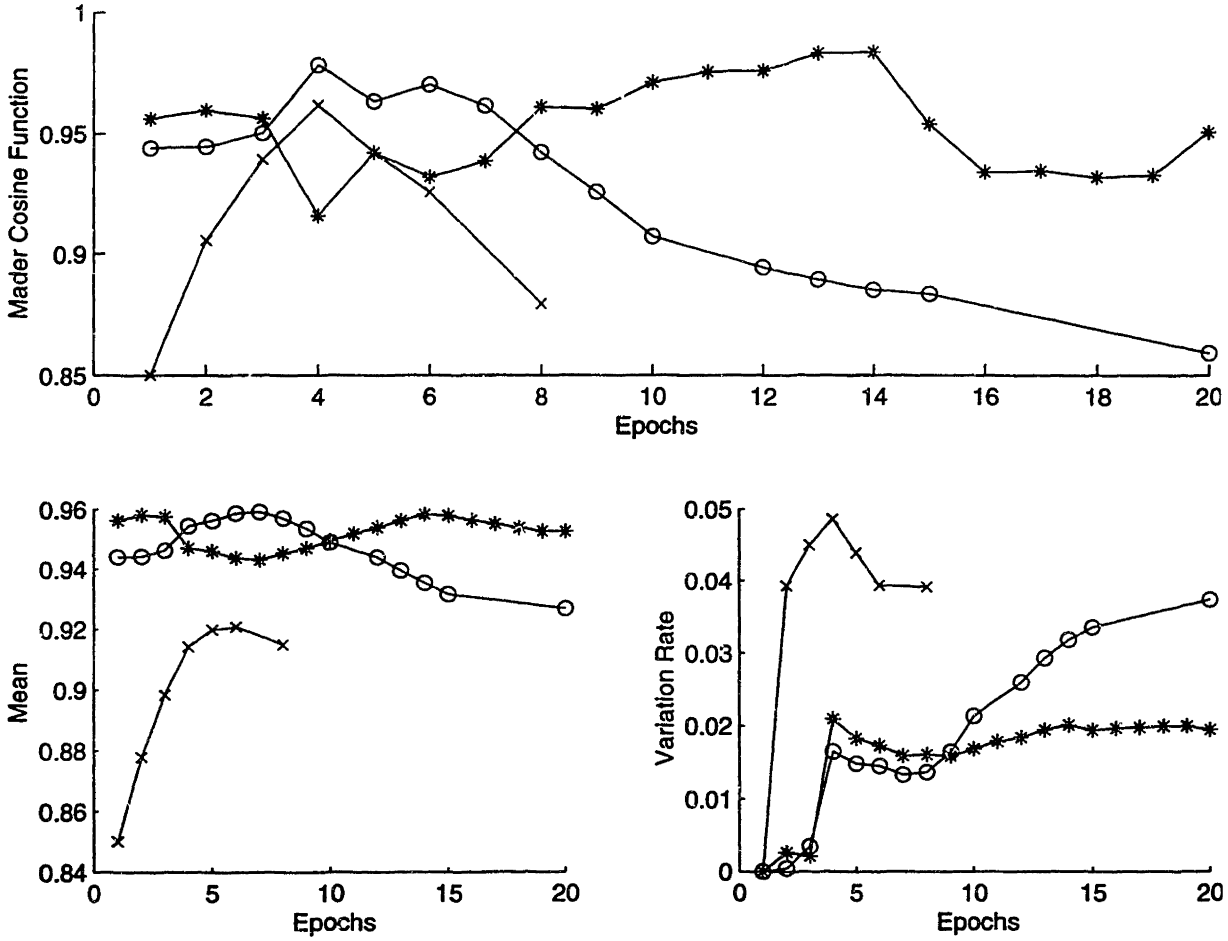
Mader Cosine Function
Epochs
Mean
Epochs
Variation Rate
Epochs

Figure 3.10

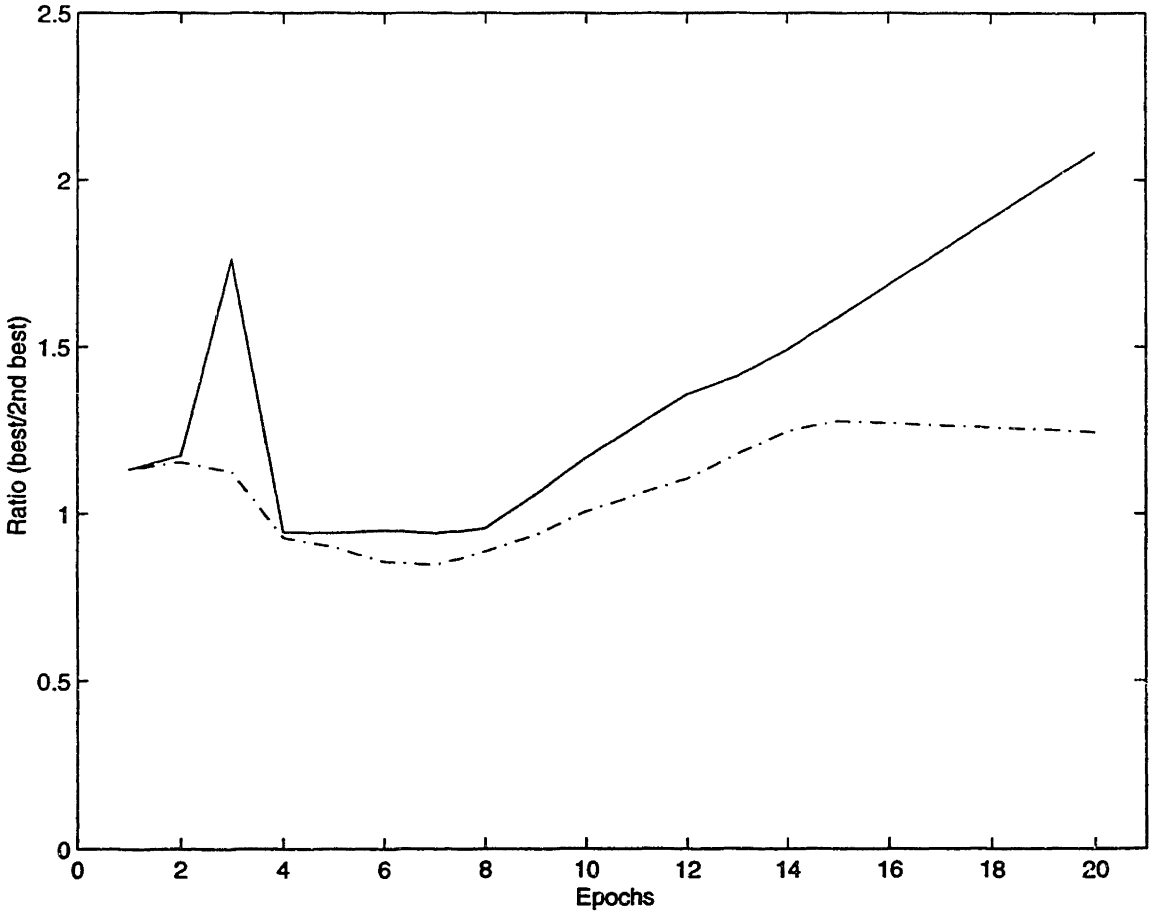

Figure 3.11

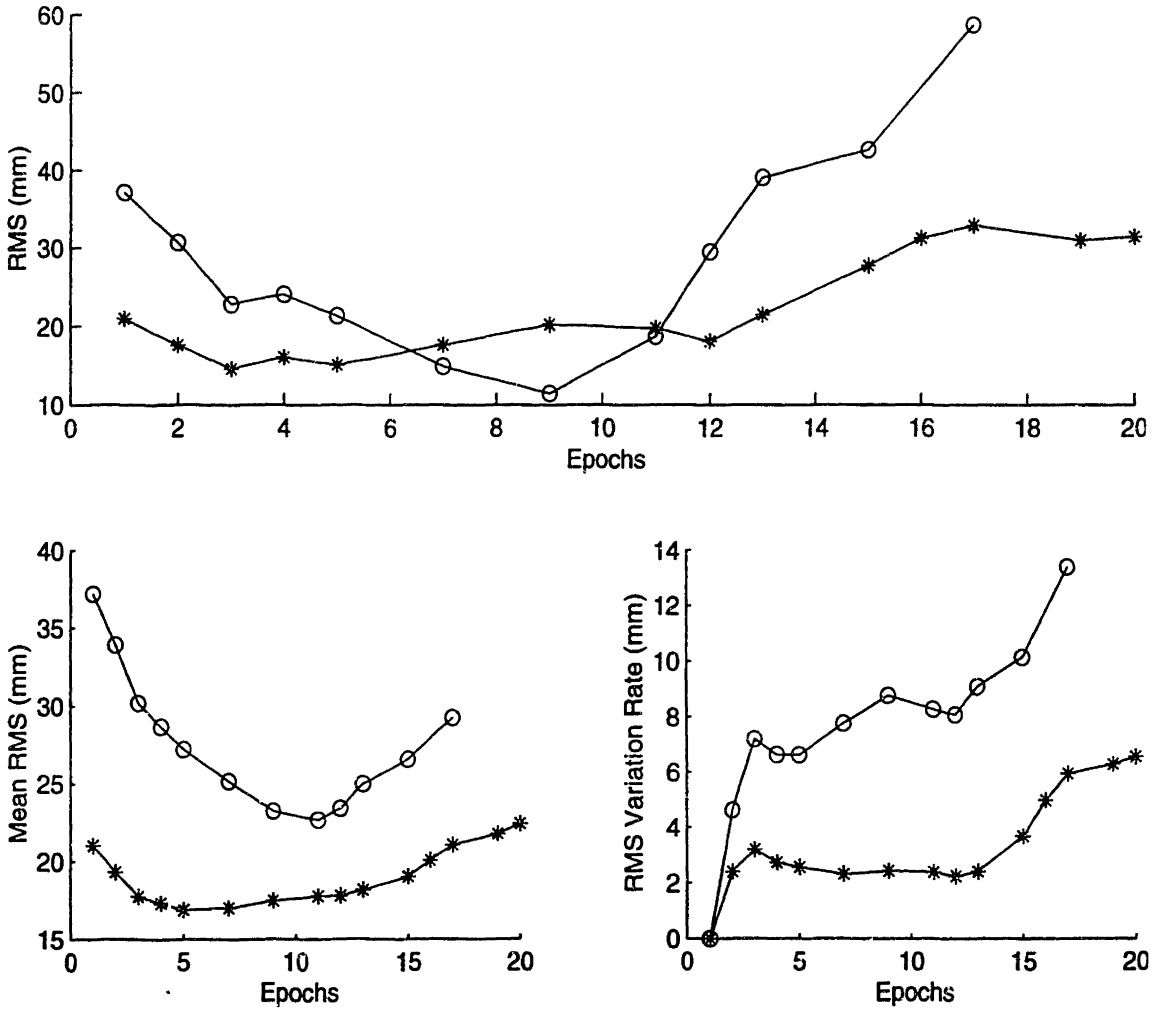
RMS (mm)
Epochs
Mean RMS (mm)
Epochs
RMS Variation Rate (mm)
Epochs

Figure 3.12

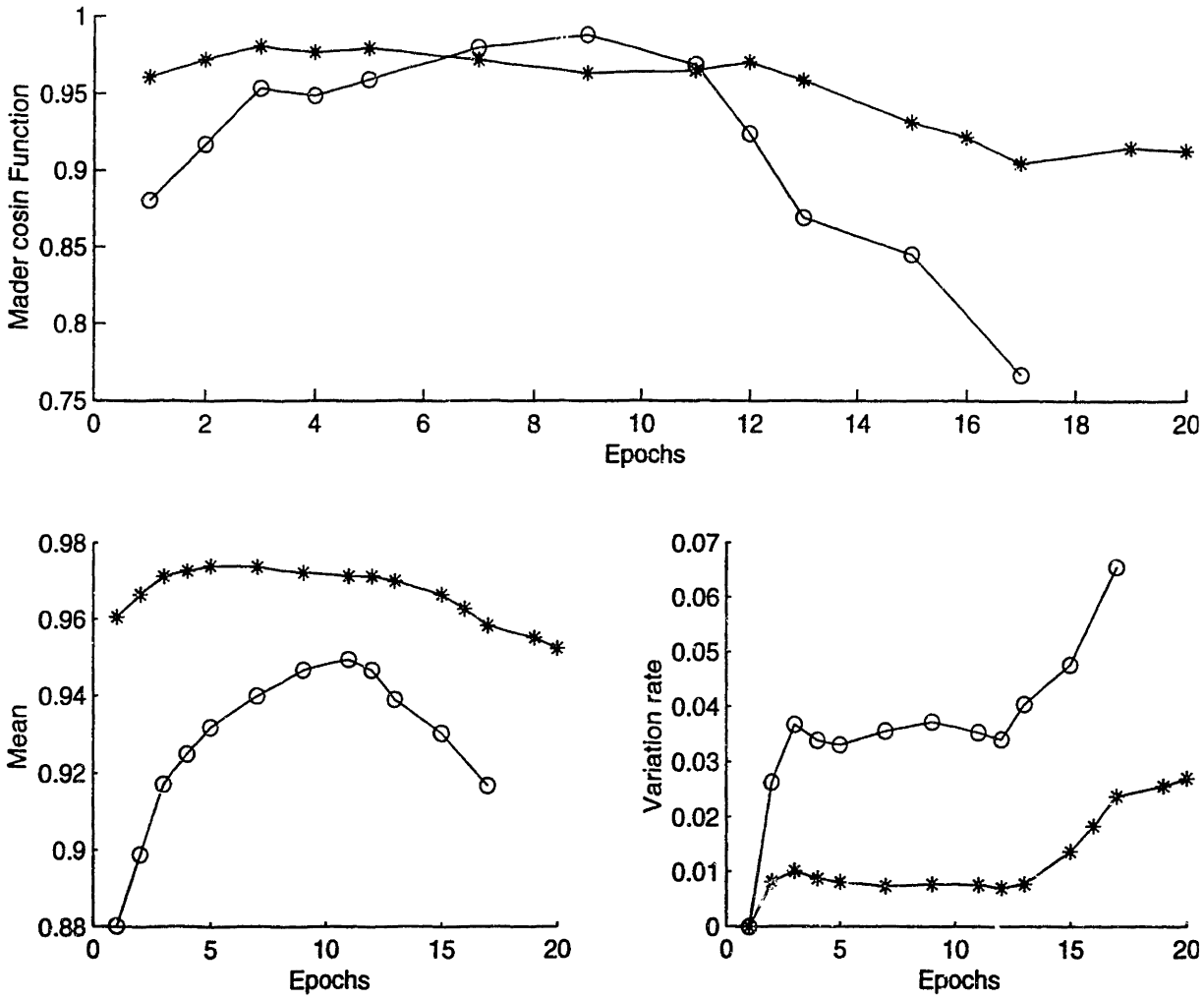
Mader cosin Function
Epochs
Mean
Epochs
Variation rate
Epochs

Figure 3.13

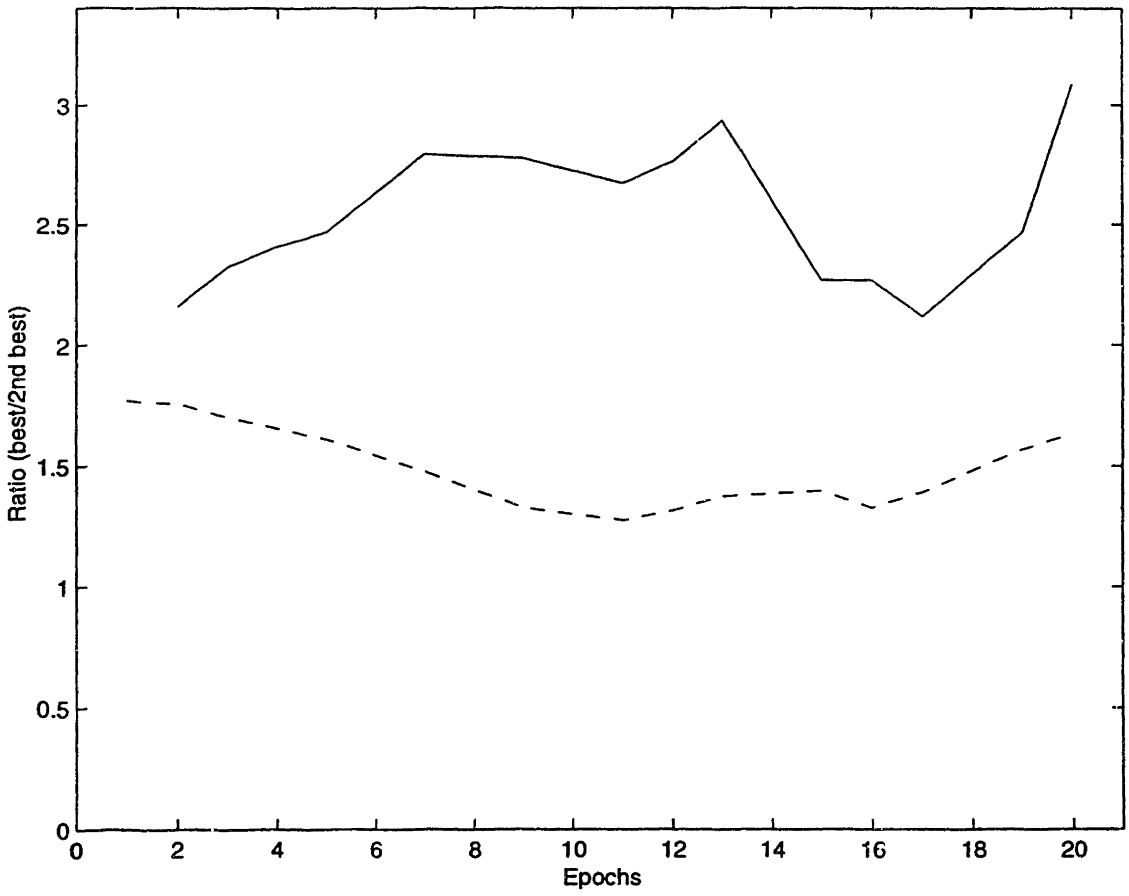

Figure 3.14

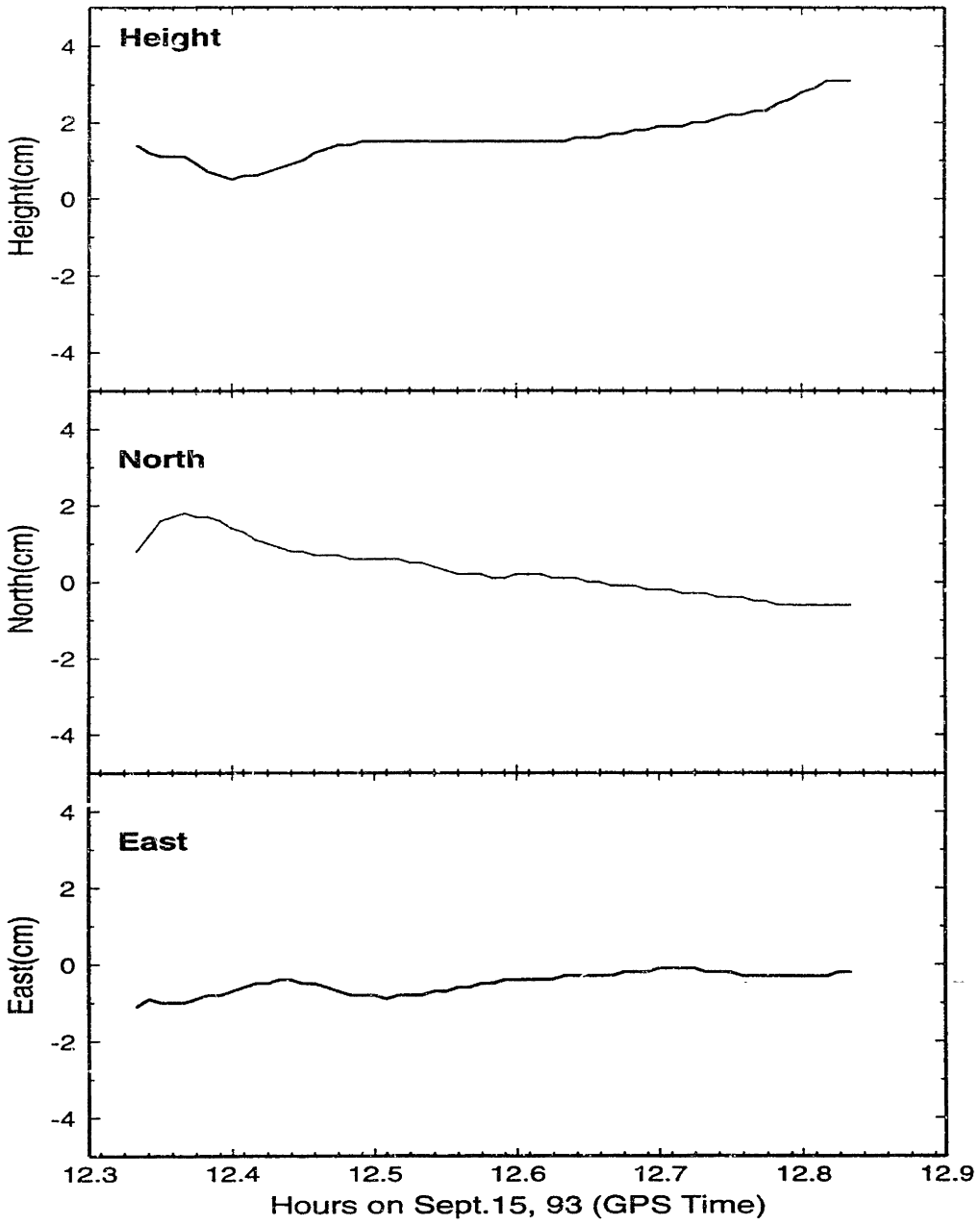
Height
Height(cm)
North
North(cm)
East
East(cm)
4
2
0
-2
-4
12.3
12.4
12.5
12.6
12.7
12.8
12.9
Hours on Sept.15, 93 (GPS Time)

Figure 3.15

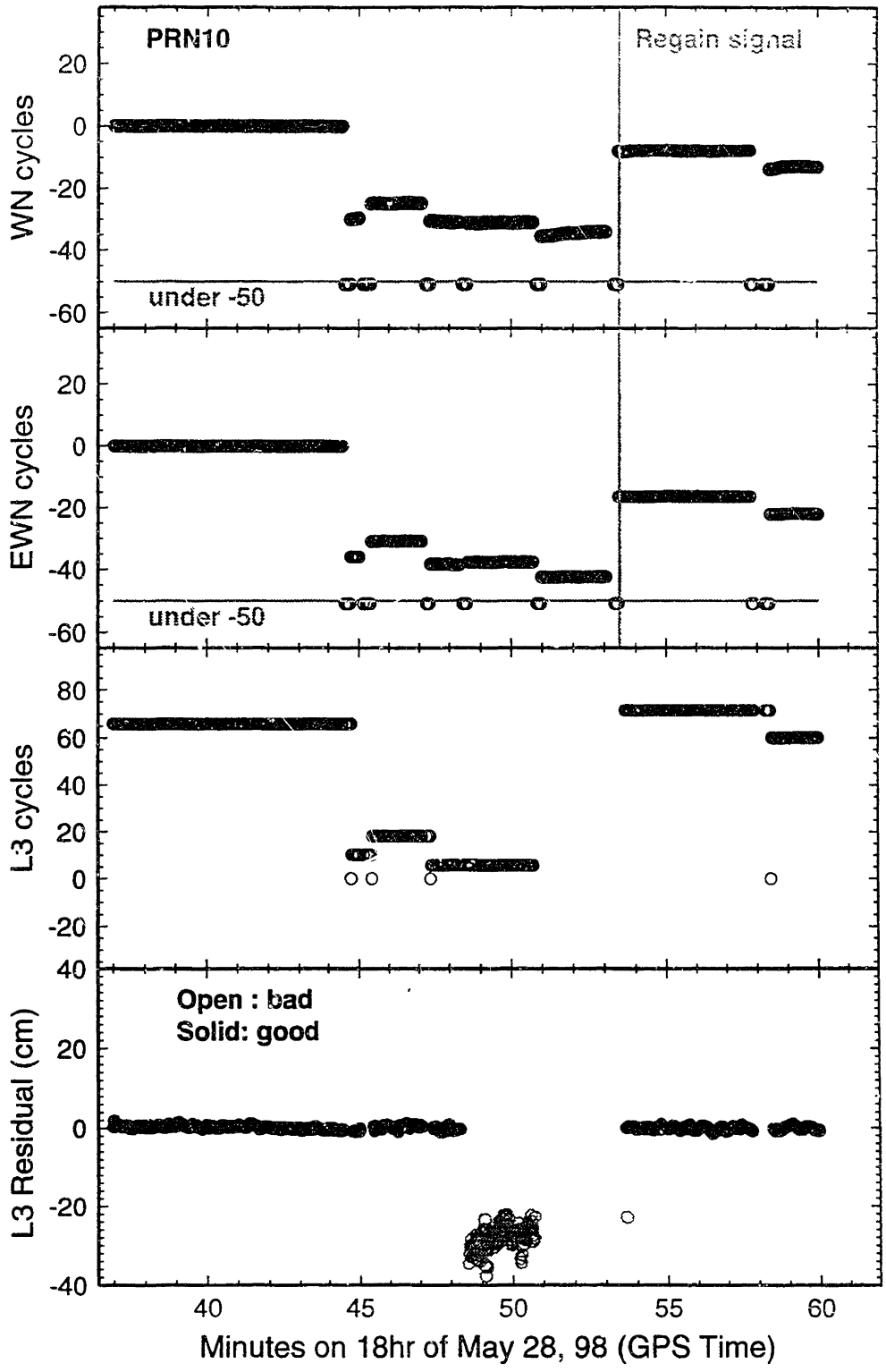
PRN10
Regain signal
WN cycles
under -50
EWN cycles
under -50
L3 cycles
L3 Residual (cm)
Open : bad
Solid: good
Minutes on 18hr of May 28, 98 (GPS Time)

Figure 3.16

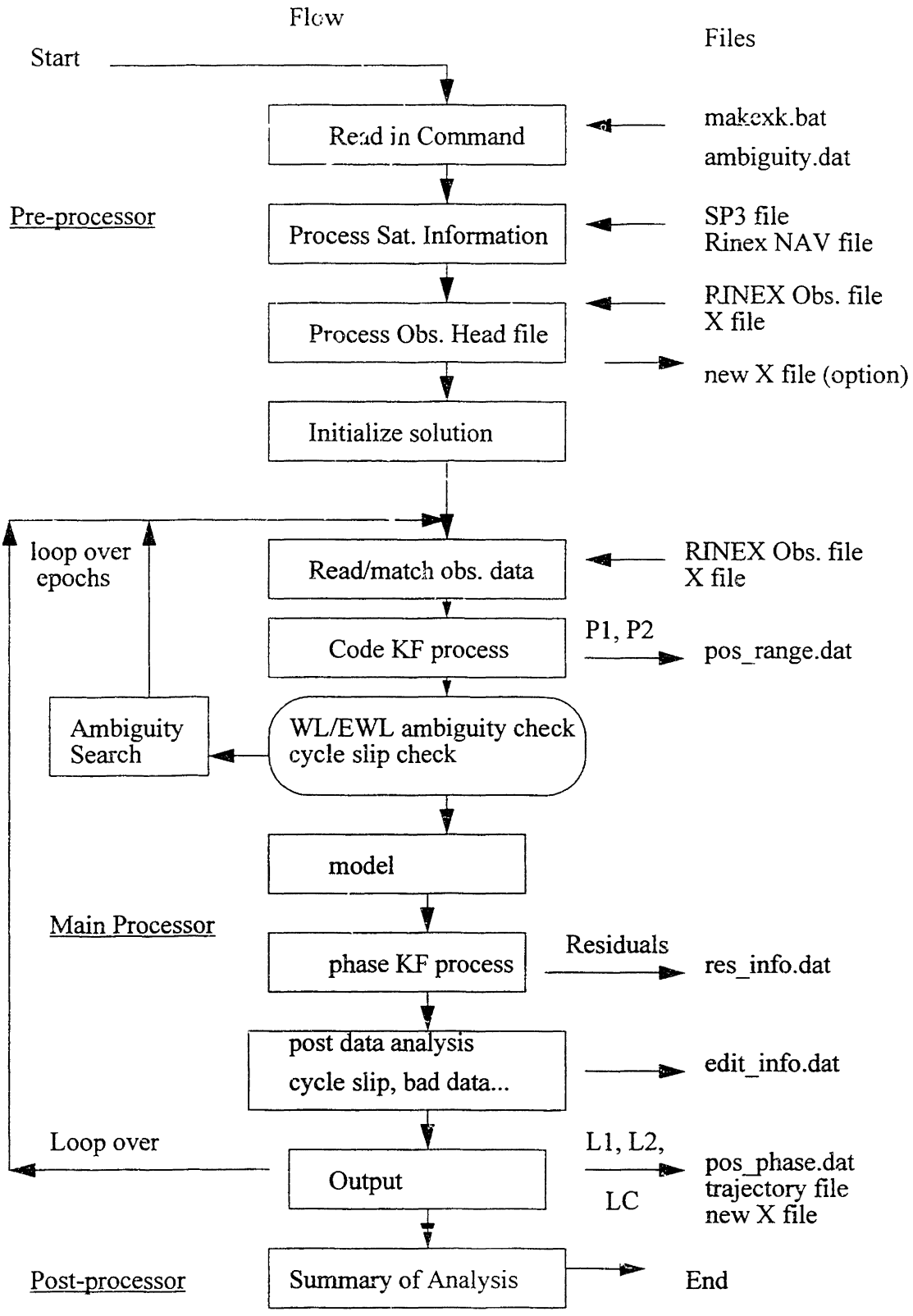

Figure 3.17 Event Diagram of software

Chapter 4 Kinematic GPS Data Analysis

In order to evaluate the performance of out differential kinematic GPS algorithm and software, TRACK, we computed the aircraft tracks with 1993 and 1995 GPS data collected in Long Valley surveys. The main aim is to verify the feasibility of GPS in accurate positioning and navigation for aircraft. The geodetic changes of ground uplift rates are not our direct concern in this thesis. In this chapter, we focus on the examination of the post-fit phase residuals of GPS observable calculated from the data analysis. We perform the kinematic tests while the aircraft is static on the ground. To further verify the reliability of the software and data analysis when the aircraft is moving, several overlapping ground tracks of the aircraft, such as these on the taxiway and runway, are also displayed and discussed.

4.1 Long Valley Surveys

Selection of flights

The first Long Valley survey was performed in September, 1993 by the SIO team and NASA T39 crew. Similar surveys were repeated between September and October, 1995, and in November, 1997. One of main purposes of these surveys was to obtain a topographic profile of the actively uplifting area and its temporal changes in the Long Valley Caldera. The other purpose was to study the accuracy of the airborne laser measurements for topographic profiling. The tracks of these flights were designed to be within 100 meters horizontally so that we can make the cross or overlapping laser footprint paths on the ground for comparison. Each survey contained a few experimental days in which the aircraft flew over the caldera twice daily. The horizontal flight zone covers an area nearly 80 km in the east-west direction and 120 km in the north-south direction. Some days the aircraft flew a even larger zone. For calibration purposes, several flat spots on the ground were targeted for repeated overflights: Antelope Springs, Benton Crossing and Lake Crowley. Antelope Springs and Benton Crossing are both treeless and flat ground surfaces within the caldera. Antelope Springs is close to the area where maximum uplift is expected.

Benton Crossing is near the edge of the caldera, somewhat far away from the center of uplift. Outside the caldera, Lake Crowley provides a good flat reflective surface to calibrate the airborne measurements. Daily height changes of water surface on the lake are expected. Direct measurements of lake heights from gauge tide stations on Lake Crowley dam are available and can be used to remove these daily height changes on the lake so that we can compare the laser measurements of lake heights from different days.

The airborne surveys during these three experiments were carried out by the same aircraft, NASA T39 jet. The T-39 jet carries a real-time pseudorange GPS receiver for high precision on-board navigation. The flight tracks of the aircraft were pre-designed for repeat flight and the real-time navigation system enables the aircraft to repeat the flights within 100 meters. The GPS antennas are mounted on the top of the plane. Two dual frequency P-code GPS receivers (a Trimble 4000 SSE and an Ashtech Z12) were used on board for the 1993 survey [*Ridgway et al.*, 1997]. In 1995, only Ashtech Z12 receivers were used. The GPS data collected from these on-board receivers are used for post-survey processing. Normally, two receivers of the same types are also used on the ground base station, set on a permanent land benchmark within a few hundred meters of the Bishop airstrip where the T-39 jet takes off and lands. (Figure 4.1).

The laser equipment and GPS receivers placed several requirements upon the geometric design for the flight tracks. Steep banks of the aircraft will cause the on-board GPS receiver to lose lock on the signal from the lower elevation angle GPS satellites. The loss of satellite signal could degrade the trajectory accuracy, introduce cycle slips and, possibly, large time gaps in time series of GPS data. Therefore, the pilot of the T-39 was advised not to bank more than 10 degrees and not to make horizontal turns with a radius less than 8.3 kilometers. The tracks are designed as several segments of short and straight lines over the points of interest connected by large radius turns. The speed of the aircraft is also limited to about 100 meters per second to allow the laser system to generate a 1 meter radius footprint with 2 meter sampling rate (50 hz laser sampling) along track. The flight heights of the aircraft are also pre-designed for best results in both 1993 and 1995 surveys. The 1993 survey used an ATLAS laser system which requires the altitude of aircraft not to be higher than 1000 meters above the ground to generate the 1 meter radius footprint on the ground. Thus in the 1993 survey, the flight heights above topographic ground are nor-

mally around 500 meters. The height of aircraft on the flight varied by a few thousand meters responding to the changes of ground topography in the mountainous area. In the 1995 survey, the T39 aircraft used a new laser system SLICER. SLICER is a medium altitude system which allows the aircraft to fly higher, at 5000-10,000 meters above geoid, so that the flights of the aircraft were flat even in the mountainous areas of the Long Valley region. In contrast to the pin-point profiling of the ATLAS system, SLICER generates a 100 meter wide swath comprising sixty 1-meter footprints.

The Base Ground Station

The location of the GPS base station at Bishop is shown in Figure 4.1. It is about 500 meters away from the Bishop Airport where the flights began and ended. The antenna is mounted on a permanent benchmark. There are two trailers within 30 meters of the antenna. Due to the short time of GPS data recording, we have not assessed the effects of multipath from the trailers. The position of the base station is calculated both from static (GAMIT) and the kinematic processing. Three GPS stations are used in the static solutions: a Bishop benchmark and two permanent GPS sites at Casa Diablo and Goldstone respectively. There may be some concerns about the absolute accuracy of the Bishop position which is based on the Casa Diablo site, which is in the center of the Long Valley dome, currently uplifting at 20 mm/yr with episodically 40 mm/yr uplift [*Dixon et al.*, 1997]. In the laser measurement discussed here, only the differential positions between the aircraft receiver and the base station are needed. Thus the position selection for the base station does not hurt the calibration accuracy of laser measurement results.

Data Collection

Our data analysis is based on only the available 1993 and 1995 data which were acquired by Ashtech receivers, one on the Bishop base station, one on the T-39 aircraft. GPS receivers record the data at a sampling rate of 2 Hz. The complete GPS data include C/A code pseudorange and carrier phase, and L2 and L2 P-code pseudorange and their carrier phases from both ground and airborne receivers.

4.2 Software Use and Data Handling

The analysis package, TRACK, developed in this thesis is documented in software manual [*Chen et al.*, 1998]. Here we give an overview of the data requirements, program input and output for the Long Valley Surveying.

Data files

Input data files

TRACK has the ability to deal with both X files (the raw data file in GAMIT) and RINEX files. The "Receiver Independent Exchange", RINEX, format is the standard GPS data transfer format. And was developed for the easy exchange of GPS data from different manufacturers [*Gurtner and Mader*, 1990]. Although the data structure of our software is based on the needs of GAMIT (MIT GPS software), TRACK can read a RINEX data observation file directly. In the analysis of the data from Long Valley, we used the RINEX files as inputs. Each file contains about 25, 000 data epochs.

To obtain positions of GPS satellites, the TRACK can either use the broadcast ephemeris given in the RINEX navigation file, or the more precise ephemerides computed from global data by a data analysis center of the International GPS Service of Geodynamics (IGS). The precise ephemeris files can be obtained from one of the IGS archives such as the NASA Crustal Dynamics Data Information System center (CDDIS). For the analysis discussed in this thesis, we used the IGS ephemerides, which had an accuracy ~ 10 ppb in 1993, and ~5 ppb in 1995 [Murata et al., 1995; Goad et al., 1997]. With these accuracies for GPS satellite orbital determination, the orbital contribution to the error is less than 1 cm in a 100 km baseline. The accuracy of the broadcast ephemerides is lower, typically 200 ppb, an error of over 2 cm for baselines of 100 km or more.

Output data file

Several different data formats are adopted for output to meet the needs of users. TRACK can generate a new X-file with updated position information. This new X-file can be processed by GAMIT other utilities for further analysis. TRACK can also provide positions as a function of time in the trajectory file format used in the laser data analysis by other GLAS groups. Other output files include phase residual files and a log file that contains information about data edited during the analysis. The residual file contains prefit- and postfit- phase residual information for each satellite at each epoch and is used for data quality checking. The log file summarizes the ambiguity resolution, cycle slip detection, and data editing carried out during the processing. This file can be used for the post analysis to provide information for data reprocessing.

Ambiguity Resolution

The process model in the Kalman filter allows us to predict the positions of the aircraft epoch by epoch from the velocity obtained from the last epoch. Using the strategy we developed in the last chapter, we deal with the ambiguity problems in all situations including the ambiguity initialization and re-initialization during the flights, ambiguity of the new satellite on-the-fly and cycle slips.

Initial ambiguity

The ambiguity search technique was addressed in Chapter 3. All the searches use frequency constraints to reduce the search number (see details in Chapter 3). In the initial ambiguity search, the L1 phase data are typically used for the geometric ambiguity search. Since the starting position of the T-39 aircraft is within 500 meter of the base station, the ionospheric delay will not affect the ambiguity search significantly. However, if the search starts with the aircraft a few kilometers of the base GPS station, the ionosphere-free observations, (L3), are used for the geometric search instead of L1. The ambiguity searches have been preformed when the aircraft is on the runway before and after the flight, and succeed in resolving ambiguities within 20 epochs for 6 flights in 1993 and 1995 surveys by using 2-5 seconds interval. A larger than recorded interval (0.5 second) is used to save the search time for a quality ambiguity search. Most of the ambiguities are fixed in the first 10 epochs. The ambiguity search in different time periods also shows

very consistent results. Due to its position-free character, our ambiguity search technique is also used to solve the ambiguities during the flights in several cases, and results show that ambiguity values are as same as those determined in the static stage of the flight.

Ambiguity for rising satellite

When a new satellite is acquired or a satellite has a cycle slip detected, its phase ambiguity bias is reset and estimated again. The initial ambiguity search strategy can work in this case. To save processing time, however, when a single cycle slip occurs or a new satellite rises, most of the time, we use a faster way (see more details in Chapter 3 to detect and fix the cycle slips and estimate the initial bias for new satellites directly. In dual frequency applications, utilizing the ionospheric delay estimates from other satellites, the ionospheric effect in the ray direction of this new satellite is estimated to reduce its impact in the ambiguity resolution.

Cycle slips and data editing

In the TRACK software, we use the ionospheric reduced geometric observations L6 and L4, a method discussed in Chapter 3, to detect possible cycle slips before processing phase data. This action is made in a pre-processing editor we designed (See the diagram in Figure 3.17).

Most cycle slips can be detected by the widelane and extrawidelane check.Due to the nature of the linear combination L1-L2 in the widelane observations, however, there are rare but possible cases undetectable by this method that the same jumps occur in L1 and L2 at the same time. Residual check is the normal tool for cycle slip detection. In the kinematic survey, the pre-fit residuals of L1 and L2 are of little use because of the movement of the receiver. The only hope to use the residuals is after estimating the positions of the receiver. The unmodeled errors remaining in residuals, such as multipath, unmodeled atmospheric effects, vary smoothly over a short observation time. These result in residual changes which vary smoothly from epoch to epoch in the absence of cycle slips. Our post-data editor relies on this behavior to detect the possible remaining cycle slips by checking the residuals and residual changes for each satellite.

Another technical problem for data checking is the similar nature of a single outlier and a cycle slip in the residuals. It is impossible to distinguish an outlier from a cycle slip instantaneously. Therefore, we develop a strategy to utilize the variation of residuals over a small time period (10 epochs) to identify whether the jump is isolated (outlier) or a permanent shift (cycle slip).

First the residuals in each observation at the current epoch are checked and sorted from maximum to minimum. If a large value occurs for one satellite data residual, a suspect is found. If this occurs when a new satellite comes at this epoch, we assume that the problem is in its uncorrected initial ambiguity guess. Otherwise, we continue to check the suspects one by one from the largest to the smallest. An abnormal jump in one satellite observation may transfer its erratic change into other observations. We begin with the one that has the maximum jump. The average values of residuals of this suspect over 5 epochs on both sides of the jump are calculated separately with their RMS scatters. If the suspect's residual value is far away from both averaged values, an isolated bad datum is found and marked. If the averaged values on both sides are not close and separated by more than three sigma of their RMS scatters, a cycle slip is possible. The next action is to find whether it is on L1 or L2. Normally, both L1 residual and widelane ambiguity (WL) are used to determine such situation.

Phase center correction

The rim of the antenna in Bishop base station is measured for each experiment. The constant height differences for both L1 and L2 phase centers from the rim are obtained from the manufacturer's manual for the same type. The antenna mounted on the roof of the T-39 aircraft is very special, and we don't have any information on it. The offset correction for the GPS receiver to the laser spot was measured for the T-39 aircraft when the aircraft was the ground. Thus the phase center offset is absorbed into this correction of the calibration.

4.3 Kinematic GPS Data Processing and Analysis

Our GPS kinematic processing begins by using pseudoranges P1 or P2 to obtain an approximate (precision of 1-2 meters) trajectory for the flight. An example of the static portion of a flight is shown in Figure 4.2. The goal of this solution is to check the quality of the data series. It also provides the mean values of widelane ambiguities (L6) and extra wide lane ambiguities (L5) and their associated RMS scatters for the cycle slip detection. Furthermore, if there are no cycle slips during the processing, these average values over the entire observation time span can also provide a quality estimation of the scale size for the ambiguity search space.

Next we perform the initial ambiguity search which is necessary for carrier phase data processing. There are five parameters controlling the search: the number of primary satellites, the allowance of noise level in the L1/L2 ambiguity integer relationship, the search range for each ambiguity, the epochs used for accumulating RMS, and the observation type for the geometric search. Generally when the aircraft is on the runway, we use a 0.1 or 0.12 cycle as the dual frequency lane constraint for these short baselines. Several larger or smaller constraint values (0.3 - 0.08 cycle) are also tested but there is not much difference in the results except the search time. We still obtain the correct ambiguities in these cases. The 0.1 or 0.12 dual frequency lane constraint is determined empirically by several tests in our experiments. For the number of the primary satellites, we normally include all satellites over 15 degree elevation angle at first, then adjust it according to the behavior of satellite with low elevations. Sometimes a cutoff of 20 degrees is applied to avoid the multipath in lower elevation angle observations. Following the examination of the behavior of its widelane and extrawidelane integers, we extend the search range by ten or fifteen integer on each side of the initial ambiguity guess for each satellite, which means that each satellite could have 21 or 31 candidates in the search space dimension. When the baseline from the aircraft to the GPS base station is short, the ionospheric effects do not play a significant role on the solution. L1 is used for the geometric analysis for the search instead of the ionosphere-free combination L3. For most experiments, when a data sampling rate of 5 or 10 seconds is used, a ten-epoch time duration of continuous search is enough for fixing and validating a significant ambiguity set. The initial ambiguity search is normally performed in the static on-runway position of flights, but this does not mean this search technique only works for the static situ-

ation. The ambiguity search technique we have implemented is position-free. Tests of the algorithm are applied when the aircraft was running on the runway and when it is flying in the air. These tests results yield the same ambiguities as those from the static determination if there are cycle slips occur during the time gaps of the different testing epochs.

After the initial ambiguity set settles down, phase observations of L1 or L3 are used for precise trajectory determination. In this stage, loose constraints are used normally 1 meter for data noise and Φ_w of $9x10^4$ m^2/s for the aircraft position process noises in three directions, together sufficient to cover the maximum aircraft velocity changes (under 300 m/s) in any situations during surveying. After analyzing the residual behavior of the data and performing some editing, we use strict constraint for the data noise (0.5 - 5 cm) and Φ_w of 10^2-10^4 m^2/s for position process noise to take the advantage of the more accurate prediction of the aircraft velocity.

Trajectories of T-39 for the 1993 experiment

Three flight surveys were performed from September 13 to 15, 1993. We display their trajectories in Figure 4.3 to Figure 4.5. In the 1993 survey, the aircraft flew at 2000 to 3000 meter above the ellipsoid to keep the aircraft 500 meter above the ground. Only the Ashtech receivers were used for the aircraft solution. L3 phase observations are used to eliminate the ionospheric effects on GPS measurements. The base station receiver had several problems during the middle of the flight on Sept. 14, and only two-thirds of the data could be used (Figure 4.4). The total flights in the 1993 survey can be divided into 18 straight line sections for laser data measurements. The trajectories are almost identical day to day to repeat ground tracks but with altitudes that may differ by a few hundred meters. In our precise kinematic mode, the precision of the positions during flights for a single epoch estimate is 2 - 4 centimeters horizontally, and around 3 - 9 cm vertically when a 5 cm L3 phase noise is used. When a 5 mm measurement noise is used, the precisions of the positions are 0.4-0.6 cm horizontally and 0.9-1.2 cm vertically. The sigma changes during the same flights are due mainly to the changes of satellite constellation (Figure 4.6).

In Figures 4.7 to 4.9, we illustrate the residual behavior during the 1993 airborne tests. The residuals from all satellites show variations under 0.1 cycles (nearly 2 cm for L3) after data cleaning, ambiguity and cycle slip fixing. In some time scans, the flat behaviors of residuals are due to the low availability of GPS satellites (down to 4). Also the same satellites show similar behaviors of residuals for the three surveying indicating systematic errors. These errors may come from the multipath from the aircraft wing because the aircraft flew the same flight tracks mostly at the same time for each day.

The adding of zenith delay estimates does not change the solution significantly. The altitude position differences are mostly under 1 cm although sometimes they are over 1.5 cm between cases with and without zenith delay estimates. One possible reason for the good aspect is that the tests were conducted under good weather with a calm atmosphere. The possible variations of atmospheric zenith delay are small and are negligible for the slight elevation angle difference of the same satellite signal obtained by two GPS receivers. We tested different atmospheric mapping functions with MTT [*Herring*, 1991], NMF [*Niell*, 1996] and CfA [*Davis*, 1986] models. The results among different mapping functions are very close. It suggests that at low altitude (less than 2 km above the ellipsoid) and for the observations above 15° elevation angles, there are no important differences among the current atmospheric mapping functions. The quality of estimation of atmospheric effect is hurt by the low satellite availability. In several time spans, the number of common observable satellites drops to only 4 (Figure 4.6), in which case we can't estimate all the parameters uniquely. In these cases, estimates are possible because the process noise constrains the atmospheric delay parameter estimate.

The phase residuals for the three days are similar (Figure 4.7 - 4.9) maybe because the schedule of flight are almost the same with the same flight time and route. The similar and non-white-noise-like behaviors of residuals indicates that the remaining errors may come from the multipathing which results from the similar ground environment when the aircraft is on the ground and from the wing of the aircraft especially when the aircraft banks in a designed flight route.

Trajectories of T-39 for the 1995 experiment

Similar flight surveys were performed from September 28 to October 10, 1995. Figures 4.10 - 4.12 show the trajectories of the Sept. 28, 29 and 30 flights. The results show behavior similar to those in the 1993 surveys. The altitudes of the aircraft in the 1995 surveys are higher (around 5 to 10 km above the ellipsoid) designed for middle range altitude measurements with the new laser instrument SLICER [*Hofton et al.*, 1997]. Also, the horizontal range of flights is much broader. The residuals from the solution of these two experiments are shown in Figures 4.13 to 4.14. On some days such as Sept. 28, the RMS scatters are little higher than those in 1993 surveys. We tested with higher elevation cutoff angle of 17^{o} and 20^{o} and the average residuals reduced 5% and 7% respectively.

4.4 Calibration Analysis on the Airport

4.4.1 Airport Static Tests

The validation of the accuracy of kinematic GPS surveying is not easy to perform because it is hard to require the aircraft to reoccupy the same spot exactly before and after the same flight and between the flights. One way to test the software is to use the data from the static stage of the aircraft positioning. Figure 4.15 shows the position of the aircraft on the ground before the Sept. 13, 1993 flight. The estimated heights are very flat and stable even when satellites rise or set during the interval. The RMS scatters of the positions then means about 2-3 cm, north, 2-3 cm, east and 3.3 cm, height assuming a 5 cm L3 phase data noise.

In Figure 4.16, we show the autocorrelation functions of the height variations when the aircraft sat on the runway. The autocorrelation functions from different surveys indicate the measurements errors in our GPS kinematic surveys are dominated by the high frequency errors in the GPS signals. The autocorrelation length is defined as the lag for which the normalized autocorrelation function to 1/e. In our surveys, the auto-correlation lengths are 73.0, 136.5, 66.5 seconds for

the experiments on Sept. 13-15, 1993, and 48.0, 77.0 seconds for those on Sept. 28 and 30, 1995, respectively. Thus data noises of the GPS signals can be averaged out in less than 80 seconds for most days; an exception is Sept. 14, 1993 for which auto-correlation length is over 2 minutes.

To test the capability of our software and algorithm in ambiguity fixing and data analysis, we processed the data independently in the kinematic mode and the quasi-static mode. In Figure 4.17, we display the positions of the aircraft on the runway at the end of the flight on Sept. 13, 1993. For the kinematic survey mode, we used a loose constraint ($4x10^4$ m^2/s of Φ_w) for positions which can cover the movements of the aircraft under a velocity of 200 m/s even it is still at the static stage. The ambiguities are calculated by the search technique when the satellite comes into the analysis during the flight. In the "quasi-static" processing, we started the ambiguity search calculation with the data after the aircraft finished the flight, but used a 0.01 m/s velocity constraint for the "quasi-static" process noise. The darker line in Figure 4.17 represents the kinematic results, and the lighter line represents the static mode survey results. The two "trajectories" agree with each other within 1 cm for most of the common observation period; the average difference is just 4 mm. This test indicates that the solutions from our software is unique and independent on the starting times as long as the ambiguities are fixed appropriately and the process noise used can cover the motions of aircraft.

4.4.2 Runway Kinematic Tests

To further test our kinematic analysis in the moving portion of the surveys, we processed several spans of data acquired when the aircraft moved on the runway at low and high speeds. There is only one runway and one taxiway at the Bishop airport. All the aircraft take off and land on the same runway, so that the measured heights of the aircraft on the runway and taxiway provide us with a qualified calibration location to compare the aircraft tracks calculated from different days. Although there may be height variations when the aircraft runs through different paths within a few tens of meters in the width of the runway and taxiway, the runway and taxiway are still relatively flat. The altitude of aircraft on the runway becomes a valuable means to assess the kinematic data quality. In this section, we compare the aircraft trajectories obtained in two experiment years (1993 and 1995).

In Figures 4.18-4.21, we show the tracks of aircraft running on the taxiway before take-off and after landing as well as its take-off and landing portion on the main runway. The tracks are calculated from the six flights during 1993 and 1995 surveys. The runway and taxiway lie mainly in northwestern to southeastern direction and are 1000-plus meters long (Figure 4.18). The taxiway links the main runway to the airport. In the data analysis, the ground heights show variations around 5 meters in runway and taxiway (Figure 4.19).

We display the detailed GPS estimated height variation on the taxiway in Figure 4.20. When the T-39 runs on the taxiway, the aircraft's speed is slow and well under 10 m/s. The maximum of differences between all reported tracks is under 8 centimeters on the taxiway. We used the differential height to eliminate the height slope changes in the horizontal direction. All tracks are recalculated relative to the track measured on Oct. 5, 1995. and results are shown in the lower plot of Figure 4.20. The analysis shows an average difference of 1.7 cm. The internal RMS scatters of each track are averaged to only 0.9 cm suggesting some systematic biases may exist. Several factors could contribute to the systematic differences, including mechanical reasons such as different tire pressures, and the ground height variations in the different running paths in the taxiway.

In Figure 4.21, we shows the detailed GPS estimated height variations when the aircraft is on the main runway during take-off. In these situations, the aircraft's speed averages 30 - 50 m/s and could be up to 60 - 70 m/s. The results demonstrate high consistency in cases of both high and low speeds. The differences of tracks measured in the six flights during 1993 and 1995 tests show that when the aircraft runs on the ground, the estimated heights of the GPS antenna are consistent within 4 cm, and under the uncertainties for single epoch measurements. The T-39 aircraft lands and takes off at different points on the runway in different experiments. We plotted the take-off and landing tracks in Figure 4.22 for experiments conducted on Sept. 13 and 15, 1993, and on Sept. 28 and 30, 1995. As soon as the aircraft is running on the ground in both cases, the estimated heights of the GPS antenna are consistent within 6 cm for most parts of tracks. The mean differences are 1.8, 3.1, 2.5 and 1.2 cm for experiments conducted on Sept. 13 and 15, 1993, and on Sept. 28 and 30, 1995, respectively. Figure 4.23 shows more details of the runway track for take-

off and landing tracks on Sept. 30, 1995. The measured landing height of the aircraft on the runway repeats almost exactly the takeoff track after nearly a 4 hour flight. The good agreement between the runway positions before the take-off and after the landing in the same flight demonstrates the reliability of ambiguity resolution in our algorithm. If we mishandle the cycle slip and initial ambiguity bias for any satellites during flight, we would have obtained an end position far away from the initial position. The high consistency between the different flights shows that GPS has the ability to obtain a cm-level precision position for aircraft tracking at high speeds. Even after two years, most of the flights fit into old tracks within a few centimeters in their height measurements.

References

Chen, G., T. A. Herring and R. W. King, TRACK software manual, MIT, in preparing, 1998.

Goad, C.C., Grejner-Brzezinska, D.A. and Yang M., Determination of high-precision GPS orbits using triple differencing technique. *J. of Geodesy*, **70**, p. 655-62, 1997

Gurtner, W., G. Mader, The RINEX Format: Current Status, Future Developments. *Proceedings of the Second International Symposium of Precise Positioning with the Global Positioning system, Ottawa,* pp977, 1990.

Hofton, M., J. Blair, B. Minster, J. Ridgway, D. Rabine, J. Bufton, and N. Williams, Using laser altimetry to detect topographic change at long Valley caldera, California, *Earth Surface Remote Sensing, SPIE 3222,* 295-306, 1997.

King, R. & Bock Y., Documentation for the GAMIT GPS Analysis Software, *MIT Geodesy and Geodynamics Lab*, 1998.

Martin C., GITAR program documentation, *NASA contract number NAS5-31558, Goddard Space Flight Center, Wallops Flight Facility, Wallops Island, VA*, 1991.

Murata, M.; Harigae, M. and Tsujii, T., GPS positioning with broadcast and precise ephemerides, SICE '95. *Proceedings of the 34th SICE Annual Conference*, p. 519, 1995

Remondi, B. W., NGS Second Generation ASCII and Binary Orbit Formats and Associated Interpolation Studies, *Poster session presentation at the Twentieth General Assembly of the IUGG, Vienna, Austria, August 11 - 24,* 1991.

Ridgway,J.R., J.B. Minster, N.P. Williams, J.L. Bufton, and W. Krabill, Airborne laser altimetry survey of Long Valley, California, *Geophys. J. Int. 131,* 267-280, 1997.

Figure Captions

Figure 4.1 Locations of the airport and the base GPS station at Bishop, California. The circle is the geodetic position of the GPS receiver mounted on a permanent benchmark as the reference station. There are two trailers (lighter rectangles) near the GPS ground receiver. At 500 meters southeast is Bishop Airport, where the T-39 aircraft, parked on the runway during experiments in 1993 and 1995. The diamond dark spots represent several different starting positions of flights for the aircraft.

Figure 4.2. Relative height values for the aircraft while it was stationary calculated from P1 (the darker line) and P2 (the lighter line) single frequency code measurements during the Long Valley survey on the Sept. 28, 1995. The difference in the average height is 14.7 cm over 30 minutes. Because the distance between the GPS base receiver and the GPS aircraft receiver of the base station is short (< 1 km), unmodeled atmospheric and ionospheric effects are not likely to contribute to these differences between P1 and P2 solutions. Range data noise and the multipath contribute mostly to the differences.

Figure 4.3. The trajectory of the aircraft during the Long Valley survey on Sept. 13, 1993. We used the WGS-84 ellipsoidal system as the reference system. The heights are the ellipsoidal elevations (upper plot) and vary to keep a 500 meter relative height over the ground for ATLAS laser measurements. This flight repeats the measurement sections (straight lines in horizontal trajectory) over crossover points (Antelope Springs and Benton Crossing) and along lake Crowley twice.

Figure 4.4. The trajectory of the aircraft in the survey on Sept. 14, 1993. The trajectory is not completed due to the receiver problem on the ground base station. (see Figure 4.3 for details)

Figure 4.5. The trajectory of the aircraft in the survey on Sept. 15, 1993. (see Figure 4.3 for

details).

Figure 4.6. The top plot shows the uncertainty values of the estimated heights of the aircraft calculated with (the darker line) and without (lighter line) atmospheric (ATM) parameters (the lighter line). Data analyses are performed with the L3 data of Sept. 13, 1993. In the bottom plot, we show the satellite availability during the entire flight. The elevation cutoff angle for observations is 15 degree. At times, the total PRN satellite number is just four, which makes the solution with atmospheric variations a little worse. When the satellite availability is down to 5 or even 4, the uncertainties of position determination can up to 20 cm for the height. When the data noise is assumed to be 5 cm, The smoothness in the changes of the height uncertainties when the atmospheric parameters are estimated and the number of satellite changes is due to the process noise on the ATM parameter.

Figure 4.7, Post-fit L3 phase residuals for some satellites from Sept. 13, 1993 data analysis. After the fixing of cycle slips, there are no over 0.2 cycle (3.8 cm) for any of the observations. The ambiguities for new satellites that rose during the flight appear to be resolved correctly, so that there are no jumps in the residual time series when satellites come in or drop out of the solution. The RMS scatters of the residuals in each frame are 0.8, 0.9, 1.2, 1.1, 1.1, 0.6, 0.8, 0.9 cm for satellites PRN16, 02, 07, 09, 12, 13, 24, and 26, respectively.

Figure 4.8, Residual variations of some satellite observations used in the calculation for the aircraft GPS data analysis on Sept. 14, 1993. (See similar comments in Figure 4.7)

Figure 4.9, Residual variations of some satellite observations used in the calculation for the aircraft GPS data analysis on Sept. 15, 1993. (See similar comments in Figure 4.7)

Figure 4.10, The trajectory of the aircraft on Sept. 28, 1995 calculated by our kinematic GPS software. The elevation of aircraft flight is over 5 km for middle altitude laser survey using SLICER. At such height, the aircraft could fly horizontally without worrying about the mountains. The horizontal region is also extended compared to the 1993 surveys (Figures 4.4-4.6).

Figure 4.11, The trajectory of the aircraft on Sept. 29, 1995 calculated by our kinematic GPS software.

Figure 4.12, The trajectory of the aircraft on Sept. 30, 1995 calculated by our kinematic GPS software. The elevation of aircraft flight is at the level 5 km and 10 km. The horizontal region also extends to be almost as twice large as that in the 1993 surveys.

Figure 4.13, Residual variations of some satellite observations used in the calculation for the aircraft GPS data analysis on Sept. 28, 1995.

Figure 4.14, Residual variations of some satellite observations used in the calculation for the aircraft GPS data analysis on Sept. 29, 1995. As the relative height and horizontal distance increase for two GPS receivers, the differential GPS cannot efficiently eliminate all elevation-related model errors, so the residuals show more noise than those for the lower height flights of the 1993 surveys.

Figure 4.15 a) The tracks (Up, North, East) for the T39 aircraft sitting on the runway before taking off on Sept. 13, 1993. The results are derived from differential GPS tracking with two ASHTECH GPS receivers, one on the base station, the other on the roof of the T39 aircraft. L3 is used for the calculation.

b) The track changes for the T39 aircraft sitting on the runway before taking off on Sept. 14, 1993.

c) The track changes for the T39 aircraft sitting on the runway before taking off on Sept. 15, 1993. The variations are larger than those from Sept. 13 and 14 possibly be caused of the strong multipath from the aircraft parking place on this date.

Figure 4.16. The normalized autocorrelation functions of the time series of estimated height errors of the aircraft. The data are from surveys on Sept. 13-15, 1993, Sept. 28 and 30, 1995 when the aircraft sat on the runway. Data sampling is 2 Hz. The flat line is the 1/e value which defines the autocorrelation length. The lighter line (the most outside line) is from

the Sept. 14,1993 survey.

Figure 4.17. The trajectory of the T39 aircraft sitting on the runway after landing (Sept. 13,1993). In the upper plot, the darker line represents the results continuing from the kinematic calculation which started before the aircraft took off. Then we start an independent static survey after the T39 aircraft landed (the lighter line). The position process noise of Φ_w is chosen as 10^{-4} m^2/s for the "static" mode comparing to the 10^4 m^2/s used in the kinematic mode. The two lines agree well in their height variations. The lower plot shows their differences which is averaged less than 1 cm.

Figure 4.18. Aircraft tracks estimated from our GPS kinematic analyses both in the 1993 and 1995 surveys. The tracks are results from Sept. 13-15, 1993; Sept. 28, 30 and Oct. 5, 1995. Plot shows tracks of the aircraft running on the runway (horizontal view)

Figure 4.19. Aircraft tracks estimated from our GPS kinematic analyses both in 93's and 95's surveys. The tracks are results from Sept. 13-15, 1993; Sept. 28, 30 and Oct. 5, 1995. Plot shows altitudes of the aircraft running on the runway in the east direction (vertical view)

Figure 4.20. Detailed estimated track heights of the aircraft on the taxiway with the GPS kinematic surveying. The upper plot is enlarged from Figure 4.19 with the same data. This plot shows the aircraft running on the taxiway with speed less than 10m/s. The lower plots shows how the other five tracks differ from the track of the Oct. 5, 1995. The averaged difference is 1.7 cm for five track differences. The averaged internal RMS for each track is 0.9 cm.

Figure 4.21. Detailed estimated track heights of the aircraft on the main runway during the take-offs. The upper plot is enlarged from Figure 4.19 with the same data. The data come from days Sept. 13, 14,15 of 1993 and Sept. 28, 30 and Oct. 5 of 95. This plot shows the aircraft running on the runway with low to high speed 10 - 70 m/s. The lower plots shows how the other five tracks differ from the track of Oct. 5, 1995. The error bars are 4.1 cm, the single epoch vertical uncertainty in the track obtained on Sept. 30, 1993.

Figure 4.22. Comparison of the estimated track heights of the aircraft on the main runway when aircraft is taking off and landing with high speed (40-70 m/s). The data are obtained from days Sept. 13, 15 of 1993 and Sept. 28, 30 of 1995. The darker line is the landing track while the lighter line is the takeoff track.

Figure 4.23 Enlarged portion of track heights of the aircraft on the main runway during takeoff and landing for experiment on Sept. 30, 1995.

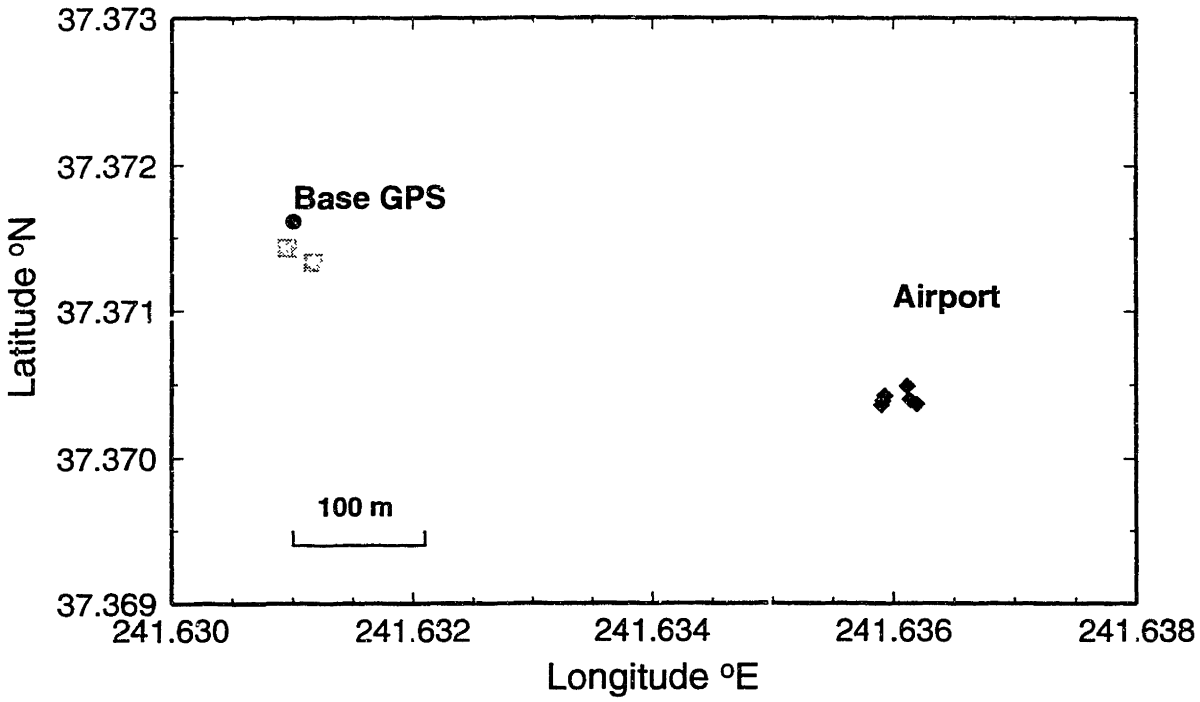
37.373
37.372
37.371
37.370
37.369
Latitude °N
Base GPS
Airport
100 m
241.630
241.632
241.634
241.636
241.638
Longitude °E

Figure 4.1

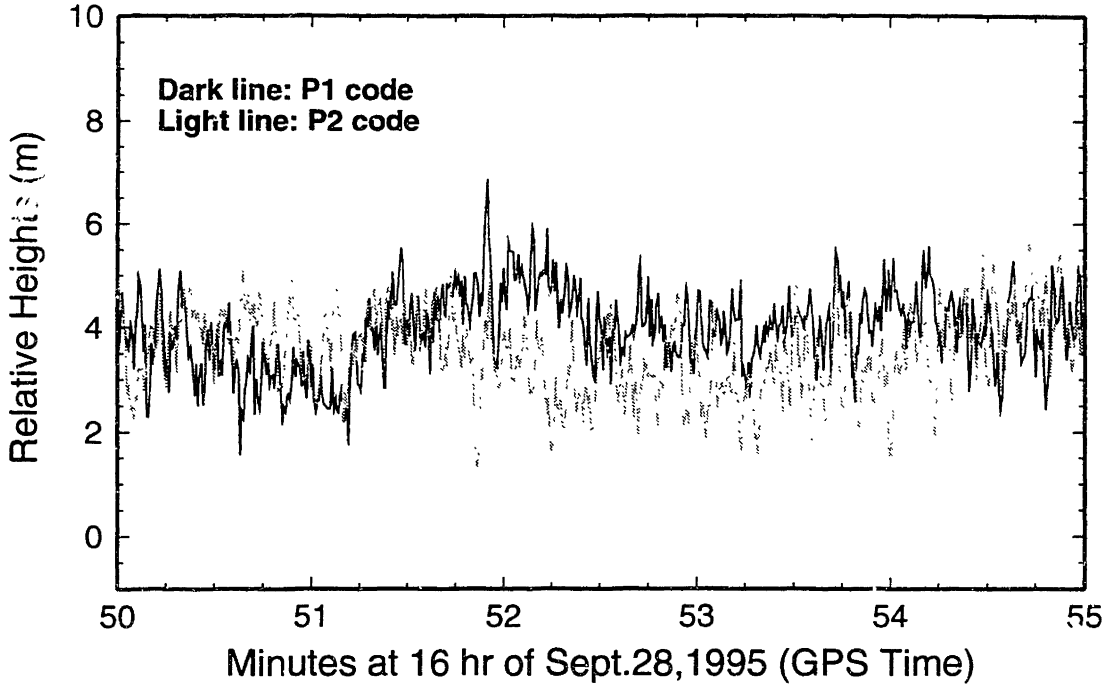
Dark line: P1 code
Light line: P2 code
Relative Height (m)
10
8
6
4
2
0
50
51
52
53
54
55
Minutes at 16 hr of Sept.28,1995 (GPS Time)

Figure 4.2

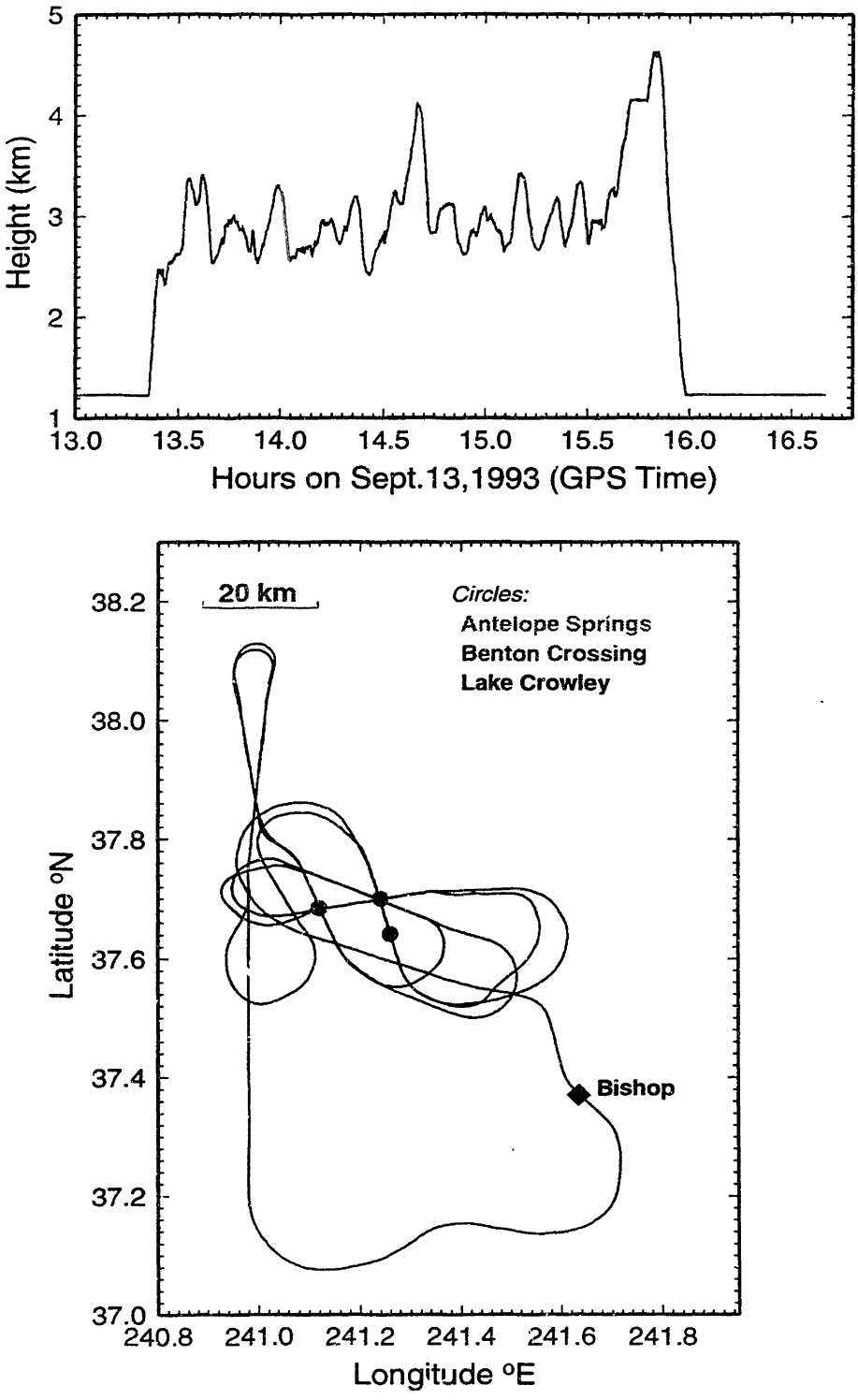
Height (km)
5
4
3
2
1
13.0
13.5
14.0
14.5
15.0
15.5
16.0
16.5
Hours on Sept.13,1993 (GPS Time)
20 km
Circles:
Antelope Springs
Benton Crossing
Lake Crowley
Bishop
Latitude °N
38.2
38.0
37.8
37.6
37.4
37.2
37.0
240.8
241.0
241.2
241.4
241.6
241.8
Longitude °E

Figure 4.3

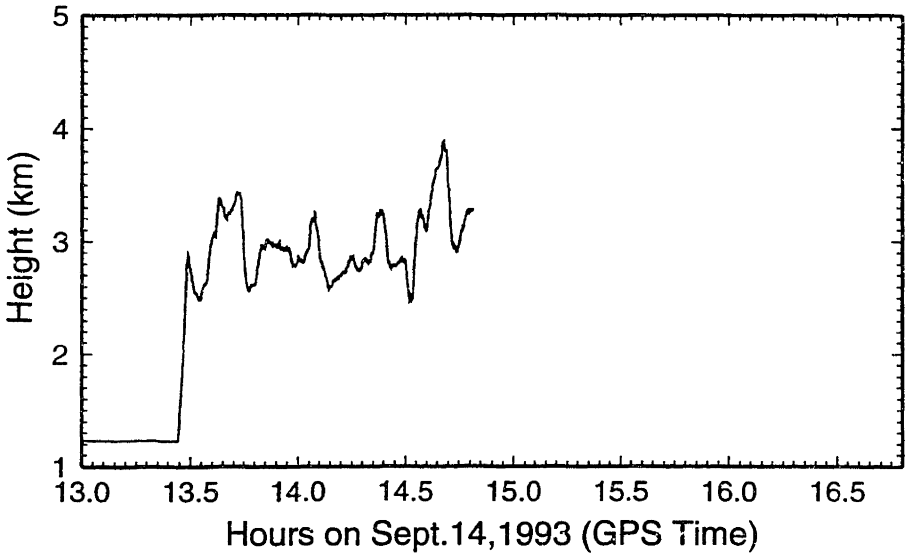
Height (km)
5
4
3
2
1
13.0
13.5
14.0
14.5
15.0
15.5
16.0
16.5
Hours on Sept.14,1993 (GPS Time)

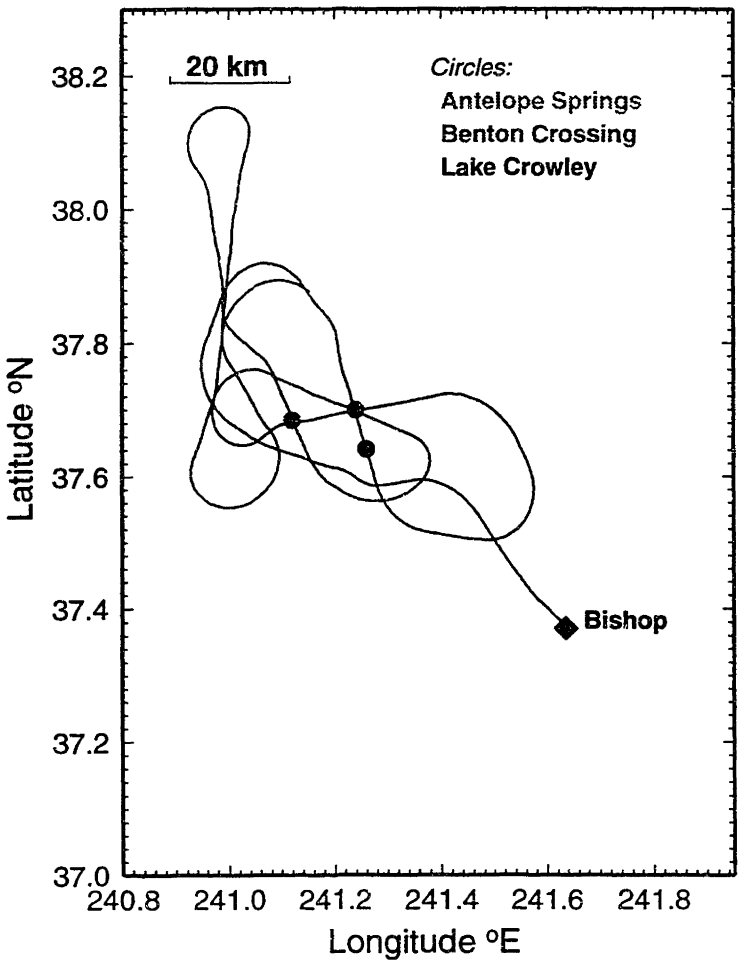
20 km
Circles:
Antelope Springs
Benton Crossing
Lake Crowley
Bishop
Latitude °N
38.2
38.0
37.8
37.6
37.4
37.2
37.0
240.8
241.0
241.2
241.4
241.6
241.8
Longitude °E

Figure 4.4

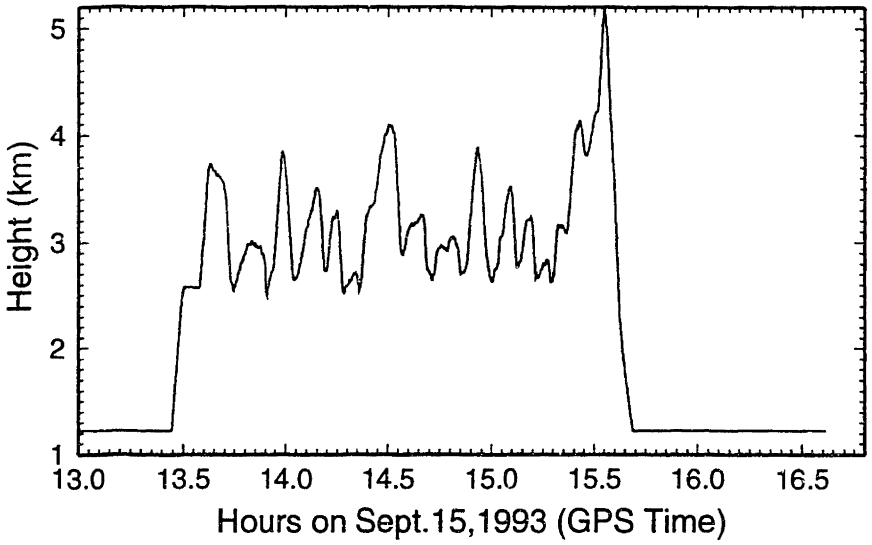
Height (km)
5
4
3
2
1
13.0
13.5
14.0
14.5
15.0
15.5
16.0
16.5
Hours on Sept.15,1993 (GPS Time)

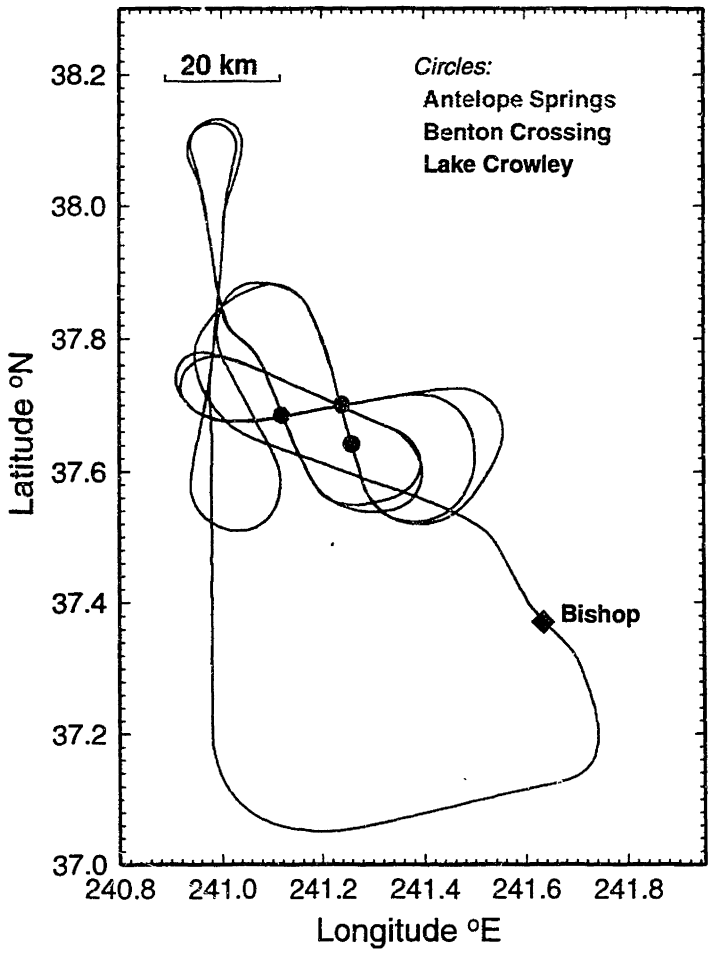
20 km
Circles:
Antelope Springs
Benton Crossing
Lake Crowley
Bishop
Latitude °N
38.2
38.0
37.8
37.6
37.4
37.2
37.0
240.8
241.0
241.2
241.4
241.6
241.8
Longitude °E

Figure 4.5

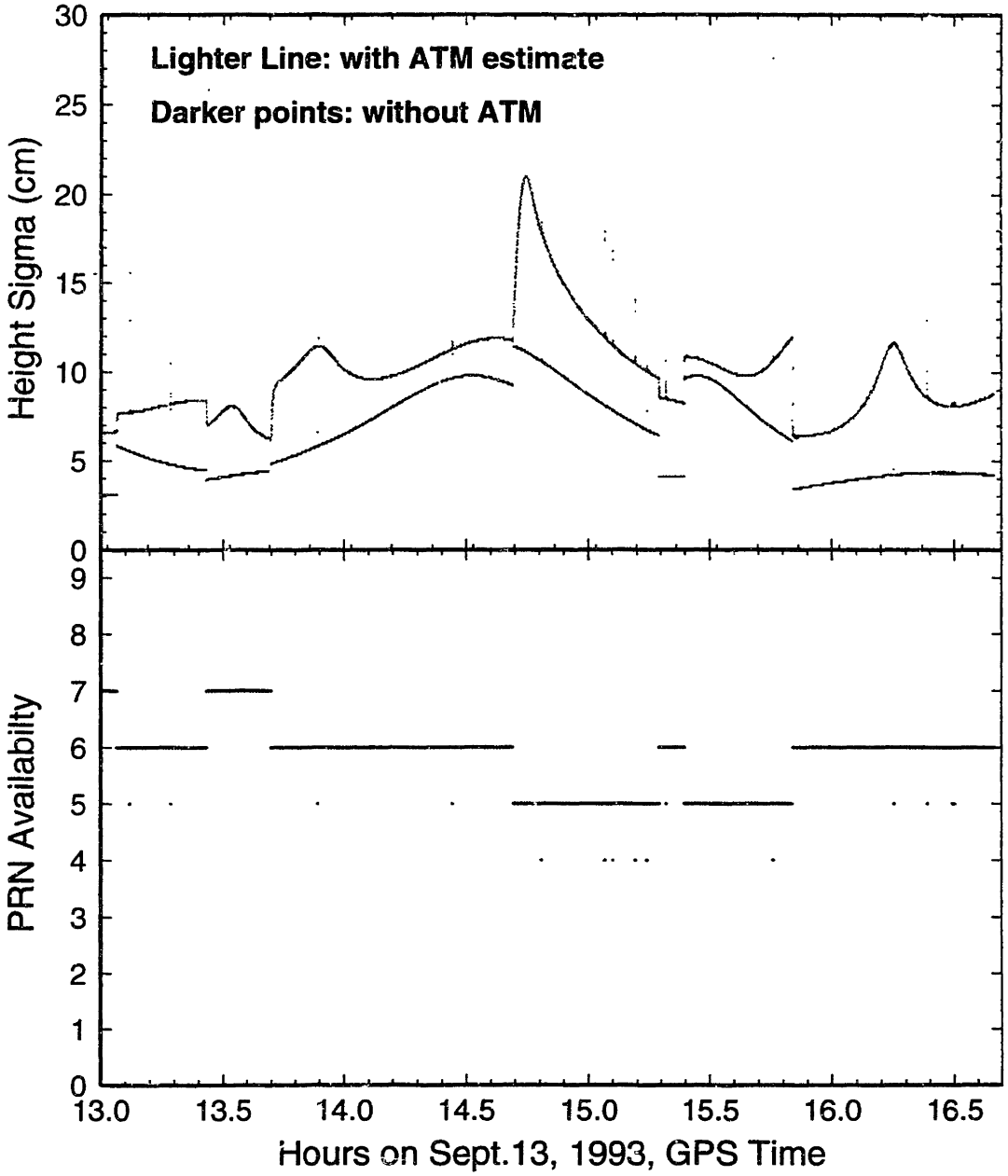
Lighter Line: with ATM estimate
Darker points: without ATM
Height Sigma (cm)
PRN Availability
Hours on Sept.13, 1993, GPS Time

Figure 4.6

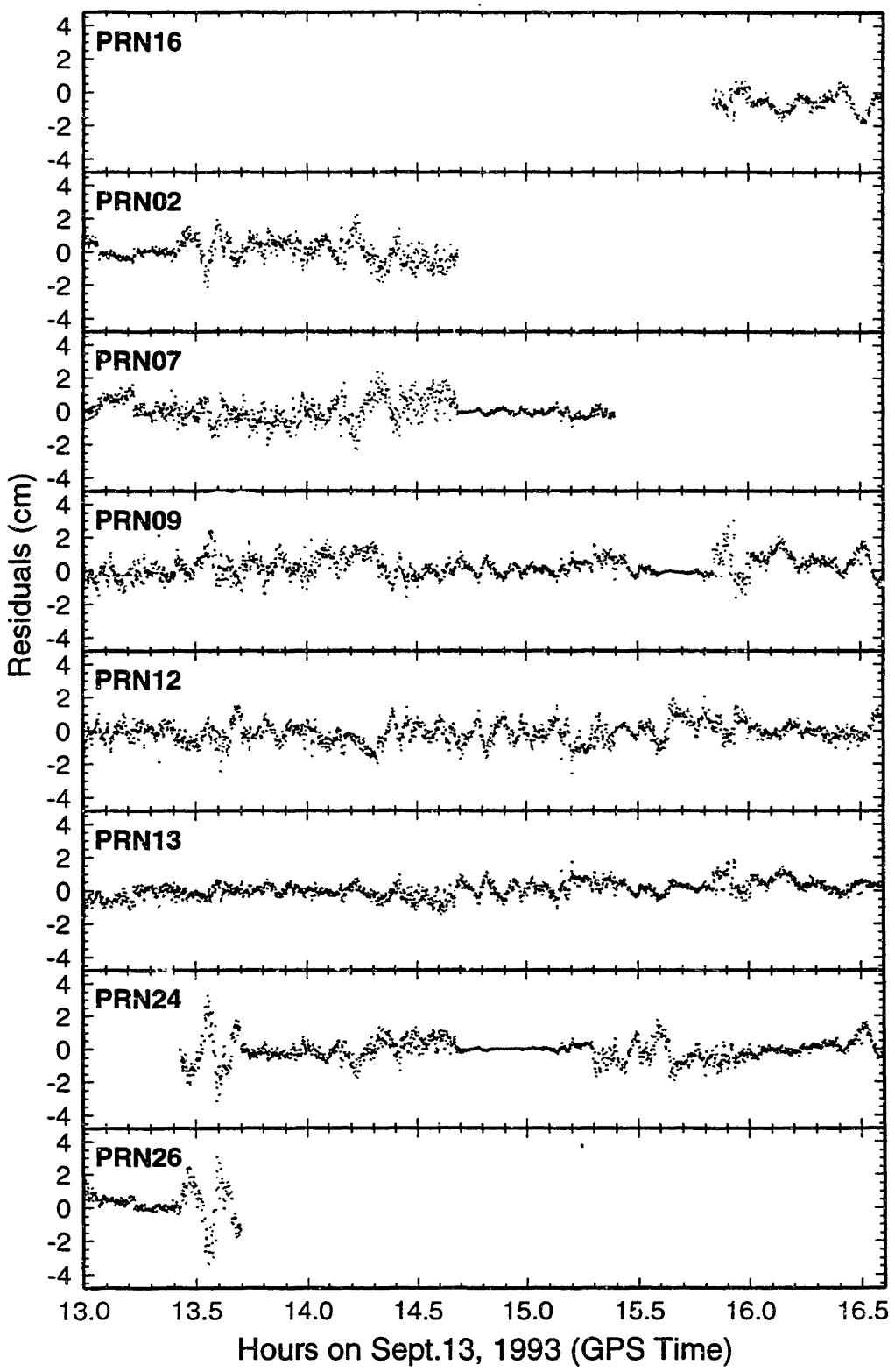
PRN16
PRN02
PRN07
PRN09
PRN12
PRN13
PRN24
PRN26
Residuals (cm)
4
2
0
-2
-4
13.0
13.5
14.0
14.5
15.0
15.5
16.0
16.5
Hours on Sept.13, 1993 (GPS Time)

Figure 4.7

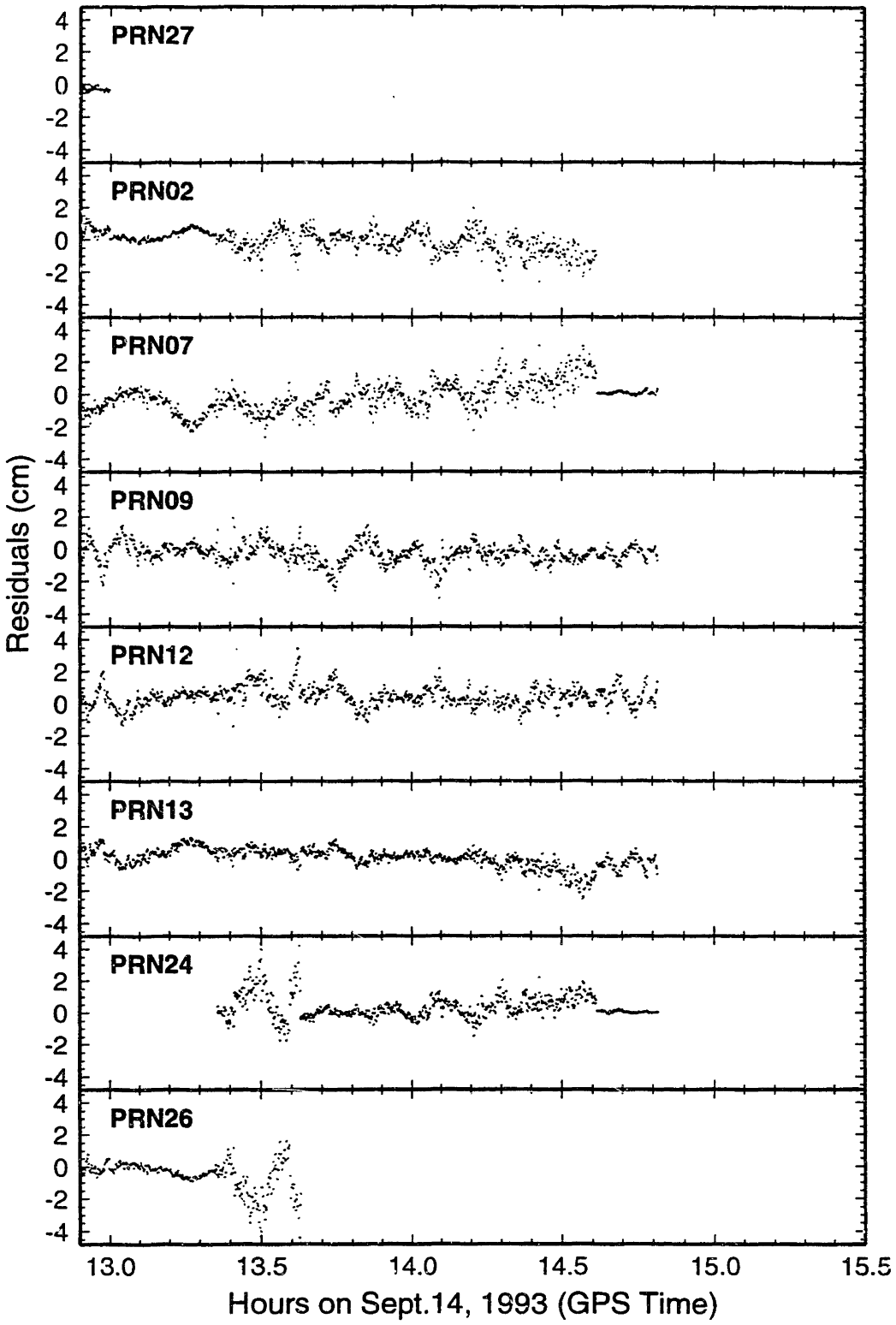
PRN27
PRN02
PRN07
PRN09
PRN12
PRN13
PRN24
PRN26
Residuals (cm)
4
2
0
-2
-4
13.0
13.5
14.0
14.5
15.0
15.5
Hours on Sept.14, 1993 (GPS Time)

Figure 4.8

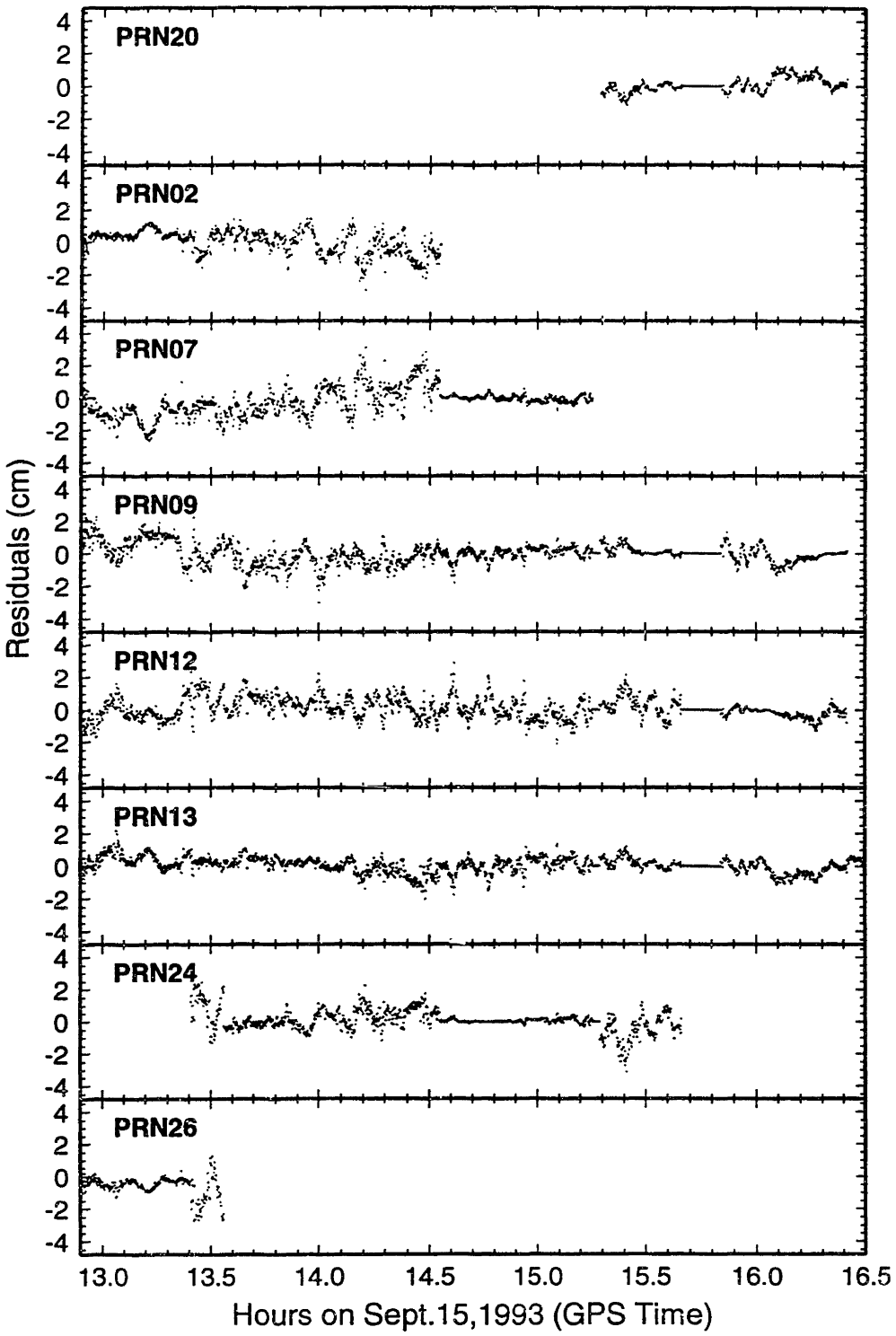
PRN20
PRN02
PRN07
PRN09
PRN12
PRN13
PRN24
PRN26
Residuals (cm)
4
2
0
-2
-4
13.0
13.5
14.0
14.5
15.0
15.5
16.0
16.5
Hours on Sept.15,1993 (GPS Time)

Figure 4.9

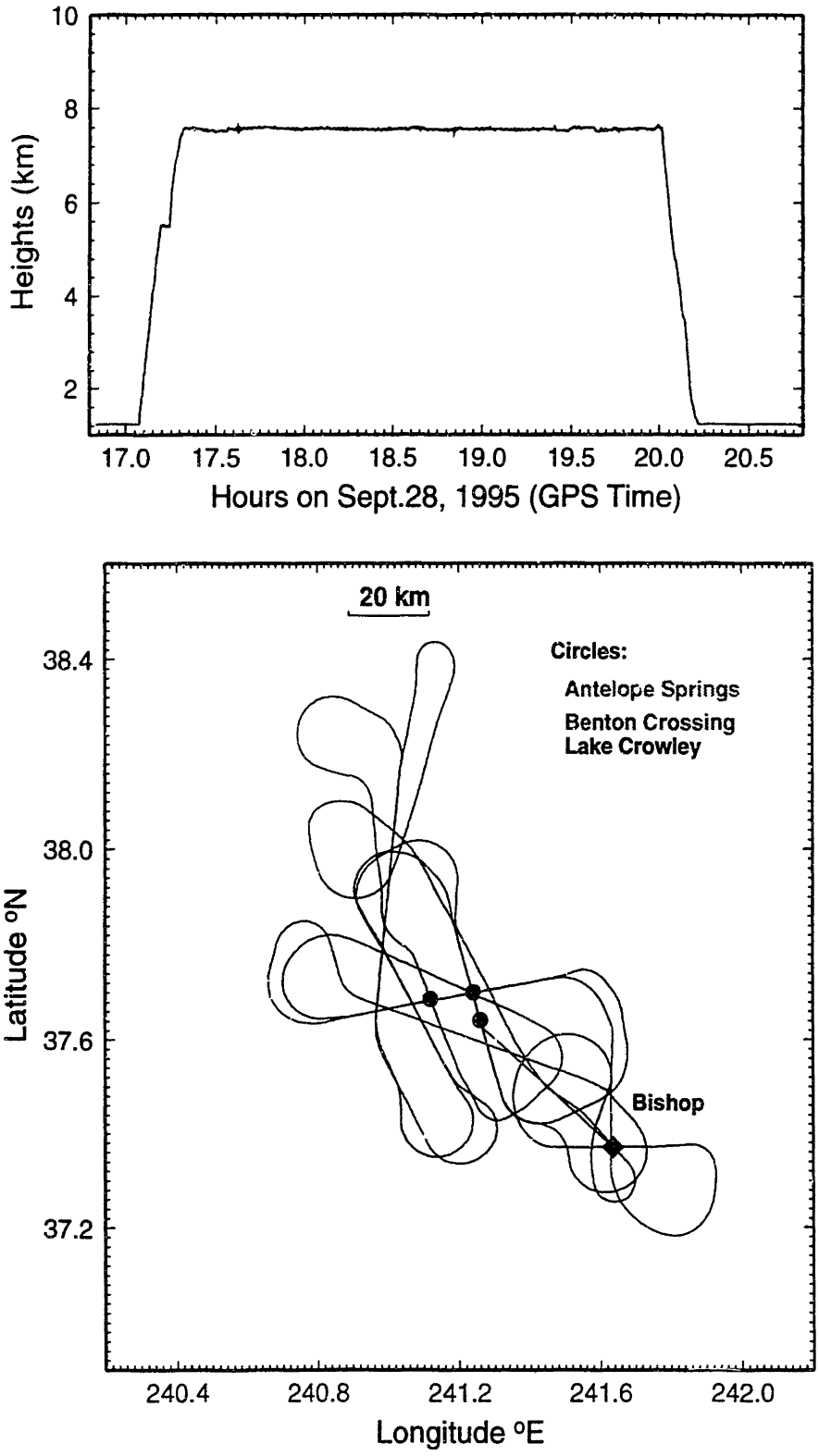
10
8
6
4
2
Heights (km)
17.0
17.5
18.0
18.5
19.0
19.5
20.0
20.5
Hours on Sept.28, 1995 (GPS Time)
20 km
Circles:
Antelope Springs
Benton Crossing
Lake Crowley
Bishop
38.4
38.0
37.6
37.2
Latitude °N
240.4
240.8
241.2
241.6
242.0
Longitude °E

Figure 4.10

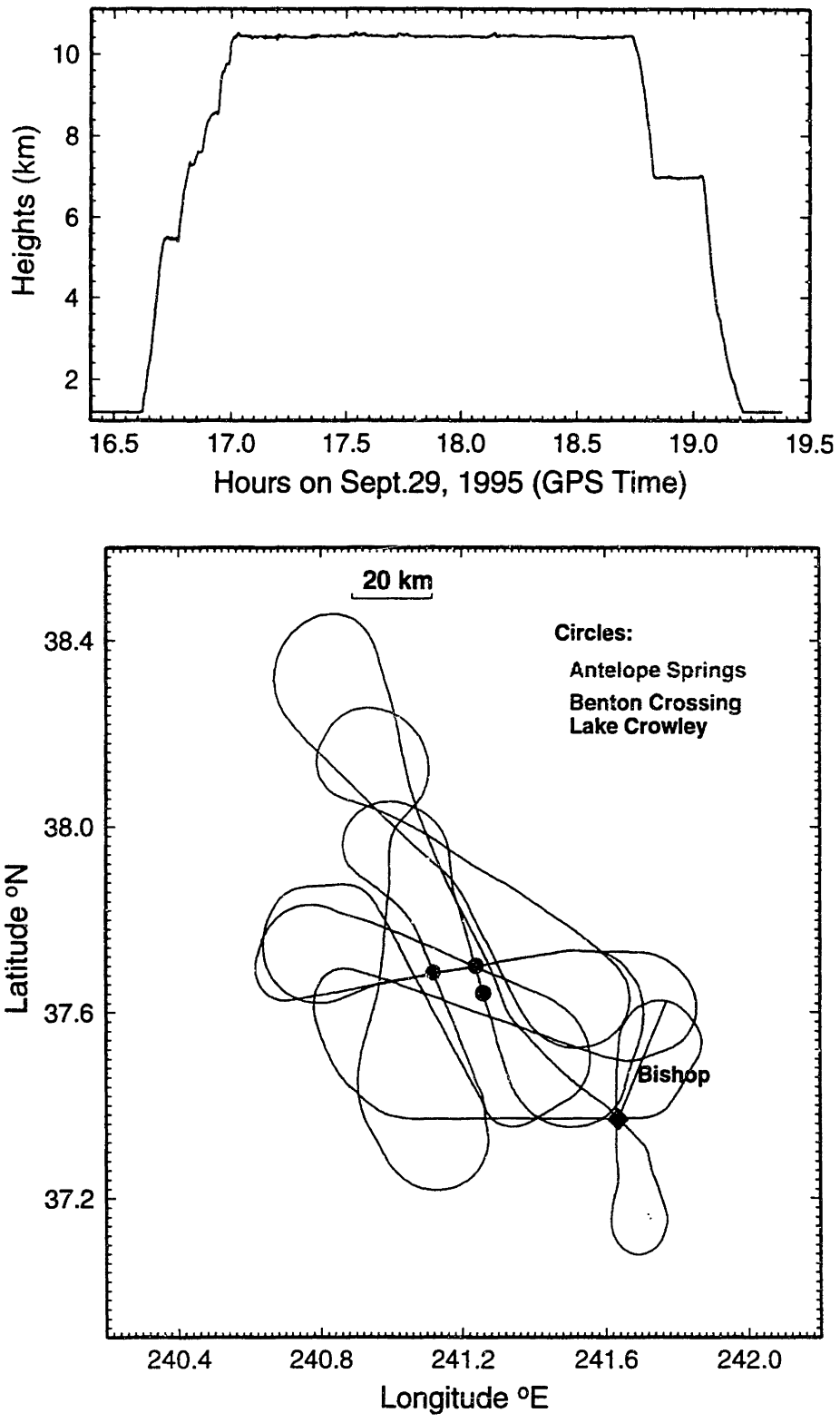
Heights (km)
10
8
6
4
2
16.5
17.0
17.5
18.0
18.5
19.0
19.5
Hours on Sept.29, 1995 (GPS Time)
20 km
Circles:
Antelope Springs
Benton Crossing
Lake Crowley
Bishop
Latitude °N
38.4
38.0
37.6
37.2
240.4
240.8
241.2
241.6
242.0
Longitude °E

Figure 4.11

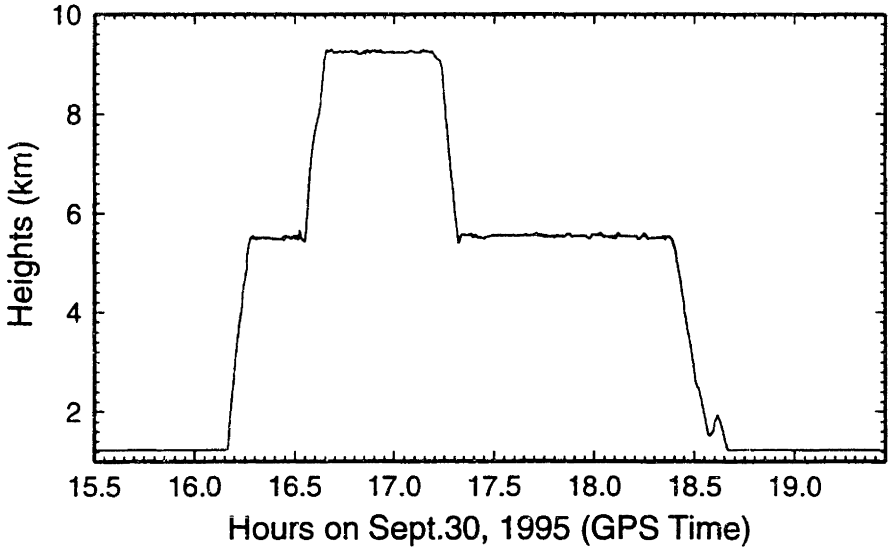
Heights (km)
10
8
6
4
2
15.5
16.0
16.5
17.0
17.5
18.0
18.5
19.0
Hours on Sept.30, 1995 (GPS Time)

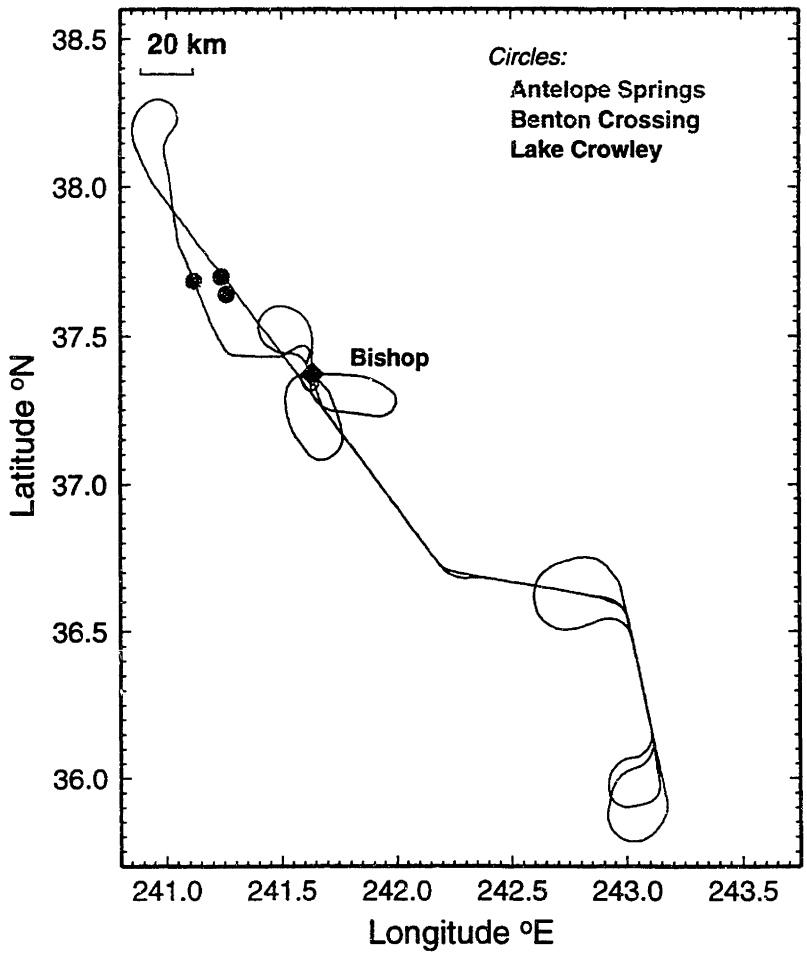
20 km
Circles:
Antelope Springs
Benton Crossing
Lake Crowley
Bishop
Latitude °N
38.5
38.0
37.5
37.0
36.5
36.0
241.0
241.5
242.0
242.5
243.0
243.5
Longitude °E

Figure 4.12

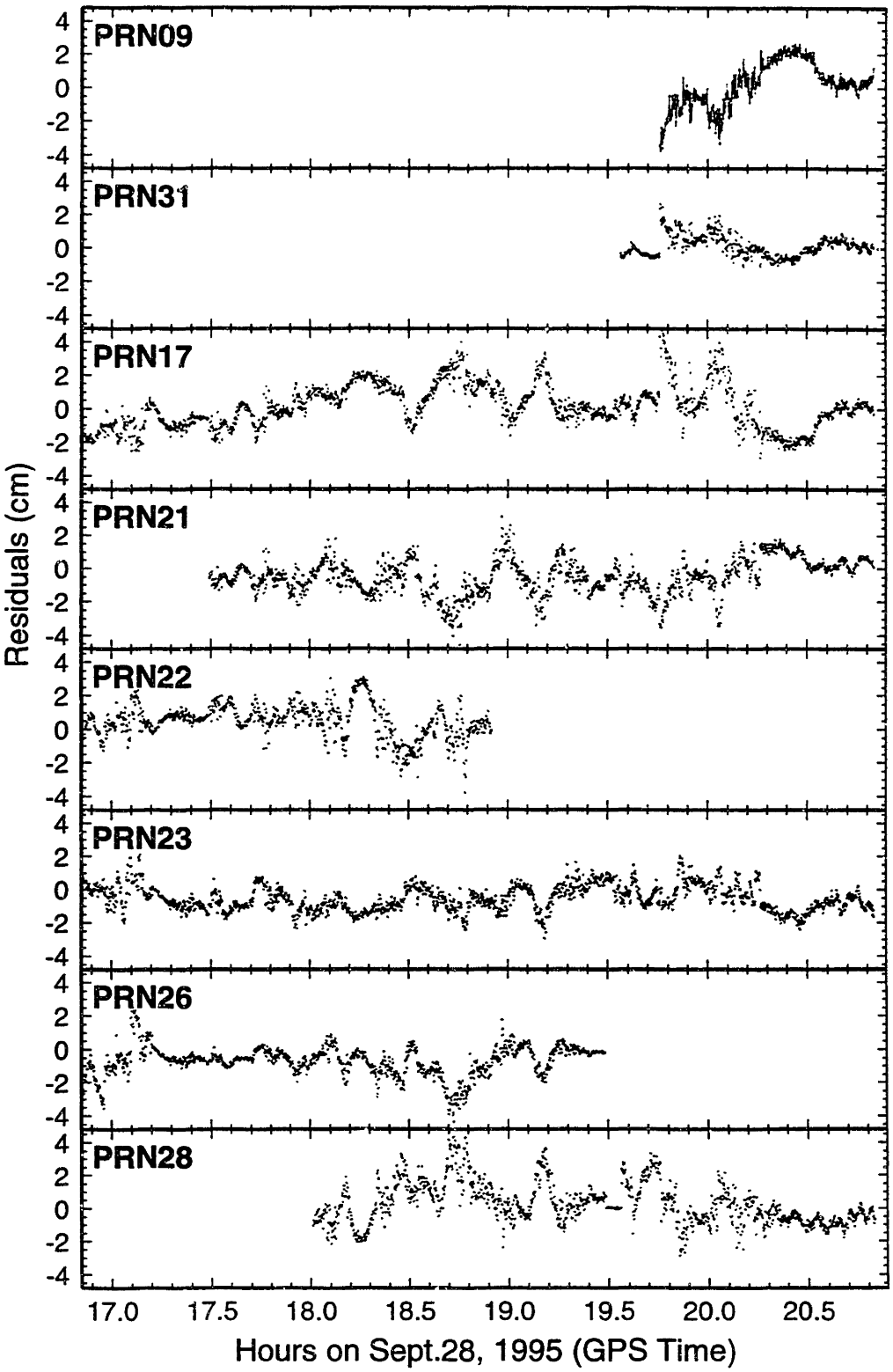
PRN09
PRN31
PRN17
PRN21
PRN22
PRN23
PRN26
PRN28
Residuals (cm)
4
2
0
-2
-4
17.0
17.5
18.0
18.5
19.0
19.5
20.0
20.5
Hours on Sept.28, 1995 (GPS Time)

Figure 4.13

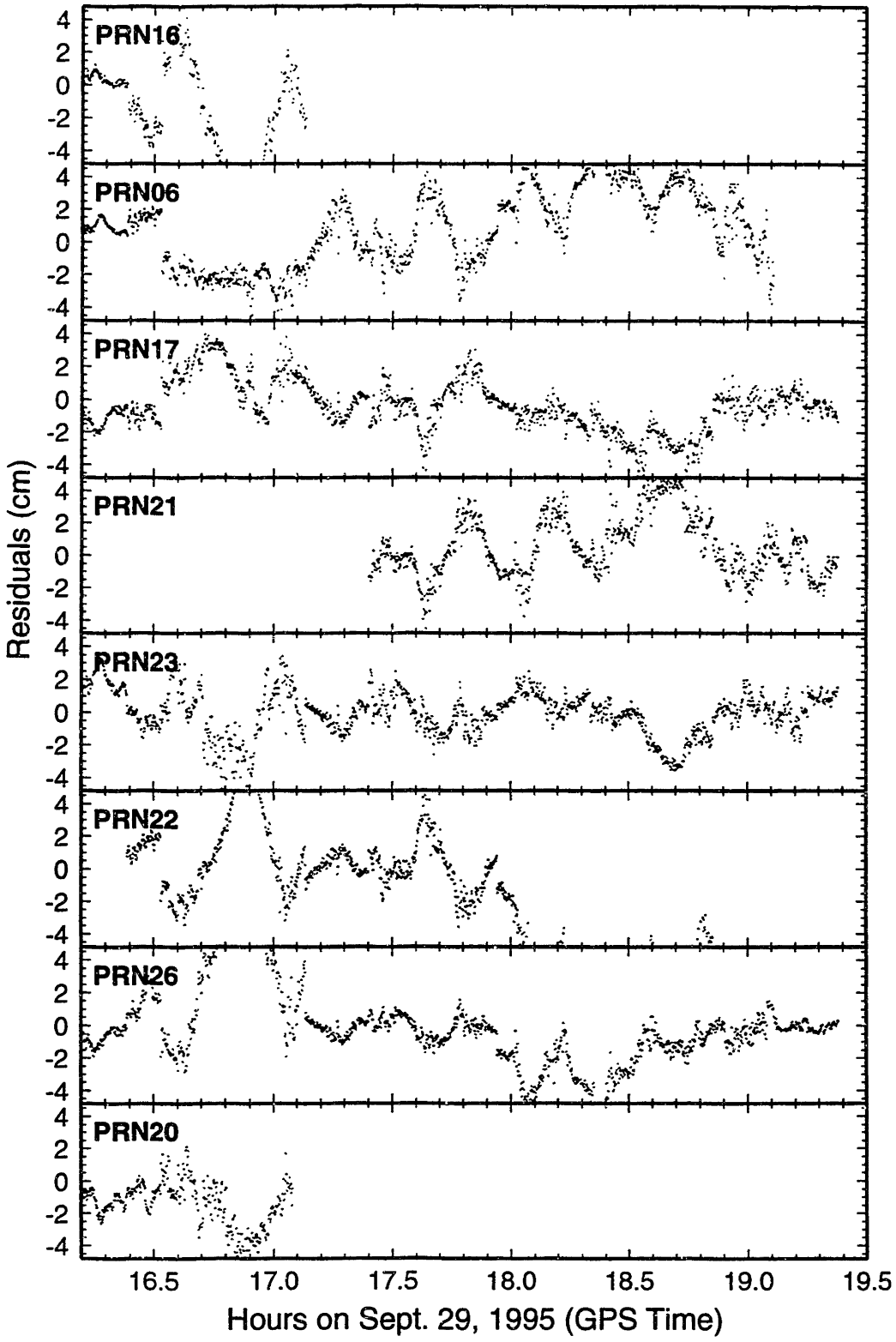
PRN16
PRN06
PRN17
PRN21
PRN23
PRN22
PRN26
PRN20
Residuals (cm)
4
2
0
-2
-4
16.5
17.0
17.5
18.0
18.5
19.0
19.5
Hours on Sept. 29, 1995 (GPS Time)

Figure 4.14

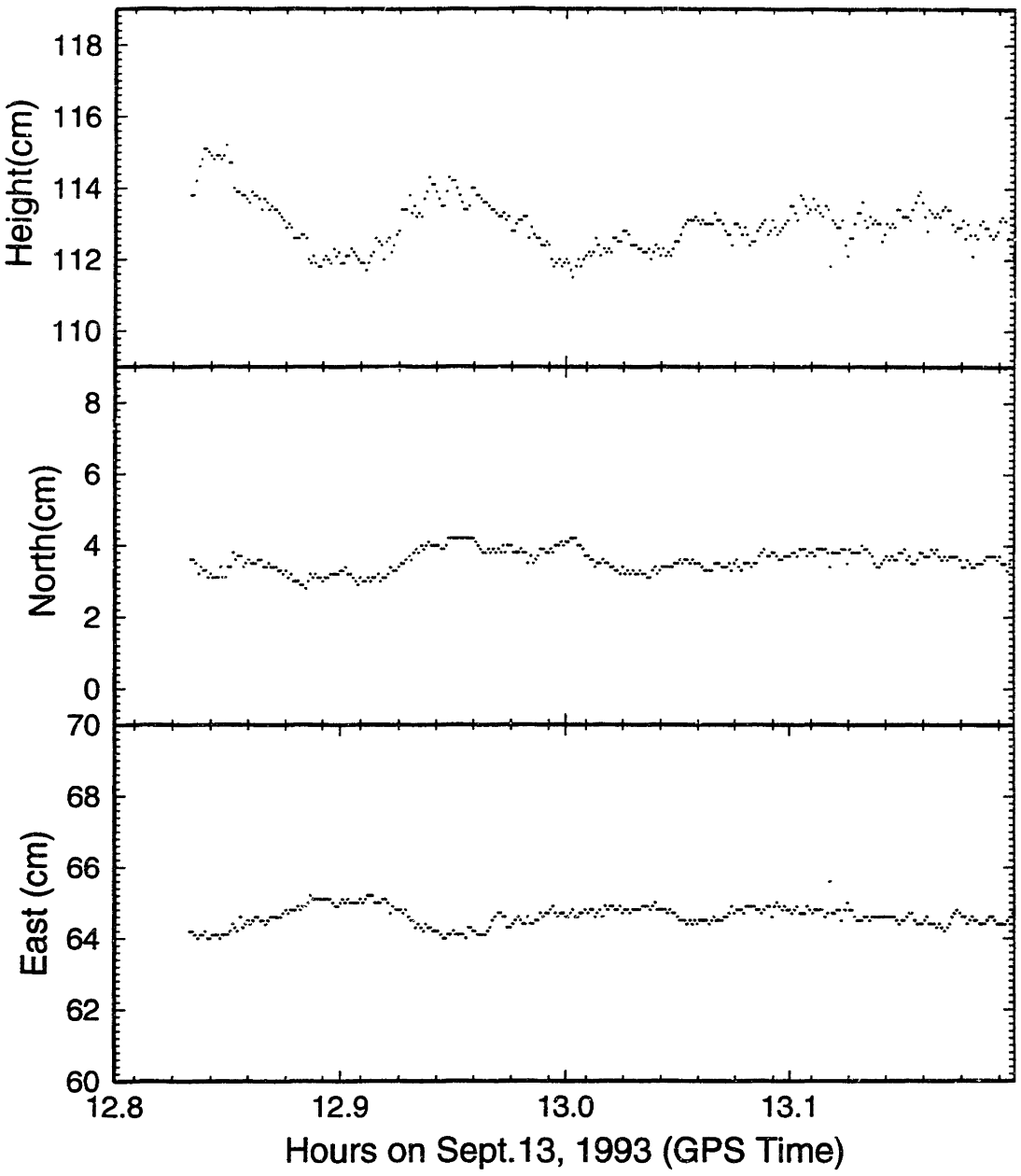
Height(cm)
118
116
114
112
110
North(cm)
8
6
4
2
0
East (cm)
70
68
66
64
62
60
12.8
12.9
13.0
13.1
Hours on Sept.13, 1993 (GPS Time)

Figure 4.15 a

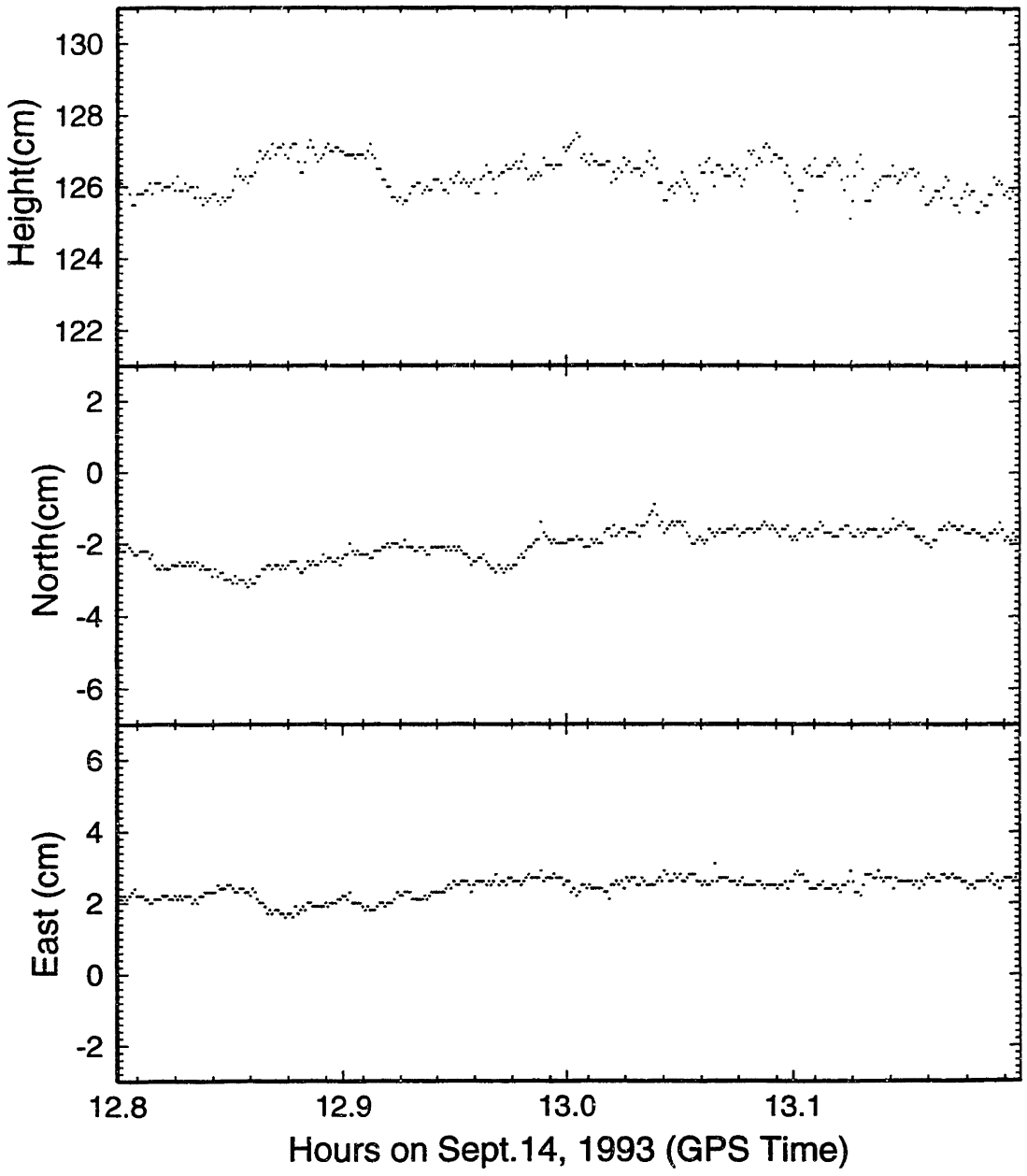
Height(cm)
130
128
126
124
122
North(cm)
2
0
-2
-4
-6
East (cm)
6
4
2
0
-2
12.8
12.9
13.0
13.1
Hours on Sept.14, 1993 (GPS Time)

Figure 4.15 b

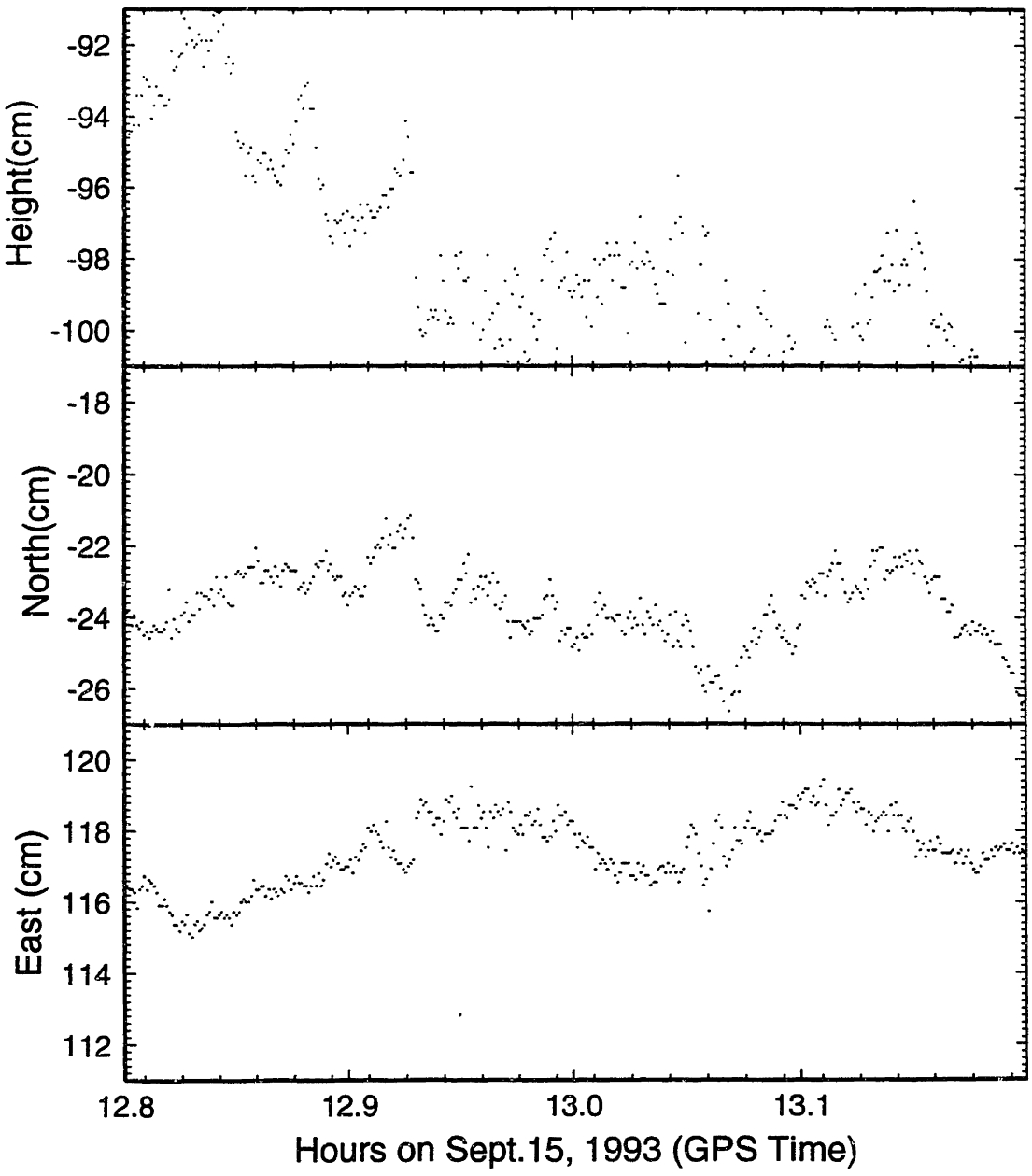
Height(cm)
-92
-94
-96
-98
-100
North(cm)
-18
-20
-22
-24
-26
East (cm)
120
118
116
114
112
12.8
12.9
13.0
13.1
Hours on Sept.15, 1993 (GPS Time)

Figure 4.15 c

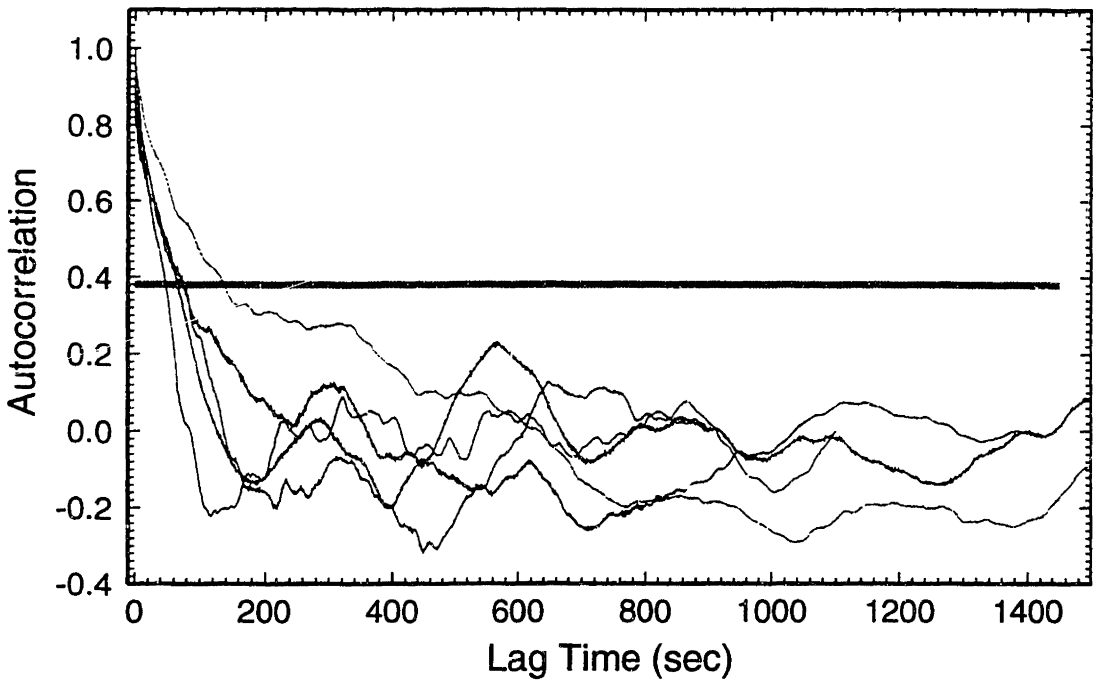
Autocorrelation
1.0
0.8
0.6
0.4
0.2
0.0
-0.2
-0.4
0
200
400
600
800
1000
1200
1400
Lag Time (sec)

Figure 4.16

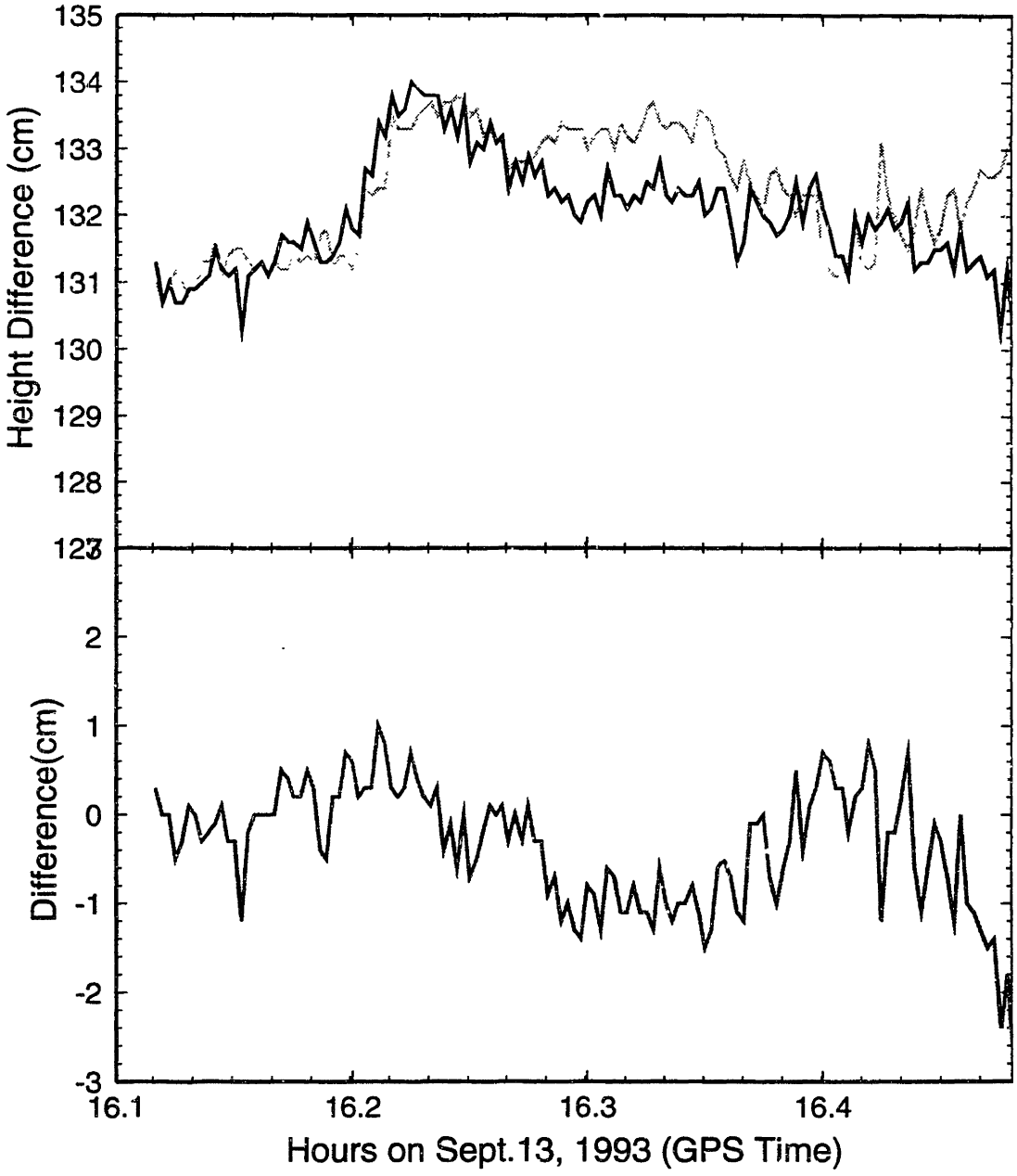
Height Difference (cm)
135
134
133
132
131
130
129
128
127
Difference(cm)
2
1
0
-1
-2
-3
16.1
16.2
16.3
16.4
Hours on Sept.13, 1993 (GPS Time)

Figure 4.17

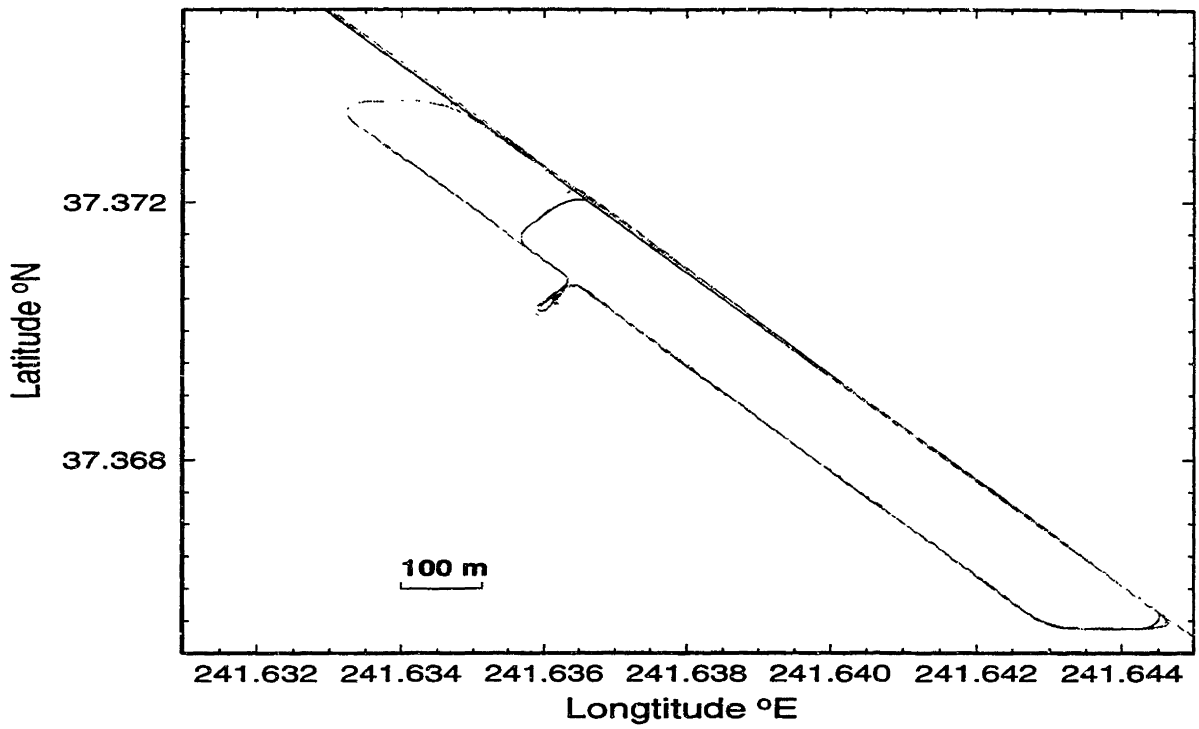
37.372
37.368
Latitude °N
100 m
241.632
241.634
241.636
241.638
241.640
241.642
241.644
Longtitude °E

Figure 4.18

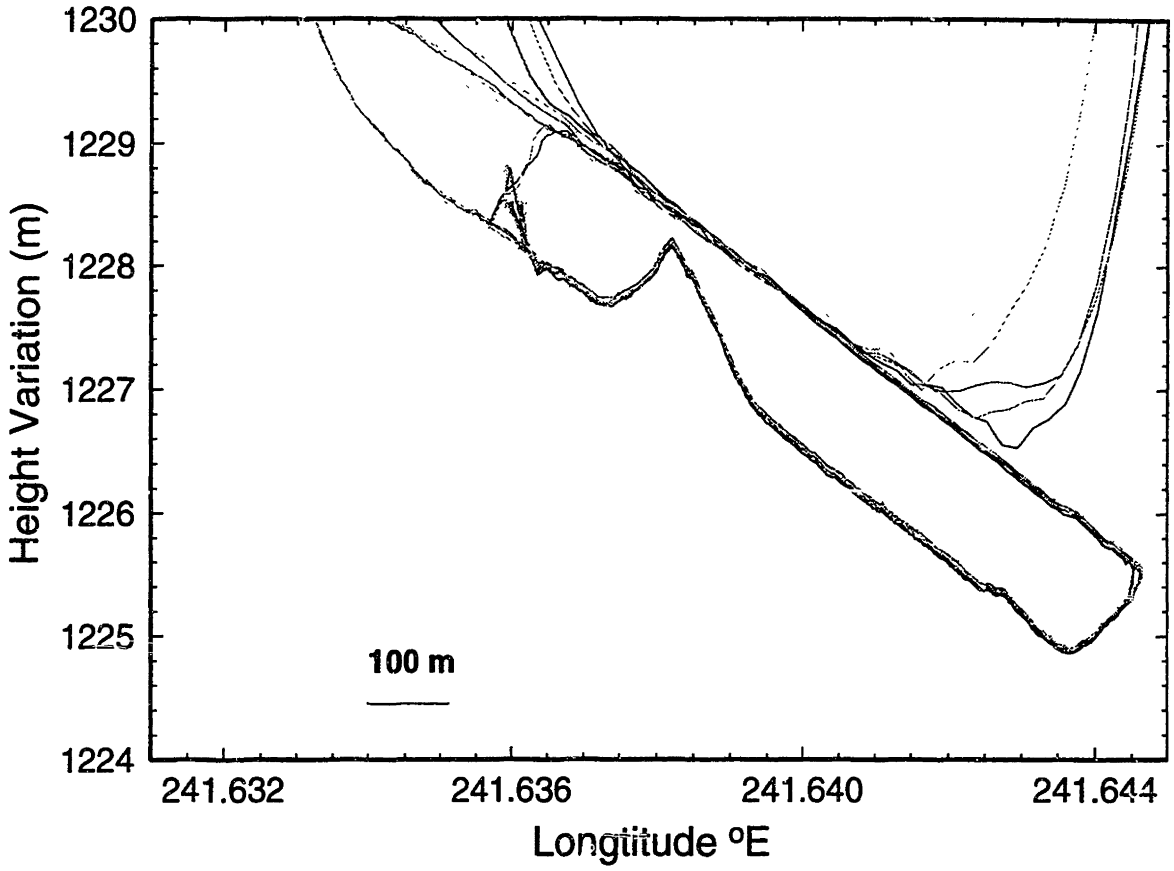
1230
1229
1228
1227
1226
1225
1224
Height Variation (m)
100 m
241.632
241.636
241.640
241.644
Longtitude °E

Figure 4.19

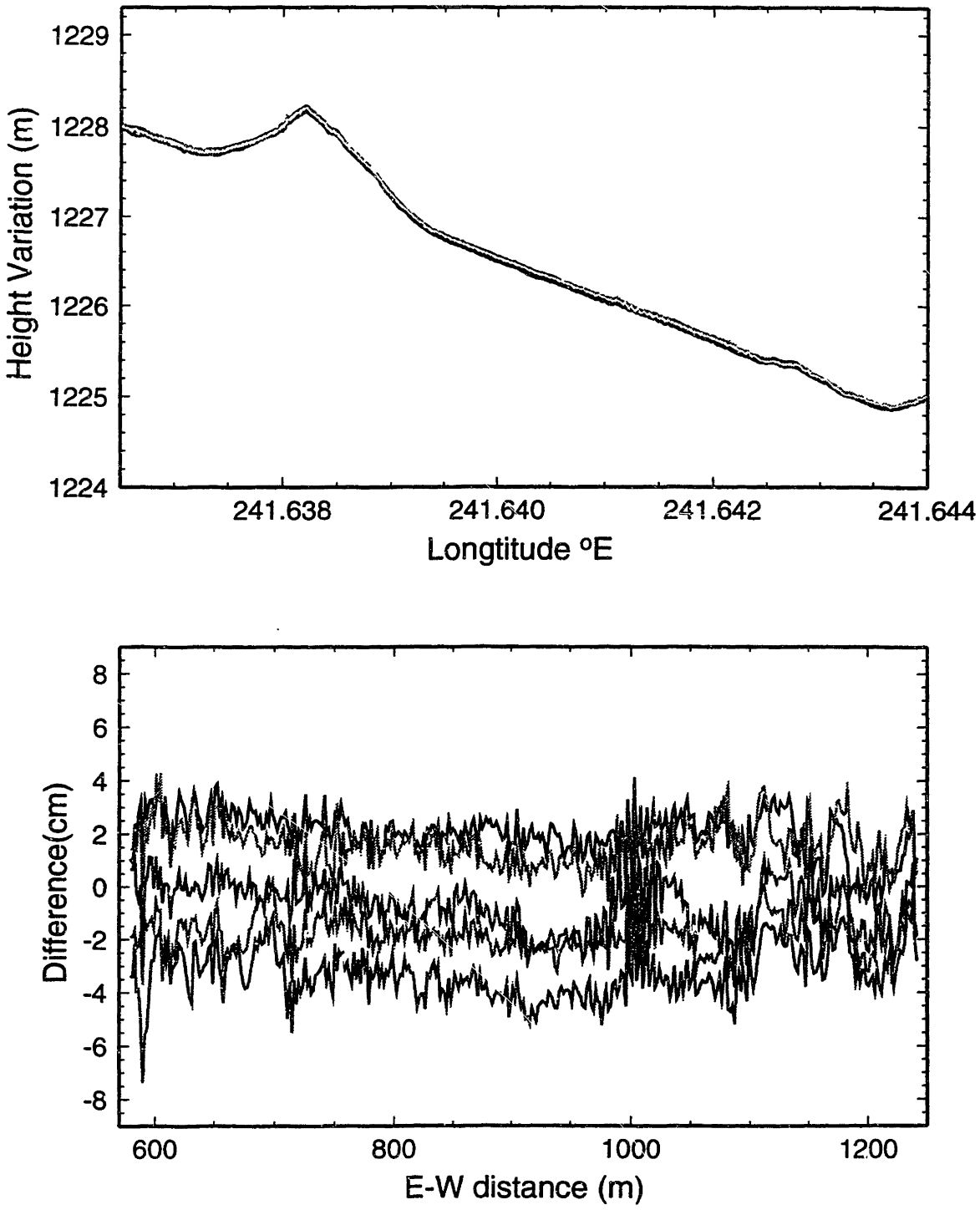
1229
1228
1227
1226
1225
1224
Height Variation (m)
241.638
241.640
241.642
241.644
Longtitude °E
8
6
4
2
0
-2
-4
-6
-8
Difference(cm)
600
800
1000
1200
E-W distance (m)

Figure 4.20

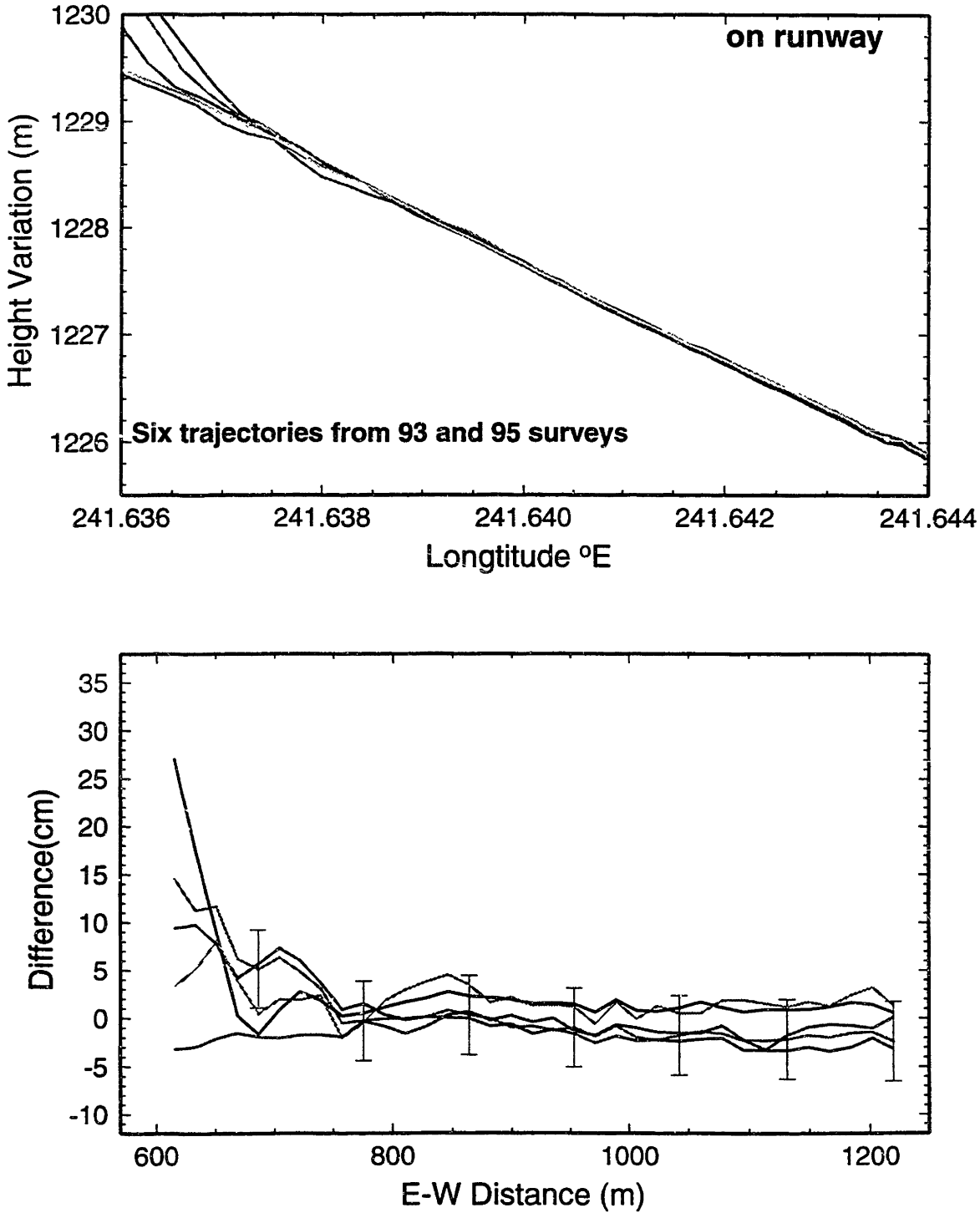
on runway
Six trajectories from 93 and 95 surveys
Height Variation (m)
1230
1229
1228
1227
1226
241.636
241.638
241.640
241.642
241.644
Longtitude °E
Difference(cm)
35
30
25
20
15
10
5
0
-5
-10
600
800
1000
1200
E-W Distance (m)

Figure 4.21

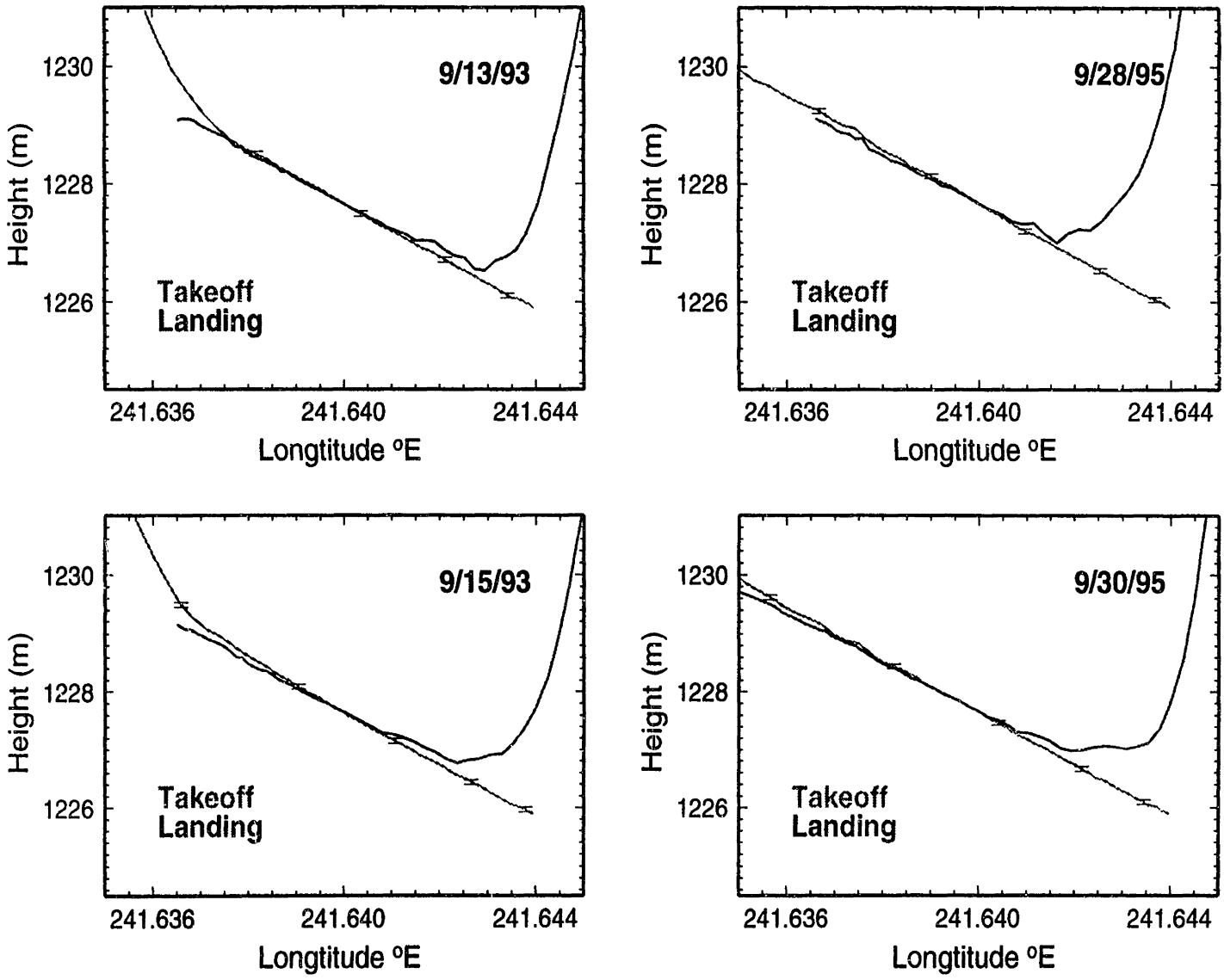
9/13/93
Takeoff
Landing
Height (m)
1230
1228
1226
241.636
241.640
241.644
Longtitude °E
9/28/95
Takeoff
Landing
Height (m)
1230
1228
1226
241.636
241.640
241.644
Longtitude °E
9/15/93
Takeoff
Landing
Height (m)
1230
1228
1226
241.636
241.640
241.644
Longtitude °E
9/30/95
Takeoff
Landing
Height (m)
1230
1228
1226
241.636
241.640
241.644
Longtitude °E

Figure 4.22

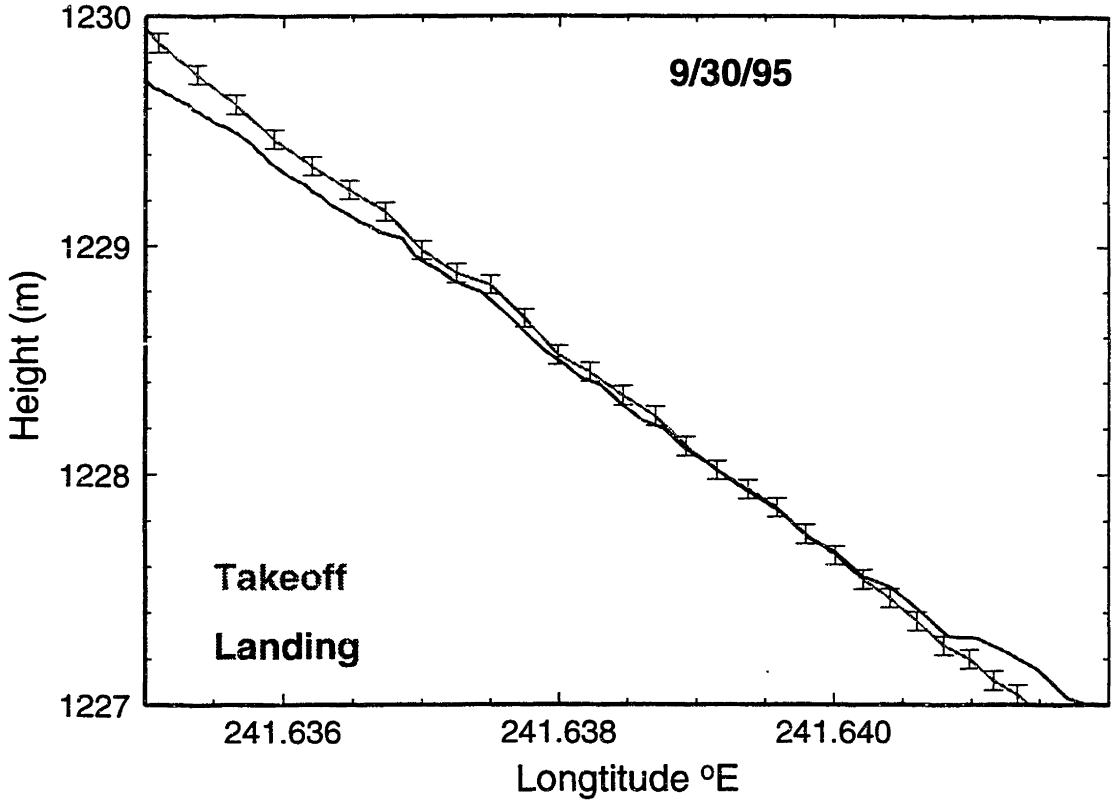
9/30/95
1230
1229
1228
1227
Height (m)
Takeoff
Landing
241.636
241.638
241.640
Longtitude °E

Figure 4.23

Chapter 5 Validation of GPS Trajectory from ATLAS Measurements

In this chapter, we address the quality of our trajectory by evaluating the GPS trajectories on the flights using the results obtained from the laser measurements over a flat surface, Lake Crowley. We use the laser altimetric results as an external data source to validate the trajectories because it is impossible to be done by GPS measurements themselves without the fixed marks for re-occupation. Another main goal of this chapter is to determine the improvement to the altimeter results through the use of our trajectory. The aircraft trajectory provided by GPS kinematic estimation is one integral part of entire airborne laser altimeter measurement system. and it is important to investigate the impact of GPS trajectory's accuracy to the precision of ground laser measurement of ATLAS system for calibration reasons.

5.1 ATLAS Data Analysis

The laser data used in this thesis were obtained by the NASA T39 jet aircraft during the 1993 surveys. T39 jet aircraft was equipped with the "Airborne Terrain Laser Topographic System" (ATLAS), two GPS receivers, a Litton LTN92 inertial navigation system (INS), and both video and still aerial cameras. The ATLAS was developed in the last decade by NASA for altimetric surveying. It is a low altitude (~ 500 meter) nadir-profiling altimetric laser system and yields a single surface footprint line with footprint radius of 0.85 meters on the ground in 1993 Long Valley survey. The sampling interval is set such that the footprints are approximately 2 meters apart. Because the laser port is fixed to the aircraft, its footprint on the ground will move off-nadir when the plane rolls or pitches. The INS is used to measure roll, pitch, and heading in order to locate the laser footprint in the post-flight processing. For more technical details of the ATLAS system are given by *Krabill et. al.*, [1995]; and *Ridgway et al.*, [1997]

We provided our new 1993 GPS trajectories to the SIO team who conducted the ATLAS data analysis in the same way as their previous data analysis [*Ridgway et al.*, 1997]. The surface height measurements of the laser footprints were returned to us for further analysis of aircraft's

trajectories. Our main purpose for this test was to validate the GPS trajectories, so we use only the laser height measurements over the flat surfaces such as Lake Crowley and the Benton Crossing.

5.2 Calibration over Lake Crowley

Lake Crowley is one of the four regular targets for the topographic calibration examination during the 1993 Long Valley surveys (Figure 5.1). The large flat surface of Lake Crowley is targeted for data calibrations in Long Valley surveys [*Ridgway et al.*, 1997]. Due to the periodic spilling of the water through the dam, the surface height may vary every day. However, changes in water level of the lake are available from the tide gauge measurements. For the 1993 surveys, we used the tide gauge measurements records from Ridgway's [1997] Figure 9 (1997) to adjust the lake surface heights. The lake surface height changes are -5.0 cm for the Sept. 14 flight and -8.5 cm for the Sept. 15 flights compared to the surface height recorded in the Sept. 13 flight. There are data available in two over-flights of Lake Crowley on Sept. 13 and 15, but only one flight on Sept. 14 due to the failure of GPS clock at the Bishop base station during the later flight section. All five elevation measurements over the Crowley Lake are shown in the Figures 5.2 - 5.4. In Figure 5.2, we show the results from the two flights on Sept. 13. For each track, we estimated a cubic polynomial line to fit the data. The cubic polynomials from both tracks have the same shapes and are offset by a consistent 0.8 cm over the 4 km plus track length. The difference is consistent with the increase of lake surface recorded from the tide gauge station during these time. We used a spline interpolation and 5-point moving average to smooth out the high frequency variations and show the results in the middle plot of the Figure 5.2. We plot the elevation height over the ellipsoid of aircraft over the Lake Crowley in the bottom plot of Figure 5.2. One flight is nearly flat while the other has 50 meter height variations. Although the trajectories of the two flights are not the same, the estimated topographic profiles of Lake Crowley are all close to each other everywhere. The RMS scatter of the profiles around the smoothed surface are 2.5 and 2.4 cm for the first and second tracks, respectively. The measured surface profiles have slopes of 3 cm/km which is a little less than the local geoid slope (4 cm/ km). However, the cubic like profile indicates that the strong wind on that day may have caused

the long wave variation and result in the water level deviating from an equipotential surface [*Minster*, 1998]. The steady wind pressure could cause several centimeter level change in long-wavelength in the water surface.

Figure 5.3 and Figure 5.4 show the other flights over the Lake Crowley on Sept. 14 and 15 surveys respectively. The measured surface profiles are very flat with a nearly constant slope rate around 4~5 cm/km which is close to the local geoid slope (4 cm/km). The mean difference of the Sept. 13's and Sept. 14's measured lake heights is 5.9 cm comparing to the 5 cm, the height variations obtained from the tide gauge observation. The mean difference of the Sept. 14's and Sept. 15's measured lake heights is 3.2 cm in a good agreement with the 3.5 cm, the tide gauge results. In *Ridgway*'s analysis of the 1993 ATLAS experiments, the second track of Sept. 15, 1993 (the fifth) has a 10 cm bias and the errors in the GPS trajectory were thought to be the cause. In our analysis, we have an approximately 4 cm variation in the middle section, but the second track agrees with the first track on the Sept. 15's in the beginning and end section (the middle plot of the Figure 5.4). We do not see a constant 10 cm bias in the fifth track. These new results indicate that part of errors in the former data analysis may be due to the failure of the old software to resolve correctly cycle slips and ambiguities during the flight.

We calculated the autocorrelation function of the differences between different tracks over Lake Crowley. The results are plotted in Figure 5.5 as a function of the distance along the lake in north-south direction. The autocorrelation length (1/e) is under 5 m. With an aircraft speed of ~80 m/s over lake, the time autocorrelation length (1/e) is under 0.1 second which is far smaller than that of GPS correlation time (70 seconds). The RMS scatter is also much larger than the GPS positioning RMS scatter (2.5 cm of ground track heights vs. less than 1 cm in GPS trajectory during less than 2 minutes). these results indicate that most of the errors of the laser measurements are at higher frequencies which may not be from the trajectory-related sources.

In order to investigate the effect of GPS trajectory on the topographic determination of the airborne laser altimeter, we plot the RMS scatter of the lake surface residuals in the five flight tracks over the Lake Crowley against the possible errors of the GPS trajectories in Figure 5.6. The RMS variations of the lake height from the laser measurements are computed by

subtracting their individual height estimates from their cubic-polynomial fitting lines. The errors of the GPS trajectory in Figure 5.6 are represented by the uncertainties in averaged single epoch which normally rely on the noise level of process noise and measurement noise as well as the satellite availability. The uncertainties can vary from 4 cm to 11 cm depending on the satellite constellation during the trajectory solution. A 5 cm noise level used for GPS system. However, the RMS variations of the lake surface heights are all around 2 cm to 2.5 cm for different flights with RMS from 2.3 to 2.4 cm (Figure 5.6). The second flight of the Sept. 15, 1993's survey has a slightly large scatter which may result from the unknown departure in the middle of the track (Figure 5.4). There is no obvious relationship between the precision of GPS trajectories and the laser height determination which implies that errors in the current GPS trajectories contribute a small amount to the high frequency errors in the height estimates. The results also suggest that a more realistic value for the scatter of surface heights is much less than the formal error of the trajectory when 5 cm phase noise is assumed.

5.3 Crossover Analysis

5.3.1 Lake Crowley

One important technique for assessing the errors in the altimeter data analysis is to compare the estimated heights at the same location from two flight tracks, a method called as the crossover analysis. Crossover analysis directly compares the laser footprint pairs for which centers are within a small search radius. If a search radius is small enough, the footprints should reveal the same (or close) elevation height. We use the crossover analysis software package developed by SIO to do the crossover analysis for the data collected in Lake Crowley and the Benson Crossing sections. The search radius in our analysis was set to the same radius used by *Ridgway et al.* [1997], 2 meter which yields a large set of points for the statistical test. Figure 5.7 shows the histogram of the cross analysis for Lake Crowley from first four track lines. The results of the fifth track are not used for the purpose of comparison to the Ridgway's results (which did not include this track). The tide gauge data are used to remove the time-varying lake

surface heights. The tide gauge station is near the dam, which is at the eastern side of lake, and the variations of the lake surface are under a few centimeter although the wind-driven seiches could cause some problems. The total number of crossover points obtained from the matching of the four lines is 276, which is larger than the 215 obtained by Ridgway et al. (1997). This may imply that our GPS trajectory determination is more stable. The mean elevation height difference of crossover points is 0.2 cm with a standard deviation of 4.5 cm. Almost 78% of crossover points are within 5 cm. This RMS scatter is close to the expected value of 3.5 cm based on the RMS scatter of the profile about the cubic fits. The additional scatter is probably due to the mean differences between the surface profiles.

5.3.2 Benton Crossing

Benton Crossing is at the edge of the Long Valley caldera but away from the resurgent dome (Figure 5.1). In this area the terrain is very flat with some low vegetation cover; the mean slope is approximately 1cm/m. Figure 5.8 shows the crossover statistical histogram for Benson Crossing with data from the tracks that cross that spot. When Compared to that of the flat lake surface, the crossover analysis for Benton Crossing shows longer tails. The outliers are caused by local rough ground topography. For example, two laser hits reflected from the opposite sides of the sharp stream bank edge in the terrain may generate a large range difference. The mean height difference of 218 point pairs is -2.1 cm with RMS of 21 cm. After deleting the outliers (difference larger than 0.4 m), the mean height difference of 202 point pairs is only -0.2 cm with RMS of 15 cm.

References

Hofton, M., J., Blair, B. Minster, J. Ridgway, D. Rabine, J. Bufton, and N. Williams, Using laser altimetry to detect topographic change at long Valley caldera, California, *Earth Surface Remote Sensing, SPIE 3222*, 295-306, 1997.

Krabill, W. B., Thomas, R. H., Martin, C. F., Swift R. N. and Frederick, E. B., Accuracy of airborne laser altimetry over the Greenland ice sheet, *Int. J. Remote Sensing, 16,* 1211-1222, 1995.

Minster, J. B., Private Communication and Discussion, 1998.

Ridgway, J. R., J.B. Minster, N. P. Williams, J. L. Bufton, and W. Krabill, Airborne laser altimetry survey of Long Valley, California, *Geophys. J. Int. 131,* 267-280, 1997.

Captions

Figure 5.1 Locations of the targeted area by repeat flights for the Long Valley mission (Benton Crossing, Antelope Springs and Lake Crowley) (from Hofton et al., 1997). Mono Lake is used for INS bias correction. The lines are the flights on the 3 days in 1993 mission.

Figure 5.2 The top plot shows the ground heights of laser footprints on the Lake Crowley surface on Sept. 13, 1993. The darker and lighter points are the first and second fly-over lines respectively, with the cubic fits to each fly-over shown with dark and light lines. Sampling rate is 50 Hz. The middle plot is the smoothed profiles of lake surface obtained by removing the variations with spatial scale <100 meters. The bottom plot shows the heights of the aircraft flight over Lake Crowley. The darker line are the first flight-over line and lighter line is the second in the same day. The sampling interval is 0.5 second (2Hz).

Figure 5.3 Similar plots as those in Figure 5.2 but for the flight on Sept. 14, 1993.

Figure 5.4 Similar plots as those in Figure 5.2 but for the flight on Sept. 15, 1993. The cubic fits are not performed due to the differences in the middle of lake which may result from the wind pressure or other forces.

Figure 5.5 The normalized autocorrelation functions of the measured surface height differences of Lake Crowley from four tracks. The solid line represents the lake surface height differences between the second and the first fly-over tracks on Sept. 13, 1993; the dash line represents the lake surface height differences between the only fly-over track on Sept. 14, 1993 and the second track on Sept. 13, 1993; and the dotted line represents lake surface height differences between the first fly-over track on the Sept. 15, 1993 and the first fly-over track over the lake on Sept. 14, 1993 The upper plot shows autocorrelation functions in full time while the lower plot shows the details in 0-50 m.

Figure 5.6 The RMS of altimeter determination of the Lake Crowley surface versus standard devi-

ations of the GPS trajectories. The uncertainties of surface of water level are calculated as the averaged departure values of the laser measurements from their cubic fits mainly due to the lake shapes and wind effects. The error bars represents the RMS scatter of the averaged departure values. The uncertainty of the GPS trajectory is the single point uncertainty of the GPS measurements. From left to right, there are results of the Sept. 15 first track, Sept. 13 first track, Sept. 14 track, Sept. 13 second track and the Sept. 15 second track respectively.

Figure 5.7 Histogram of repeat pass differences over Lake Crowley using ATLAS during the Sept., 1993 Long Valley mission. Search radius for crossover collocations is 2 meters. The height variation of daily lake surface is removed using the tide gauge observations. The number of cross-over points is 276 with the first 4 flight lines over the lake. The mean difference is 2 mm with standard deviation 4.4 cm.

Figure 5.8 Histogram of repeat pass differences over Benton Crossing using ATLAS during the Sept., 1993 Long Valley mission. The number of cross-over points obtained is 216. The mean difference is -2.1 cm with RMS 21.1 cm. After the outliers are removed (the darker bins), the mean difference is 0.2 cm with RMS 15 cm.

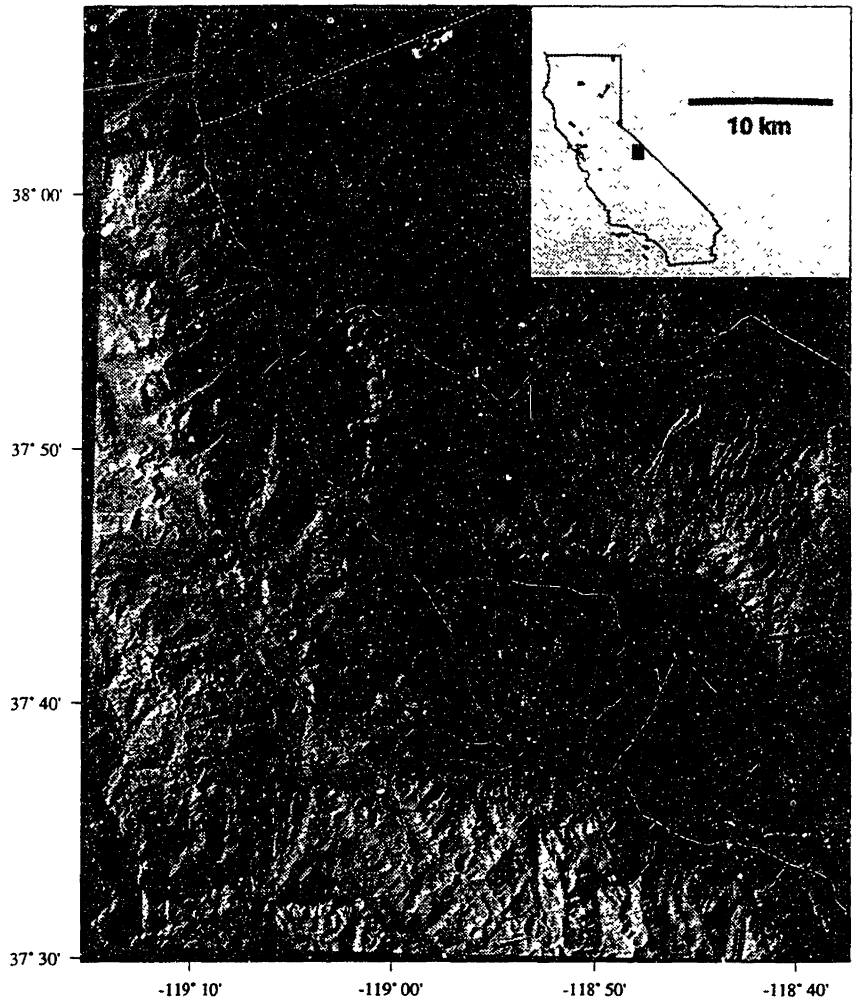

Figure 5.1

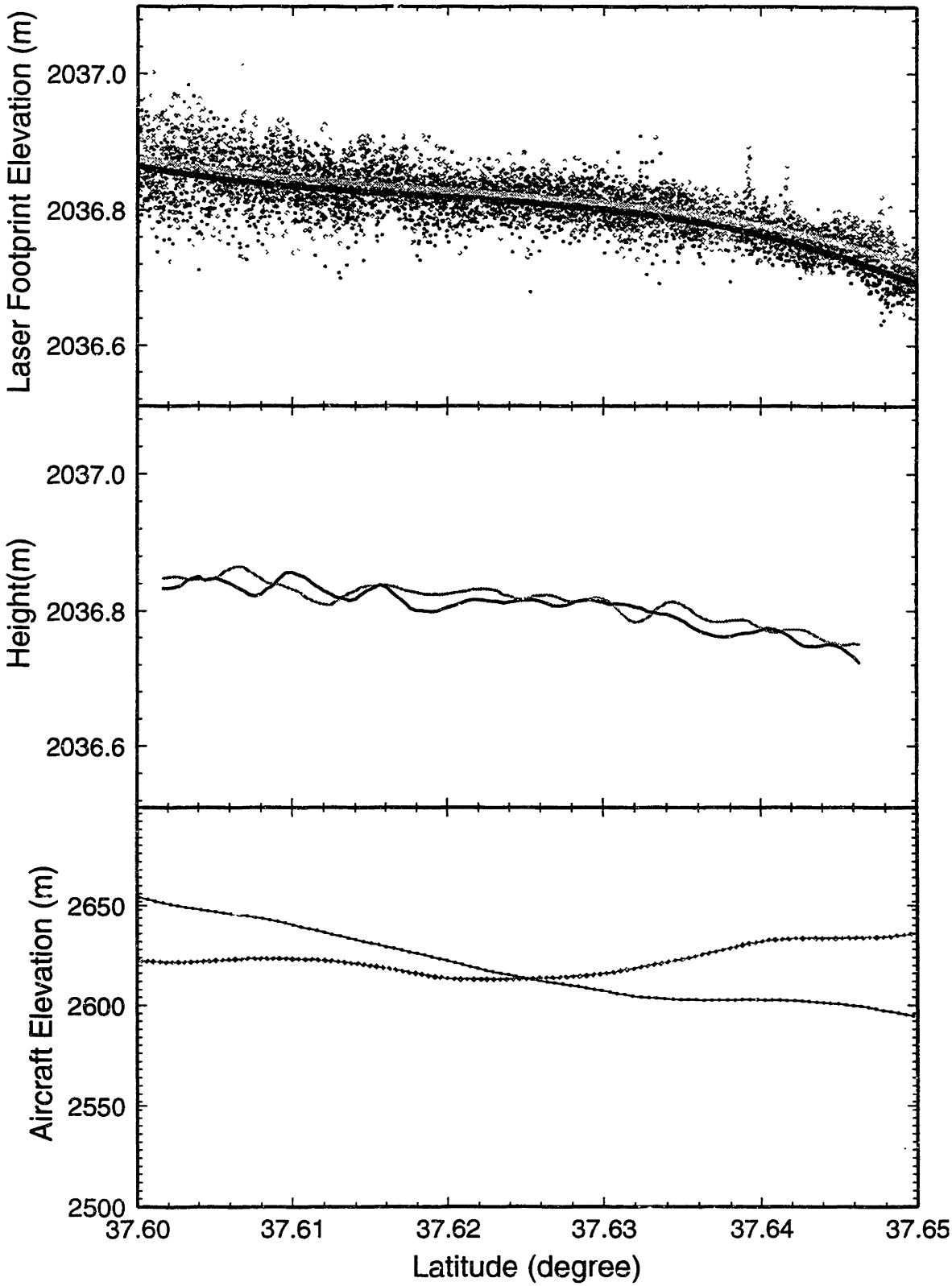
Laser Footprint Elevation (m)
2037.0
2036.8
2036.6
Height(m)
2037.0
2036.8
2036.6
Aircraft Elevation (m)
2650
2600
2550
2500
37.60
37.61
37.62
37.63
37.64
37.65
Latitude (degree)

Figure 5.2

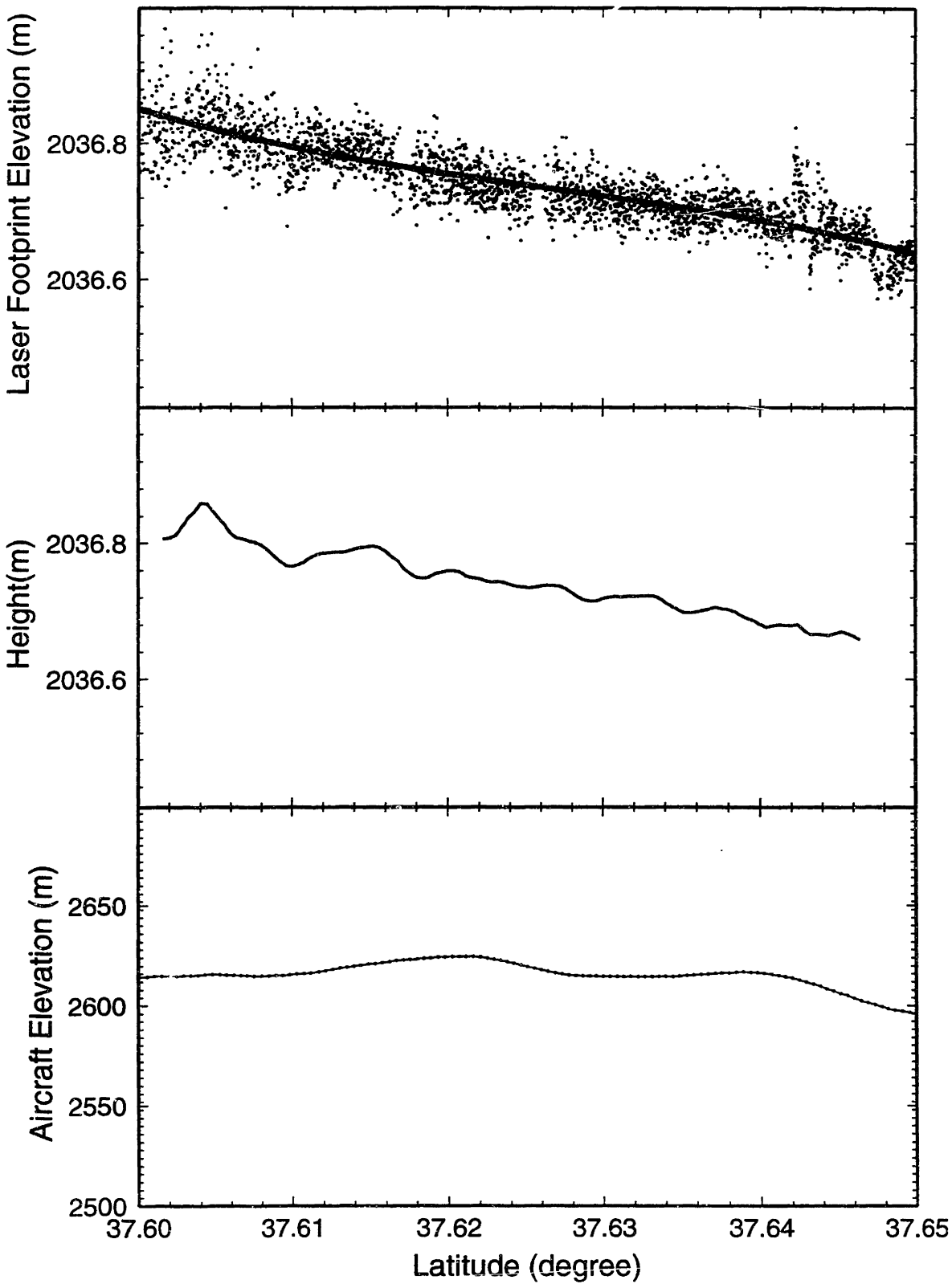
Laser Footprint Elevation (m)
2036.8
2036.6
Height(m)
2036.8
2036.6
Aircraft Elevation (m)
2650
2600
2550
2500
37.60
37.61
37.62
37.63
37.64
37.65
Latitude (degree)

Figure 5.3

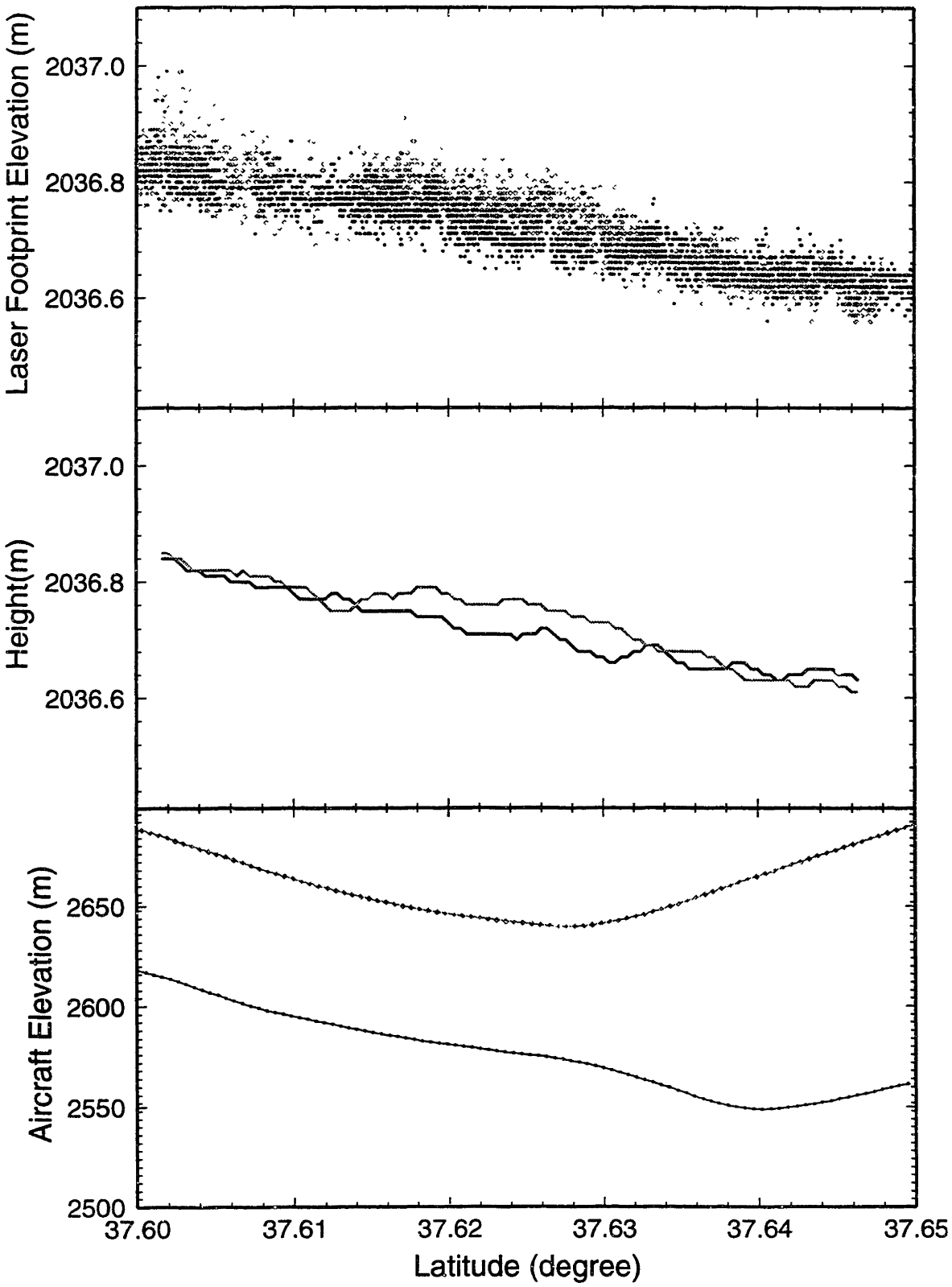
Laser Footprint Elevation (m)
2037.0
2036.8
2036.6
Height(m)
2037.0
2036.8
2036.6
Aircraft Elevation (m)
2650
2600
2550
2500
37.60
37.61
37.62
37.63
37.64
37.65
Latitude (degree)

Figure 5.4

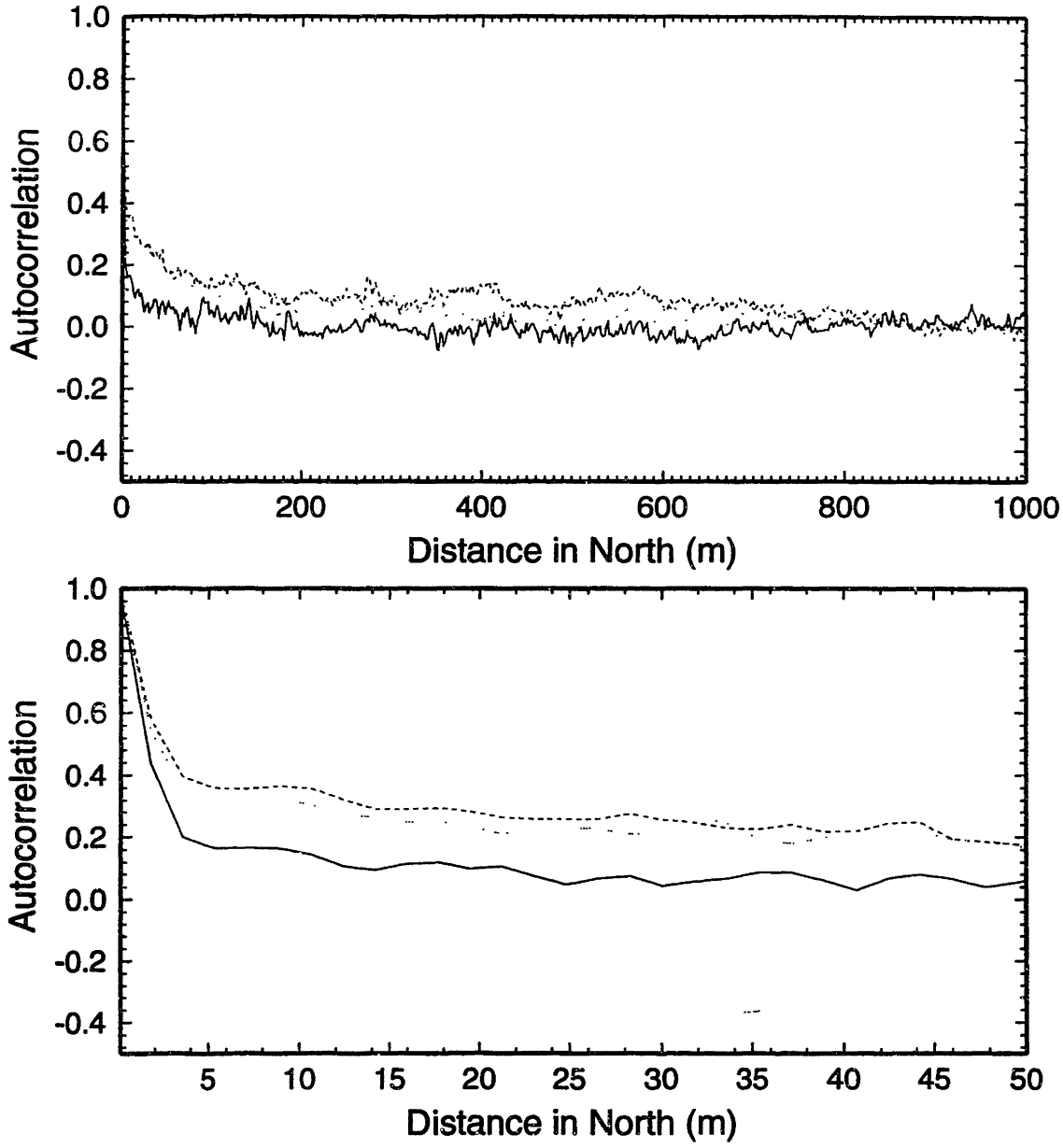
1.0
0.8
0.6
0.4
0.2
0.0
-0.2
-0.4
Autocorrelation
0
200
400
600
800
1000
Distance in North (m)
1.0
0.8
0.6
0.4
0.2
0.0
-0.2
-0.4
Autocorrelation
5
10
15
20
25
30
35
40
45
50
Distance in North (m)

Figure 5.5

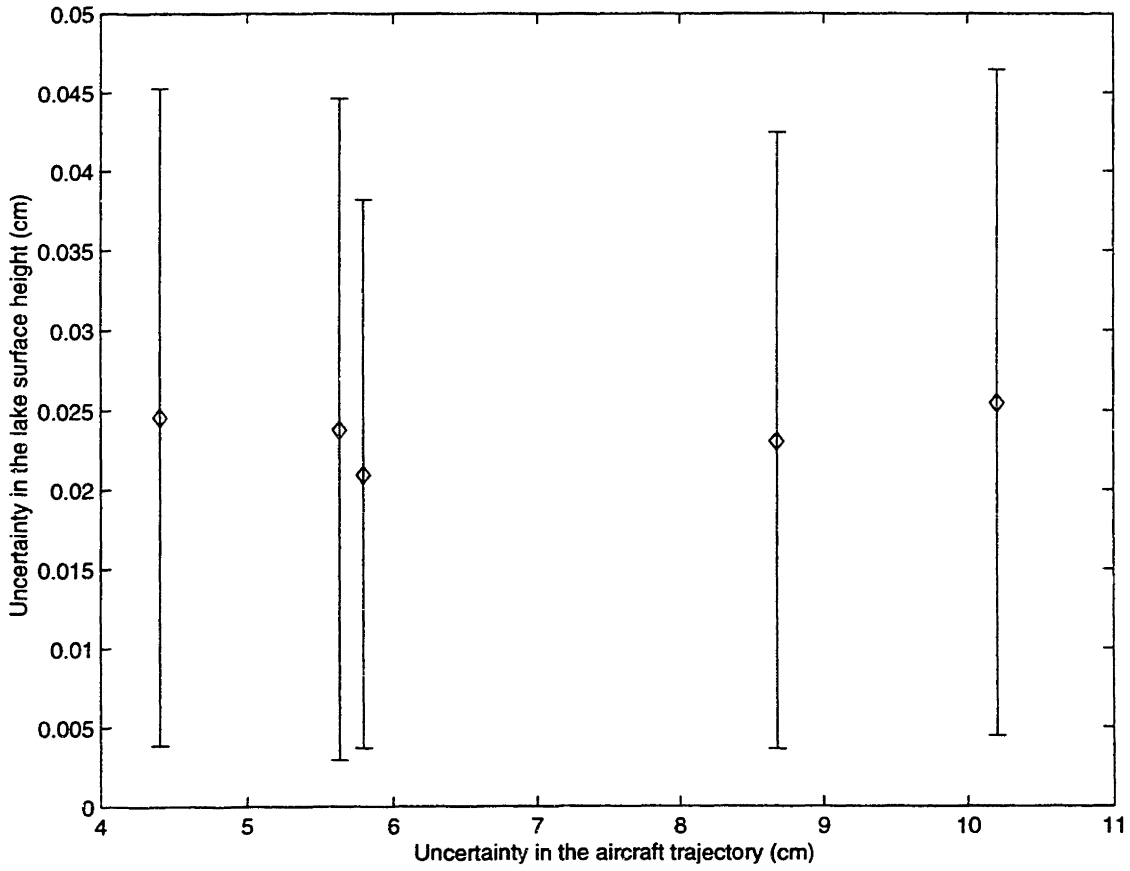
0.05
0.045
0.04
0.035
0.03
0.025
0.02
0.015
0.01
0.005
0
Uncertainty in the lake surface height (cm)
4
5
6
7
8
9
10
11
Uncertainty in the aircraft trajectory (cm)

Figure 5.6

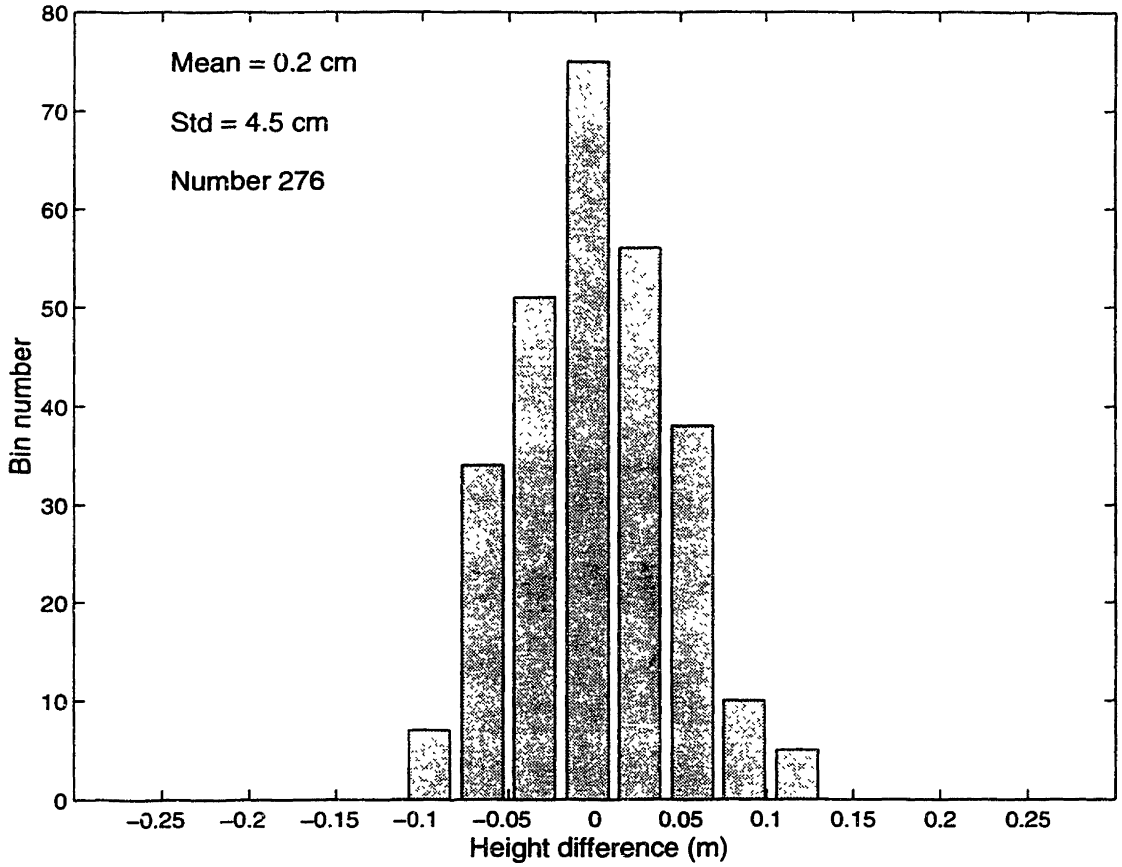
Mean = 0.2 cm
Std = 4.5 cm
Number 276
Bin number
Height difference (m)
80
70
60
50
40
30
20
10
0
−0.25
−0.2
−0.15
−0.1
−0.05
0
0.05
0.1
0.15
0.2
0.25

Figure 5.7

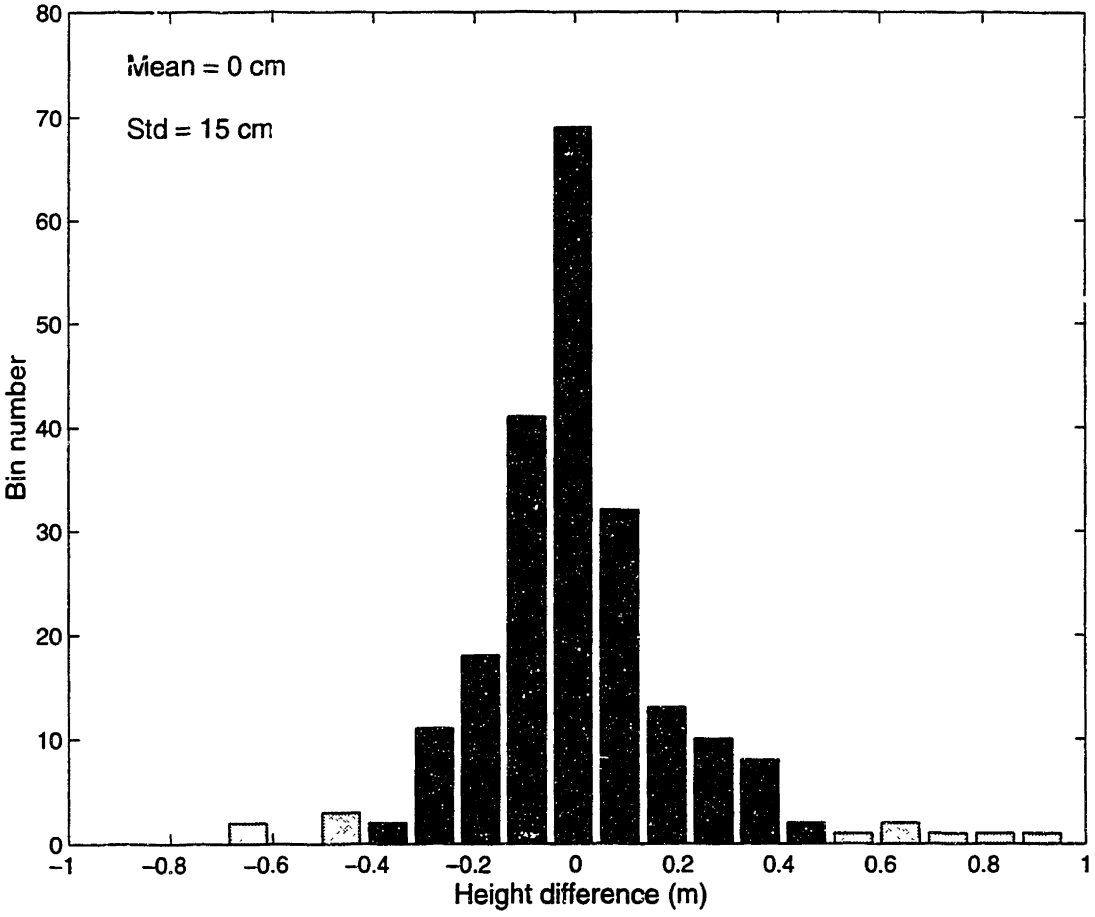
Mean = 0 cm
Std = 15 cm
Bin number
Height difference (m)
80
70
60
50
40
30
20
10
0
−1
−0.8
−0.6
−0.4
−0.2
0
0.2
0.4
0.6
0.8
1

Figure 5.8

Chapter 6. Discussion and Conclusion

In this thesis, we have developed an algorithm for kinematic GPS surveying in high speed vehicles, such as aircraft, based on Kalman filtering. Kalman filtering can use stochastic models to update the estimates of position and velocity without a clear knowledge of their physical models a feature for kinematic GPS surveying. In kinematic mode, the velocity model is not as well known as in the dynamic or quasi-dynamic mode, such as spacecraft positioning, whose processes are governed by clear physical laws. The aircraft accelerates and decelerates fairly arbitrarily and is hard to model dynamically even in a short time span. In this situation, the application of stochastic models such as random walks on velocities and positions of the aircraft can help us to utilize the information from past observations to estimate the current state in a simple and straightforward way. In our application, Kalman filter also shows its ability to include estimation of auxiliary different parameters, such as temporal variations of the clocks and atmospheric delays in GPS observations, together with the position changes of GPS receivers, all with appropriate stochastic models. The use of a Kalman filter helps the kinematic algorithm to utilize continuous temporal information of parameters in the data analysis.

Without accurate ambiguity estimates, the carrier phase observations can not achieve centimeter level accuracy. Developing an ambiguity resolution technique suitable for kinematic GPS measurements is the key point to use precise GPS carrier phase measurements at their full potential. The kinematic mode of aircraft GPS survey is more complicated and difficult than the static mode or the ground kinematic mode, in which a measured spot can be re-occupied. The static or repeated ground occupation of GPS receivers helps the determination of many model errors. The ionospheric delay, multipath and atmospheric delay can be averaged out by long time observations. In kinematic mode, these benefits disappear. It is difficult to separate model errors, such as uncorrected ambiguity bias from the motion of the GPS antenna. Thus we have to find a strategy to determine the ambiguity from observation data in a short time span and to utilize all available information to solve the problems

In this thesis, we developed methods for reliably determining integer L1 and L2 ambiguities using dual-frequency carrier phases. The approach is taken in two different ways regarding

of the ambiguity problems both in initialization and non-initialization conditions. For initial ambiguity search, we used the widelane and extrawidelane combinations to obtain the position-free initial guess for ambiguity sets. The lane constraints (integer relationship) between the L1/L2 dual frequency phase measurements are used for the reduction of the ambiguity search space. We also developed a new validation method which considers not only the RMS scatters of the phase residuals and the changes of this scatter, but also the balance between the use of low elevation observations to improve geometry and the errors that may be introduced because of propagation medium and multipath. For ambiguity changes during a flight, a method is developed to detect and fix the cycle slips and to resolve the ambiguity for new satellites much faster for the initial search. The method utilizes the available position information to reduce the effects of the position, ionospheric and other errors on the ambiguity estimation. Also a pre-filter examining of the widelane and extrawidelane can help us avoid the impact of ambiguity in the continuous estimation of position. The method we developed is flexible for different observation situation, and is capable of solving the ambiguity for a moving object in a short time of period. The goal of our ambiguity search method is not the reduction of computation time which most current methods on, but a flexible, quick (shorter time span) and unique resolution regardless of experimental conditions.

To process the GPS data sets involved in kinematic GPS measurements, we developed a robust software package to implement the algorithm based on the Kalman filtering and differential GPS technique. Our software takes the precise satellite orbit and clock information. By auto-examining of data and ambiguity, it makes it easier for users to process the kinematic GPS data. The use of this software is not limited to airborne laser altimetry but can also be used for many types of GPS kinematic surveying.

In the application of our software to the Long Valley mission, the repeatability of GPS kinematic surveys has shown to be under 3 cm by our runway tests and crossover analyses of the laser data. The software handles the GPS data well for an aircraft flying at altitudes in the range of 1 to 10 km. In the tests with 1993 and 1995 GPS data in Long Valley mission, our software obtained good trajectories in all cases except for the case when there are problems in the original data (such as the second trajectory part on Sept. 14, 1993). The five take-off and landing tracks of the aircraft trajectories matched within 3 cm with an average of 1.8 cm.

The application of GPS tracking into laser altimeter data analysis is also encouraging. The measurement of elevation height over Lake Crowley shows a centimeter-lever statistical accuracy in the repeat measurements. The profiles of the lake surface along the tracks are measured with RMS scatter between 2.0 to 2.5 cm. The differences of the profiles of the lake from different days also agree within 2 cm. Although the direct crossover analysis show a 4.5 cm point-to-point scatter, the near zero mean difference indicates such scatter can be smoothed out by repeat measurements. The crossover analysis for Benton Crossing also shows good terrain ground measurements with an average crossover residual under 1 cm for 216 points even though the scatter is larger (15 cm) due to rough local topography. The accuracy of the airborne laser altimetry can be assessed from the statistical analysis of data collected. A more stable and reliable GPS trajectory can provide more qualified interpolation points for the laser measurements and a better statistical resolution can be then deduced for ground profiling.

The noise analysis in the flights over Lake Crowley indicates most errors of the current altimetric data process are not directly related to those of GPS trajectories. Even when the formal errors of GPS trajectory change from 4 cm to 10 cm because of the decrease of the observable satellites, the mean RMS of the estimated lake surface does not change significantly. Also the variations of the differences between the tracks over Lake Crowley have much higher frequency noise than the static GPS. The autocorrelation length is 5 m (0.05 second under velocity of 100 m/s) for altimetric measurements comparing to 70 second for GPS measurements. Those facts imply that with a robust GPS algorithm, the errors of the estimated GPS trajectories are not the main sources for the airborne altimetry. The long autocorrelation length of GPS measurements indicates it is better to repeat the survey over the same area after a few minutes to smooth out the potential GPS bias for a track over a few kilometers such as that over Lake Crowley (5km). In most tests here, the estimated lake surface shape over the Lake Crowley shows that the differences between the repeat flights are less than 2 cm in most spots. It implies that the use of 5 cm for the phase noise is too large for the true behavior of GPS receiver. When a smaller noise level such as 0.5 cm is used, the single epoch uncertainties of the GPS trajectory will decease to 1 to 4 cm.

Although GPS trajectory determination has shown cm-level accuracy here, there is still

room for improvements for the future airborne surveys. The post-fit residuals are slightly larger in high altitude flights, especially for low elevation observations. For the flights at altitudes over 5 km, there are possible unmodeled errors arising from the atmospheric mapping function and ionospheric effects. With a thinner atmospheric path, the curvature of the ray is smaller than for a ray that reaches the ground. Although we have used several mapping functions that have the ability to model the height variation of the GPS receiver [*Davis et al.*, 990; *Herring*, 1992; *Neill* 1996], none of these models has been tested at 5 to 10 km ellipsoidal height. Also the effects of phase center rotation of GPS receiver at high speed is still unknown. *Ridgway et al.* [1997] conducted an antenna rotation test in the 1993 mission and found only 5 mm changes in the position. However, the rotation under high velocity may be different. The GPS antenna on the roof of the T39 aircraft is custom-designed and we do not have enough information for further antenna rotation test. Current calibration flight tests are performed on the nearly straight trajectory sections of flight; thus the effect of antenna phase may not been revealed in the repeat flights. Another concern related to the repeatability of the GPS measurements is the position accuracy of the GPS base station. In a 50-100 km baseline, the vertical variation of the base station position transfers almost exclusively into the measured heights of the aircraft trajectories (For a 20 cm change in the vertical position of the base station, the position of an aircraft 50 km away changed by 20 cm and 0.16 cm in vertical and horizontal directions, respectively.) The nearest permanent GPS station at Casa Diablo is not a good reference station for our reference station at Bishop because of the large and irregular geodetic displacements detected in Casa Diablo. So there is a need to measure the position of the Bishop base station related to several other global GPS stations in the future airborne laser measurements in Long Valley. By conducting long time static GPS measurements, we can also investigate the multipath and other location related errors around the base station.

Although there is no direct evidence that the changing satellite geometry increases the variations of trajectories in the Long Valley experiments, the formal error of the aircraft vertical position in a single epoch increase by a factor of two when the number of observable satellites decreases from six to 4. When the atmospheric zenith delay is estimated, the situation worsens (Figure 4.6). The atmospheric zenith correction affects the height determinations of the aircraft directly and may be needed when the atmosphere change is strong. Thus in the design of flight tracks, it is better to keep at least 5 satellites visible for the GPS measurements in the targeting

segment of the flights.

The airborne laser altimeter system is potentially capable of measuring changes of the vertical displacements of the topographic surface with centimeter accuracy. However, the precise airborne laser altimeter measurement is a complicated technique involving a laser altimeter, an inertial navigation system (INS), and GPS positioning for the aircraft. To achieve centimeter level positioning, the GPS trajectory determination of the airplane is a key element. With a fast resolution algorithm and a high quality centimeter-level GPS trajectory, it is possible that the airborne laser altimeter technique could facilitate rapid, direct and precise surface deformation monitoring in near real-time, which should benefit the study of many geodetic events such as volcanic eruptions. After several years of repeat flights, we expect the airborne laser system could reveal the vertical uplift in the top of resurgent dome near Long Valley caldera, which is expected to reach 4 cm/year. The GLAS launch is already planned for 2001. We hope the algorithm and software developed here could provide some useful experience for the future GPS tracking application in the centimeter space laser altimetry.

Appendix A: Atmospheric Delay Modeling

The atmospheric delay contribution to the delay of the GPS signal in given by

$$L_a = \int_{atm} n(s)ds - \int_{vac} ds \qquad \text{(A-1)}$$

where *n(s)* is the refractive index along the ray path. The first integral in (A-1) is along the real path in atmosphere and the second integral is along the vacuum path of the ray. Since the values of *n(s)* are not well-known, the equation (A-1) is approximated by the introduction of zenith delay, the atmospheric delay determined in the zenith direction, and a "mapping function" which is the ratio of L_a in any directions to the zenith delay. Azimuth asymmetric effects exist [*Chen and Herring*, 1997] but, to simplify the problem, most of atmospheric delay models still use a common symmetric assumption in the mapping functions. We re-write the atmospheric delay equation (A-1) as

$$L_{atm}(\varepsilon) = Z_d m_d(\varepsilon) + Z_w m_w(\varepsilon) \qquad \text{(A-2)}$$

where Z_d, Z_w are the hydrostatic (dry) and wet components in the zenith directions; $m_d(\varepsilon)$ and $m_w(\varepsilon)$ are the dry and wet mapping functions; ε is the elevation angle of the ray. Our kinematic GPS software has options to allow the user to choose several different atmospheric models. We discuss them in the following section.

Saastamoinen Zenith Delay

The most popular formula used for zenith delay is that developed by *Saastamoinen* [1972]. It relates the pressure, temperature, and humidity as well as the latitude and height of the site to the propagation delay in the zenith direction. The dry zenith delay Z_d is defined as:

$$Z_d = \frac{0.002277 P_0}{f(\varphi, H)} \qquad \text{(A-3)}$$

where P_0 is the total pressure in mbars of the point, $f(\phi, H)$ is a function which accounts for the variations of gravity with the latitude ϕ and altitude H (in km) of the point, and is given in [*Davis,*

1985]

$$f(\phi, H) = 1 - 0.0026(1 - 2\sin^2\phi) - 0.00031H \qquad \text{(A-4)}$$

The "wet" zenith delay Z_w is defined related to wet pressure e_0 (in mbars) as

$$Z_w = \frac{0.002277 e_0}{f(\varphi, H)}\left(\frac{1255}{T_0} + 0.05\right) \qquad \text{(A-5)}$$

where T_0 is the absolute temperature of point (in Kelvins).

The use of mapping function has several choices: Marini model, CfA-2.2 model, MTT model (both temperature and seasonal temperature), and the Niell's HMF model [1996].

Marini model

The Marini formula is written as [Marini, 1974]

$$m(\varepsilon) = \frac{1}{\sin\varepsilon + \dfrac{A/(A+B)}{\sin\varepsilon + 0.015}} \qquad \text{(A-6)}$$

where A is the Saastamoinen zenith delay given by sum of (A-3) and (A-5) and B is given by

$$B = \frac{2.644x10^{-3}}{f(\varphi, H)}\exp(-0.14372H) \qquad \text{(A-7)}$$

Equation (A-6) is used for both dry and wet mapping function.

CfA model

After it was found that Marini formula was inadequate for the lower elevation of observations especially those below 15o, *Davis* (1986) developed a model known as CfA-2.2:

$$m(\varepsilon) = \frac{1}{\sin\varepsilon + \dfrac{a}{\sin\varepsilon + \dfrac{b}{\sin\varepsilon - 0.009}}} \tag{A-8}$$

With

$$\begin{aligned} a &= 0.001185[1 + 0.6071x10^{-4}(P_0 - 1000)] \\ &\quad - 0.1471x10^{-3}e_0 + 0.3072x10^{-2}(T_0 - 20) \\ &\quad + 0.1965x10^{-1}(\beta + 6.5) \\ &\quad - 0.5645x10^{-2}\ (h_t - 11.231) \end{aligned}$$

$$\begin{aligned} b &= 0.001144[1 + 0.1164x10^{-4}(P_0 - 1000)] \\ &\quad + 0.2795x10^{-3}e_0 + 0.310910^{-2}(T_0 - 20) \\ &\quad + 0.3038x10^{-1}(\beta + 6.5) \\ &\quad - 0.1217x10^{-1}(h_t - 11.231) \end{aligned} \tag{A-9}$$

where P_0 is the total pressure (mbars), e_0 is the partial pressure of water vapor (wet) (mbars), T_0 is the temperature (in Celsius), β is the tropospheric temperature lapse rate (K km^{-1}) and h_t is the height of tropopause (in km).

MTT model

The CfA mapping function strictly requires the knowledge of the upper atmospheric conditions which are not available for most locations. *Herring* (1992) developed a mapping function that depends only on the surface temperature T_s, latitude φ and ellipsoid height of point H_s:

$$m(\varepsilon) = \frac{1 + a/(1 + b/(1 + c))}{\sin\varepsilon + \dfrac{a}{\sin\varepsilon + \dfrac{b}{\sin\varepsilon + c}}} \tag{A-10}$$

With coefficients *a, b, c* in dry mapping function as

$$a = [1.232 + 0.013\cos\varphi - 0.0209H_s + 0.00215(T_s - 10)]x10^{-3}$$

$$b = [3.1612 - 0.013\cos\varphi - 0.0331H_s + 0.00206(T_s - 10)]x10^{-3}$$

$$c = [71.244 - 4.293\cos\varphi - 0.149H_s - 0.0021(T_s - 10)]x10^{-3} \quad \text{(A-11)}$$

and coefficients a, b, c in wet mapping function as

$$a = 0.583 - 0.011\cos\varphi - 0.052H_s + 0.00215(T_s - 10)]x10^{-3}$$

$$b = [1.402 + 0.102\cos\varphi - 0.101H_s + 0.0020(T_s - 10)]x10^{-3}$$

$$c = [45.85 - 1.91\cos\varphi - 1.29H_s + 0.015(T_s - 10)]x10^{-3} \quad \text{(A-12)}$$

HMF model

Arthur *Niell* [1996] developed expressions for mapping function (NMF function). The formula of NMF mapping function is as same as that of MTT function except the coefficients. The coefficients of NMF mapping function depend on the latitude and height above the sea level of the observation point and the day of the year. For details of coefficient table of NMF, refer to *Niell* [1996].

Reference

Chen, G. and T. A. Herring, Effects of atmospheric azimuth asymmetry on the analysis of space geodetic data, *J. Geophys. Res.* **102**, 20,489-20,502, 1997

Davis, J,L., Atmospheric propagation effects on radio Interferometry, *Ph. D. Thesis, MIT, Cambridge, MA,* 1986

Marini, J. W. and Murray, C. W., Correction of laser range tracking data for atmospheric refraction at elevations above 10 degrees, *NASA report X-591-73-351, Goddard Space Flight Center,* 1973.

Herring, T. A., modeling atmospheric delays in the analysis of space geodetic data, in *Refraction of trans-atmospheric Signals in Geodesy, eds. J. C. Munck and T. A. Spoelstra, Netherlands Geodetic Commission Publications in Geodesy*, 36,157- 36,164, 1992.

Saastamoinen, Contribution to the theory of atmospheric refraction. *Bulletin Geodesique,* **107,** 13-34, 1972

Niell, A. E., Global mapping functions for the atmosphere delay at radio wavelengths, *J. Geophys. Res.*, **101, B2**, 3227-3246, 1996.